J. Fluid Mech. (1991), *vol.* 230, *pp.* 583–646
Printed in Great Britain

Collision of two vortex rings

By S. KIDA[1]†, M. TAKAOKA[2]‡ AND F. HUSSAIN[3]

[1] Applied and Computational Mathematics, Princeton University, Princeton, NJ 08544, USA

[2] Department of Physics, Faculty of Science, Kyoto University, Kyoto 606, Japan

[3] Department of Mechanical Engineering, University of Houston, Houston, TX 77004, USA

(Received 23 February 1990)

The interaction of two identical circular viscous vortex rings starting in a side-by-side configuration is investigated by solving the Navier–Stokes equation using a spectral method with 64^3 grid points. This study covers initial Reynolds numbers (ratio of circulation to viscosity) up to 1153. The vortices undergo two successive reconnections, *fusion* and *fission*, as has been visualized experimentally, but the simulation shows topological details not observed in experiments. The shapes of the evolving vortex rings are different for different initial conditions, but the mechanism of the reconnection is explained by *bridging* (Melander & Hussain 1988) except that the bridges are created on the front of the dipole close to the position of the maximum strain rate. Spatial structures of various field quantities are compared. It is found that domains of high energy dissipation and high enstrophy production overlap, and that they are highly localized in space compared with the regions of concentrated vorticity. The kinetic energy decays according to the same power laws as found in fully developed turbulence, consistent with concentrated regions of energy dissipation. The main vortex cores survive for a relatively long time. On the other hand, the helicity density which is higher in roots of bridges and threads (or legs) changes rapidly in time. The high-helicity-density and high-energy-dissipation regions overlap significantly although their peaks do not always do so. Thus a long-lived structure may carry high-vorticity rather than necessarily high-helicity density. It is shown that the time evolution of concentration of a passive scalar is quite different from that of the vorticity field, confirming our longstanding warning against relying too heavily on flow visualization in laboratory experiments for studying vortex dynamics and coherent structures.

1. Introduction

Vorticity dynamics is one of the most fundamental means of understanding fluid motion, especially at high Reynolds number and in turbulent flows. For an incompressible flow, the velocity and vorticity fields contain almost equivalent information. Although vorticity is more difficult to measure in experiments, particularly in three-dimensional turbulent flows, there are several reasons why the vorticity field is a more fundamental quantity.

First, in high-Reynolds-number flows, high-vorticity regions are more localized in space than velocity. Vorticity, unlike velocity, is Galilean invariant. A velocity field

† On leave from Research Institute for Mathematical Sciences, Kyoto University, Kyoto 606, Japan

‡ Present address: Department of Mechanical Engineering, Faculty of Engineering Science, Osaka University, Toyonaka, Osaka 560, Japan.

induced by vorticity in an incompressible flow is obtainable from the Biot–Savart induction equation. Thus it is easier to understand fluid phenomena and to build a model for them, if necessary, in terms of vorticity than velocity. The vortex method, which is one of the most powerful numerical schemes to solve high-Reynolds-number flows, is based upon an idealization of concentrated vorticity regions (Leonard 1980; Chorin 1982; Shirayama & Kuwahara 1984).

Second, turbulent motion is more clearly evident in the vorticity field than in the velocity field. The large-scale organized structures, the so-called *coherent structures*, which persist for relatively long times in turbulent flows, are characterized by domains of coherent vorticity and their interactions and evolution can be explained in terms of vortex dynamics (Hussain 1983).

Third, in comparison with the large-scale organized structures, splintered regions of high vorticity, which mostly form bundles, are the source of intermittency in turbulence. The probability distributions of velocity derivatives and vorticity have exponential tails which decay much slower than the Gaussian distribution – a characteristics of the intermittency of turbulence (Kida & Murakami 1989).

Fourth, the topological structure of vortex lines is closely related to helicity (the spatial integral of the inner product of velocity and vorticity $\boldsymbol{u}\cdot\boldsymbol{\omega}$) and super-helicity density $\boldsymbol{\omega}\cdot\boldsymbol{\chi}$, where $\boldsymbol{\chi} = \nabla\times\boldsymbol{\omega}$ is the di-vorticity (Kida 1985). In an inviscid flow which is composed of closed vortex lines, the total amount of knottedness or entanglement and circulation of vortex lines determine the helicity, which is one of constants of motion for inviscid flows (Moffatt 1969). The Kelvin–Helmholtz theorem states that vortex reconnection is inhibited in the inviscid case. Both topology and circulation of vortex lines do not change in time, and so is the case with helicity. In a viscous fluid, on the other hand, helicity may increase or decrease depending on the structure of the flow field or, more precisely, in proportion to viscosity and the negative of super-helicity (see (7.5)). The existence of viscosity is a necessary condition for vortex reconnection (see Kida & Takaoka 1991). It should be mentioned here that vortex reconnection does not always cause helicity to change. For example, in a collision of two vortex rings, which will be considered in this paper, helicity is zero at all times and reconnection is not accompanied with helicity change. A reconnection in a trefoiled vortex (Kida & Takaoka 1987, 1988), on the other hand, results in a helicity change. The invariance of helicity in the inviscid limit is not obvious since the super-helicity may blow up in this limit. A similar problem remains unsolved for the energy dissipation in the inviscid limit (e.g. Kida 1983). There is a numerical suggestion that the helicity may be invariant in the inviscid limit (Kida & Takaoka 1988), but more extensive simulations and analyses are necessary to solve this subtle problem. This limiting property of the change in time of helicity has some relevance to the theory of turbulence. The so-called helicity-cascade theory is based upon the existence of finite helicity transfer to the small-scale motions in the inviscid limit (Brissaud *et al.* 1973).

Fifth, the singularity of the solution of the Navier–Stokes equation or Euler equation is directly related to the vorticity field. The formation of a singularity must be accompanied by a blow-up of the vorticity field (Beale, Kato & Majda 1984). The verification of a finite time singularity has been tried extensively by the direct numerical simulation of the Navier–Stokes and Euler equations (Siggia & Pumir 1985; Kerr & Hussain 1989), but it is still hard to obtain a conclusive result for the existence of a singularity by numerical simulation because it requires very high resolution and very long time integration.

The interaction between vortex tubes which are moving in an irrotational

surrounding flow has been studied extensively by many researchers both experimentally and numerically. Among other configurations the motion and the interaction of two circular vortex rings are expected to exhibit the mechanism of the vortex reconnection processes in the simplest way. In fact, visualizations by dye and smoke as well as measurement of vorticity have revealed the nature of vortex interactions (Fohl & Turner 1975; Oshima & Asaka 1977; Schatzle 1987; Oshima & Izutsu 1988). In the experiments, two circular vortex rings which are ejected side by side from nozzles undergo two successive reconnections. (Note, however, that what is observed in the experiments is not vorticity but a passive scalar (see §6).) The two rings merge into a single distorted ring in the first reconnection. This ring then splits in the second reconnection into two rings in a direction perpendicular to the initial rings. In Schatzle's experiments, an averaged vorticity field was obtained by taking an ensemble average over many realizations. Since successive realizations do not necessarily exactly repeat, the inherent jitter is bound to introduce substantial smoothing of the averaged vorticity field. Owing to technical limitations it is hard to measure vorticity with high accuracy. Moreover, the data analysis is limited only to several planes while three-dimensional data on the flow field are necessary to understand the mechanism of vortex reconnection. A drastic improvement of the measuring technique is highly desirable.

Numerically, a number of studies of the vortex reconnection problem have been attempted for various configurations of vortex tubes: for example, the vortex stick method (Leonard 1974; Anderson & Greengard 1988), the vortex filament method (Siggia 1985; Schwarz 1985; Siggia & Pumir 1985), contour dynamics (Shariff *et al.* 1988), the spectral method (Kida & Takaoka 1987, 1988; Melander & Zabusky 1988; Melander & Hussain 1988; Kida, Takaoka & Hussain 1989; Kerr & Hussain 1989) and the finite-difference scheme (Chamberlain & Liu 1985). The occurrence of vortex reconnection is obvious in these simulations, but the detailed mechanism of the reconnection processes has not been fully understood and varies considerably among these studies.

A simple and naive explanation of the mechanism of the reconnection process of a pair of nearly anti-parallel vortex tubes may be a simple *cancellation* of vorticity of opposite sign (figure 1). A continuous squashing of a vortex pair by a converging flow induced by either the rest of the vortex tubes or an external flow is a necessary condition for the cancellation to be completed. The interacting pair itself does not induce a strong enough colliding velocity for completion of the cancellation because it is weakened during the reconnection process (§3.3). As will be shown later, the configuration in the reconnection process would not remain two-dimensional, but the curved vortex tubes inevitably induce motion in the third direction, which makes the phenomenon complicated. It is expected, however, that at the beginning of the reconnection, vortex lines have an X-structure such as illustrated in figure 1.

Another mechanism which was observed by a numerical simulation is the '*bridging*' studied by Kida & Takaoka (1987, 1988), in which a strong-vorticity blob bursts out of other than the closest point of interacting parts of a trefoiled vortex ring. The mechanism of this bursting, however, has not been fully understood yet. Another phenomenon, called *fingering*, was observed in a simulation of two orthogonal straight vortex tubes (Melander & Zabusky 1988). More recently, Melander & Hussain (1988, this paper will be cited as MH in the following) made a numerical simulation of a pair of anti-parallel sinusoidally perturbed vortex tubes and discovered a new mechanism of vortex reconnection, also called 'bridging' by

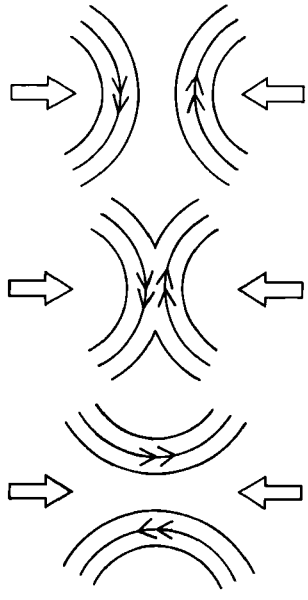

FIGURE 1. Cartoon of vortex reconnection by a simple cancellation of opposite-signed vortex lines. Double arrows indicate directions of vorticity and big arrows a converging flow around the interaction zone.

them, which was proposed as a different mechanism from that noted by Kida & Takaoka.

As stated before, the study of two vortex rings was initiated by laboratory experiments using dye or smoke as tracers. Observations of many interesting phenomena such as the cross-linking of vortex tubes, the wave formation on a vortex ring and the repetition of overtaking of two vortex rings stimulated subsequent analytical and numerical studies of the motion of vortex tubes of various shapes. It should be noted, however, that the spatial pattern of concentration of passive scalars such as dye and smoke does not represent faithfully the motion of vorticity magnitude (Hussain 1983). This claim stems from the completely opposite effects of stretching of fluid elements on the intensity of vorticity and on the concentration of a scalar quantity; i.e. a stretching intensifies the strength of vorticity but diminishes the concentration of a passive scalar.

In this paper we deal with the interaction of two circular vortex rings which start with a side-by-side configuration, as in the experiments cited above. The motion of the vortex rings is followed by solving the Navier–Stokes equation numerically. The periodic boundary condition is imposed. The calculation employs a spectral method with 64^3 collocation points. The primary goals of this study are to (i) simulate numerically two successive vortex reconnections which were visualized in laboratory experiments, but have not yet been realized in a numerical simulation, (ii) reveal the detailed mechanism of the vortex reconnection process by analysing three-dimensional fields of various properties, (iii) examine the dependence of the reconnection process on the initial condition (inclination angle) as well as on viscosity, (iv) compare the spatial structure of enstrophy, energy-dissipation, enstrophy production and helicity densities, in order to establish a possible relation of coherent structures with these quantities, and (v) discuss the similarity and differences in the evolutions of vorticity and passive scalar fields. A preliminary part

of the present study has been already reported (Kida *et al.* 1989), in which we showed qualitative aspects of the vortex interaction.

This paper is organized as follows. The numerical scheme and the initial set-up of the vortex tubes are explained in §2. We made several runs with different initial inclination angles and different viscosities. We take a single run in §3 to describe various phases of the interaction as well as the formation of a head–tail structure followed by the first and second reconnections. The mechanism of bridging is explained in some detail. In §4, we compare several runs with different initial conditions. The decay laws of energy and enstrophy are examined in §5, and are found to obey the same power laws as observed in turbulent flows. The transport property of a passive scalar advected by the vortex motion is examined in §6. The limitations of a passive scalar in marking high-vorticity regions is discussed. The relation between helicities and skewed structures of the flow field is studied in §7. Finally, §8 is devoted to our concluding remarks.

2. Numerical scheme and initial condition

We trace the motion of two vortex rings by solving the Navier–Stokes equation

$$\frac{\partial \boldsymbol{u}}{\partial t}+\boldsymbol{\omega}\times\boldsymbol{u}=-\boldsymbol{\nabla}\left(\frac{p}{\rho}+\frac{|\boldsymbol{u}|^2}{2}\right)+\nu\nabla^2\boldsymbol{u}, \tag{2.1}$$

or the vorticity equation

$$\frac{\partial \boldsymbol{\omega}}{\partial t}+(\boldsymbol{u}\cdot\boldsymbol{\nabla})\,\boldsymbol{\omega}=(\boldsymbol{\omega}\cdot\boldsymbol{\nabla})\,\boldsymbol{u}+\nu\nabla^2\boldsymbol{\omega}, \tag{2.2}$$

together with the continuity equation

$$\boldsymbol{\nabla}\cdot\boldsymbol{u}=0, \tag{2.3}$$

where

$$\boldsymbol{\omega}=\boldsymbol{\nabla}\times\boldsymbol{u} \tag{2.4}$$

is the vorticity and ν is the kinematic viscosity.

The velocity field is assumed to be periodic with a period 2π in all the three orthogonal directions. We consider the motion of vortex rings in a cyclic cube of side 2π. For convenience of description, we define the Cartesian coordinate system (x_1, x_2, x_3) as shown in figure 2. The origin is located at the centre of the box, and the x_1- and the x_2-axes are on diagonal planes. That is, (x_2, x_3) and (x_3, x_1) are diagonal planes, while (x_1, x_2) is a mid-plane parallel to opposite faces of the cube.

Initially, two identical circular vortex rings are set up as shown in figure 3. The centres of the vortex rings are on the x_1-axis. The distance between the centres of the two rings is D. The radius of the circular vortex rings is R and the core radius is a. The vortex rings are inclined by an angle θ towards the x_3-axis. Thus, the velocity field is symmetric with respect to the (x_2, x_3)- and the (x_3, x_1)-planes. These symmetries are preserved during the entire period in the simulation though we do not impose them in our numerical code. We start with two vortex rings along a diagonal of the computational box in order to maximize resolution. We use a Gaussian vorticity distribution in the core:

$$\omega(r)=\omega_0\exp\left[-\left(\frac{r}{a}\right)^2\right]. \tag{2.5}$$

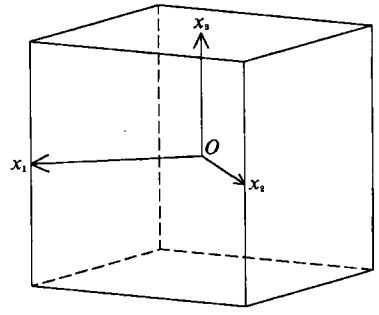

FIGURE 2. A periodic box and the Cartesian coordinate system.

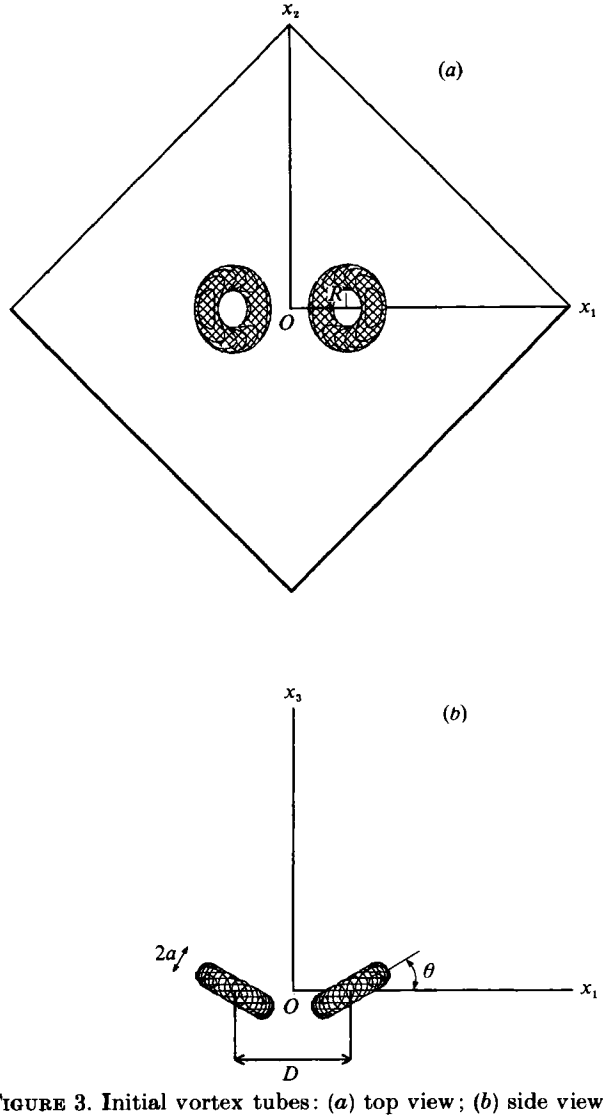

FIGURE 3. Initial vortex tubes: (a) top view; (b) side view.

Case	R	a	ω_0	θ (deg.)	D	$\mathscr{E}(0)$	$\mathscr{Q}(0)$	ν	Γ	Γ/ν	Δt	t_t
I	0.982	0.393	23.8	0	3.65	0.500	3.42	0.01	11.53	1153	0.02*	13
II	0.491	0.196	23.8	0	1.83	0.0168	0.428	0.005	2.88	577	0.05	30
III	0.491	0.196	23.8	15	1.83	0.0168	0.428	0.005	2.88	577	0.05†	45
IV	0.491	0.196	23.8	30	1.83	0.0168	0.428	0.005	2.88	577	0.05‡	60
V	0.491	0.196	23.8	45	1.83	0.0168	0.428	0.005	2.88	577	0.05†	45

TABLE 1. Parameters used in different runs (* 0.025 for $5 \leqslant t \leqslant 13$, † 0.1 for $15 \leqslant t \leqslant 45$, ‡ 0.2 for $30 \leqslant t \leqslant 60$)

Here r is the distance from the core centreline, ω_0 is the maximum vorticity at the core centre and a is the e^{-1}-fold radius of the core. The circulation of the vortex ring

$$\Gamma = 2\pi \int_0^\infty r\omega(r)\,\mathrm{d}r \tag{2.6}$$

is $\pi\omega_0 a^2$. The turnover time during which a fluid particle at a distance a from the centre of the ring goes around the centre once is about $6.3\pi/\omega_0$, which is 0.83 for $\omega_0 = 23.8$ (see table 1). The tail of the core of the vortex rings is terminated at $0.01\omega_0$ (which is at $2.14a$ from the centreline). This ensures that the vorticity of the two vortex rings does not overlap at the initial instant. The vorticity field is then adjusted to be exactly divergence-free by orthogonalizing the Fourier components of the vorticity field with wavenumber. Of course, by symmetry, the computation domain is circulation-free and remains so for the entire computation time.

Several runs of different orientations of vortex rings and different values of viscosity have been made. The relevant parameters, listed in table 1, include the kinetic energy (in a frame moving with the mean velocity $\boldsymbol{u}_0$ which is averaged over periodic cube and is constant in time),

$$\mathscr{E}(t) = \frac{1}{2}\int\int\int_0^{2\pi} \rho|\boldsymbol{u}(\boldsymbol{x},t)-\boldsymbol{u}_0|^2\,\mathrm{d}\boldsymbol{x} \quad (\rho \equiv 1), \tag{2.7}$$

and the enstrophy,

$$\mathscr{Q}(t) = \frac{1}{2}\int\int\int_0^{2\pi} |\boldsymbol{\omega}(\boldsymbol{x},t)|^2\,\mathrm{d}\boldsymbol{x}. \tag{2.8}$$

The initial vortex rings for Cases I and II have the same shape and orientation but the size of the two rings and the distance between them are different by a factor of 2. If we neglect the effects from other periodic boxes, we can scale the initial vortex rings for Case I by a change of variables,

$$l \to 2^{-1}l, \quad \boldsymbol{u} \to 2^{-1}\boldsymbol{u}, \quad \boldsymbol{\omega} \to \boldsymbol{\omega}, \quad t \to t, \quad \nu \to 2^{-4}\nu, \tag{2.9}$$

l being the lengthscale, so that it may coincide with Case II. Thus, Case I may be compared with Case II by reducing the viscosity to 0.0025. By transformation of variables (2.9), the energy and enstrophy are converted as

$$\mathscr{E} \sim l^3u^2 \to 2^{-5}l^3u^2 \sim 2^{-5}\mathscr{E}, \quad \mathscr{Q} \sim l^3\omega^2 \to 2^{-3}l^3\omega^2 \sim 2^{-3}\mathscr{Q}. \tag{2.10}$$

As seen in table 1, these correspondences are satisfied very well for the enstrophy but not well for the energy. This is because the energy is not as localized as the enstrophy, and the effects from the adjacent boxes cannot be neglected for the energy. Cases

II–V are simulations of the same initial vortex rings with the same distance between the centres and the same viscosity but with different inclined angles, $\theta = 0°$, 15°, 30° and 45°. We examine the initial-condition dependence by comparing these four runs. The radii 0.982, 0.491, 0.393 and 0.196 cover 10, 5, 4 and 2 mesh points, respectively. The final time of the calculation t_f is shown in the last column of table 1.

The parameters listed in table 1 were chosen carefully after an extensive check of numerical accuracy by comparing various runs with different resolutions and viscosities. We made a larger (128^3) simulation with exactly the same initial condition as Case I and found no visible difference from the vortex contours shown in figure 5 below from the present 64^3 run.

We solved the vorticity equation (2.2) by a spectral method on N^3 ($= 64^3$) grid points. The aliasing interactions are eliminated by a shifted Fourier transformation and the truncation of the Fourier components outside an octadecahedron in the wavenumber space, which is defined by $|k_j \pm k_k| = \frac{2}{3}N, j, k = 1, 2, 3, j \neq k$, and $|k_j| = \frac{1}{2}N, j = 1, 2, 3$ (Orszag 1971). In this method the Fourier components of wavenumber magnitude at least $\sqrt{2}/3N$ are retained in all directions in the wavenumber space. Time marching is done by the Runge–Kutta–Gill scheme with the time increment Δt shown in table 1.

3. Interaction of vortex tubes

3.1. *Overview*

The evolution of the two vortex rings is conveniently represented by iso-surfaces of vorticity norm $|\omega|$. They are plotted in figures 4(*a*)–4(*d*) at several representative stages of evolution for Case I, seen from the (2, 1, 5)-, (0, 0, 1)-, (1, 0, 0)- and (0, −1, 0)-directions, respectively. The levels of the iso-surfaces are 25 % of the instantaneous maximum of the vorticity norm $|\omega|_{\max}$ (see figure 18*a* below). Remember that these surfaces are not vorticity surfaces. Where vorticity is higher, the iso-surface of the vorticity norm produces a larger object than that of the vorticity surface. Vorticity lines may cross the iso-surfaces of the vorticity norm.

Self-induction causes the two vortex rings to travel in the x_3-direction and mutual induction causes them to turn toward the (x_2, x_3)-plane. These together make them approach each other and they collide on the (x_2, x_3)-plane at around $t = 3$ (figure 4*a–d*(ii)). The vortices are anti-parallel at the contact point and vortex lines of opposite directions are cancelled by viscous cross-diffusion, and at the same time vortex lines in the main tubes are connected to create a single big distorted ring. (A detailed explanation of the reconnection mechanism will be given in the following subsections.) This cancellation cannot be completed and the uncancelled part, which is called the *thread* (MH), is left on the front of the vortex tube (figure 4*a–d*(v)). Meanwhile the curvature-induced motion distorts the ring. Thereafter, these threads swirl around the main tubes because of the velocity induced by the latter, while being diffused by viscosity (figure 4*a–d*(vi, vii)). The decay process is not straightforward because the threads, being anti-parallel to and much weaker than the main vortex tube, undergo cancellation with the main vortex tube by viscous cross-diffusion. Thus virtually a single ring (figure 4*b*(vii)) emerges out of the initial two.

The main distorted ring moves further along the x_3-direction. The velocity induced by its own vorticity distribution causes a stretching of the tube in the x_2-direction and a shrinking in the x_1-direction (figure 4*b*(v–vii)). It takes a gourd-shaped form around $t = 7$ (figure 4*a*(vii)). The curvature at the two round ends of the tube

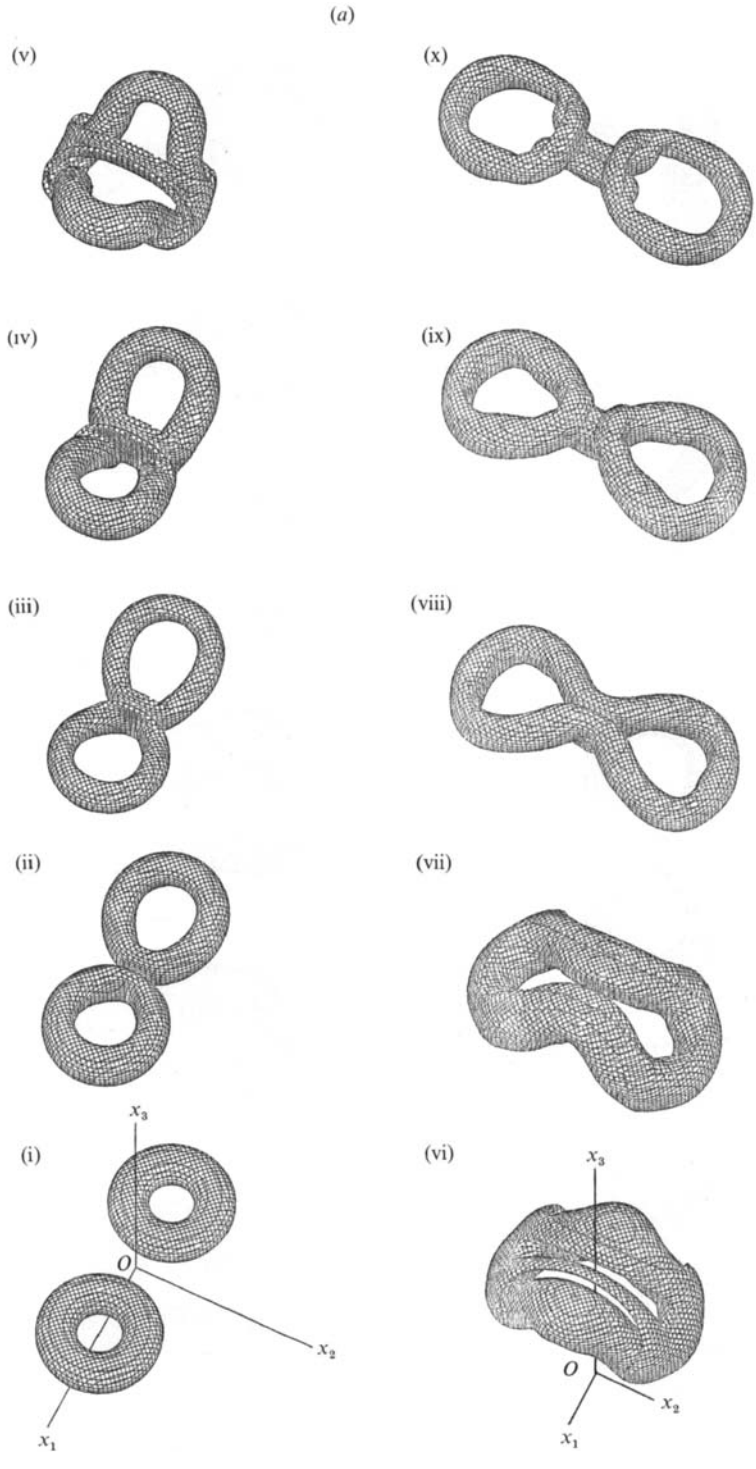

FIGURE 4(*a*). For caption see p. 594.

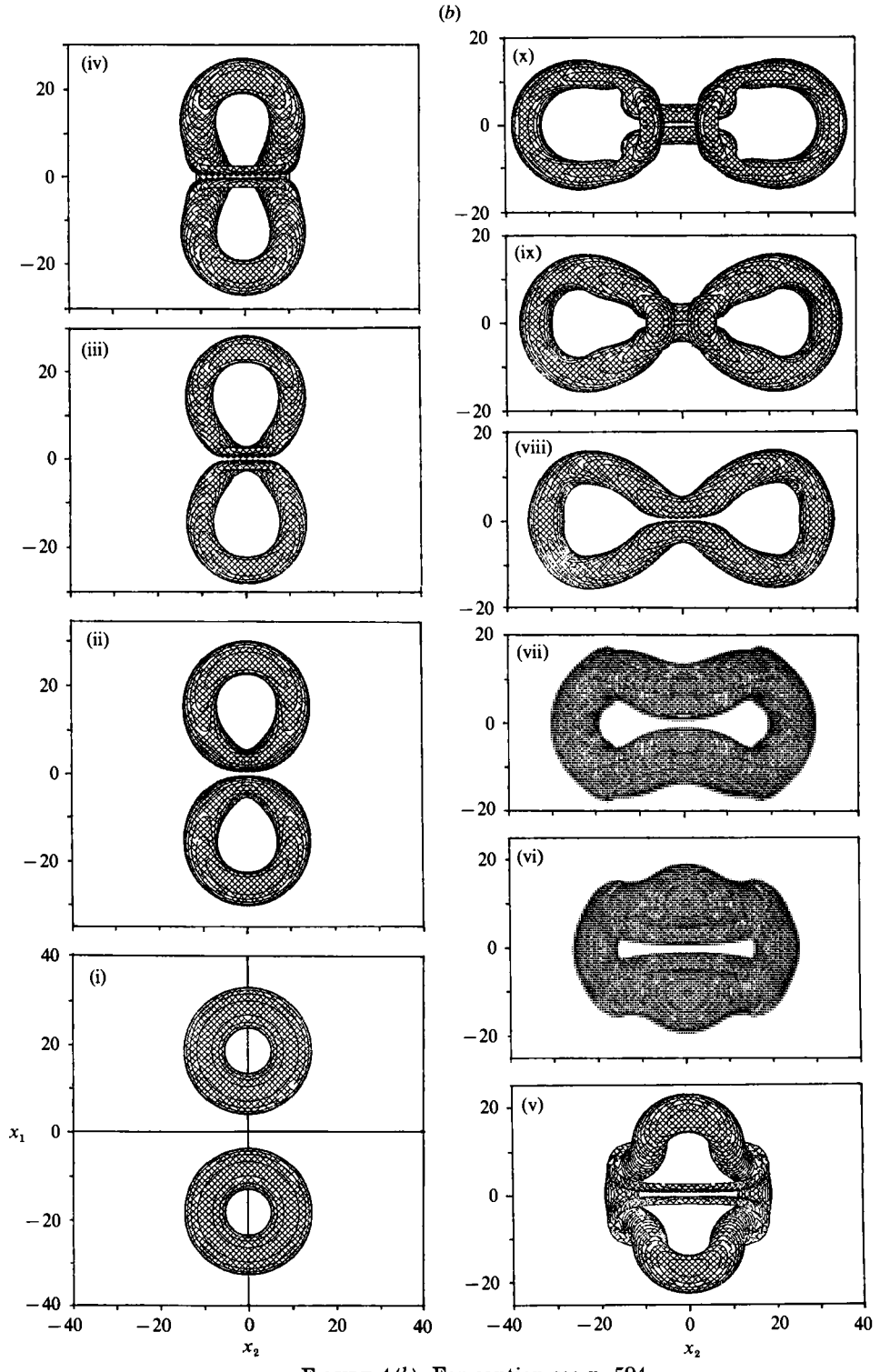

FIGURE 4(*b*). For caption see p. 594.

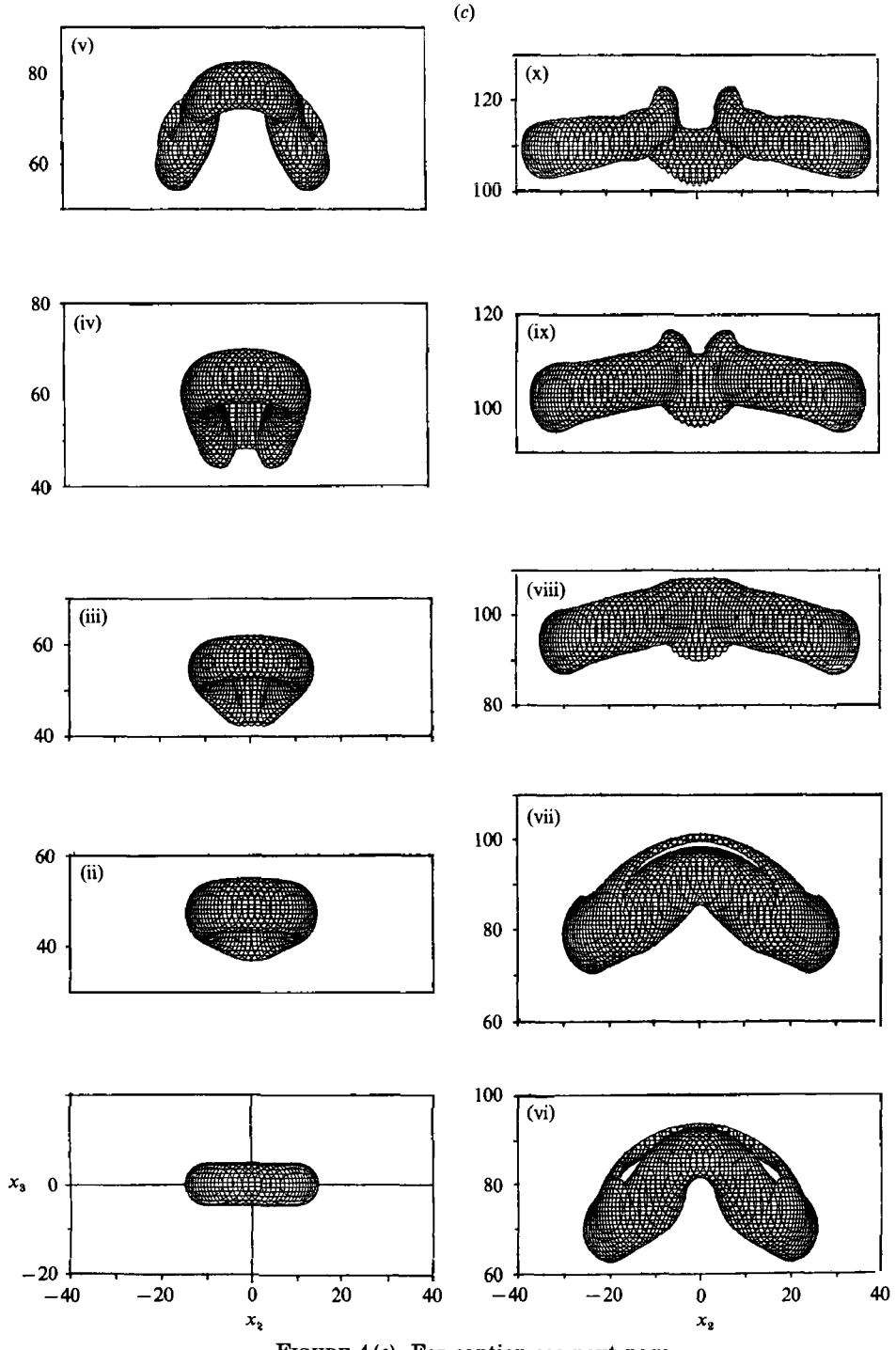

FIGURE 4(*c*). For caption see next page.

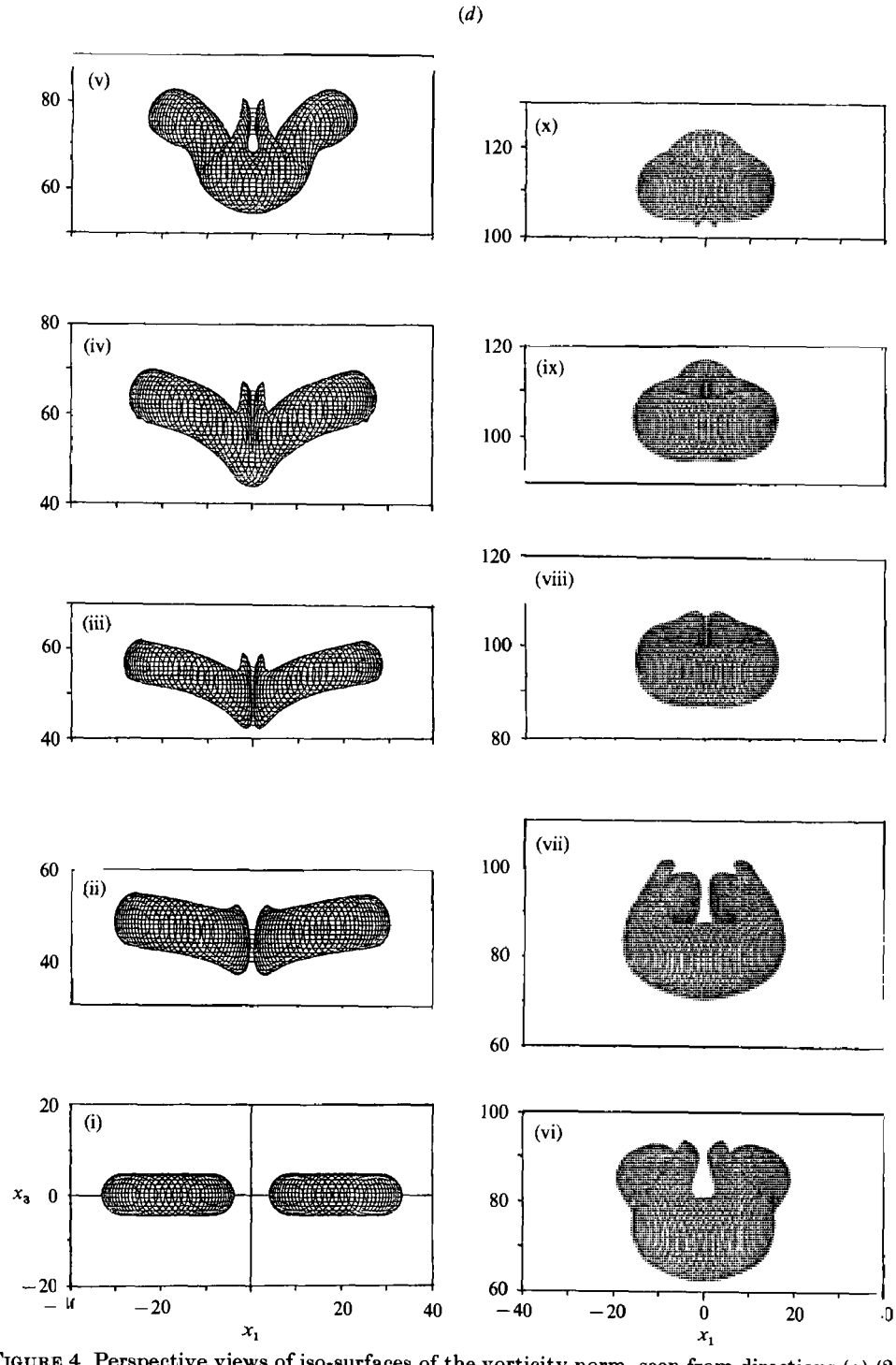

FIGURE 4. Perspective views of iso-surfaces of the vorticity norm, seen from directions (*a*) (2, 1, 5), (*b*) (0, 0, 1), (*c*) (1, 0, 0) and (*d*) (0, −1, 0) for Case I. (*i*) $t = 0$, (*ii*) 3, (*iii*) 3.5, (*iv*) 4, (*v*) 5, (*vi*) 6, (*vii*) 7, (viii) 9, (ix), 10, (x) 11. The surface level of 25% of $|\omega|_{\max}$ is drawn.

becomes larger and therefore induces a higher velocity there, making these parts travel faster. This makes the distorted ring somewhat planar (figure 4*a–d*(viii)). The neck of the gourd shape of the vortex, on the other hand, becomes narrower and narrower, and the facing parts of the ring contact at around $t = 9$ (figure 4*a–d*(viii)), triggering the second reconnection. Two humps appear in front of the vortex tube (figure 4*a–d*(ix)). At each end of the contact line, the facing parts of the tube are linked by bridges to create two circular rings. Again the cancellation of opposite-signed vorticity is not complete and two remnant vortex tubes called *legs* (Kida *et al.* 1989) are left behind the bridges. (A thread and a leg seem to be left by a similar mechanism though they are different in appearance.) The vortex ring at $t = 11$ resembles eyeglasses with a frame and nose-pieces (figure 4*a–d*(x)). The mechanism of these vortex reconnections will be described in more detail in the following subsections.

3.2. *First reconnection*

Figure 5 shows the time development of contours of $-\omega_2$ on the symmetric (x_1, x_3)-plane. The contour levels drawn here are 5, 10, 20, 40 and 80% of $|\boldsymbol{\omega}|_{\max}$. The solid and broken lines represent positive and negative values of $-\omega_2$, respectively. That is, the vortex cores shown by solid lines rotate counterclockwise and those by broken lines clockwise.

The initial circular cores of the vortex tubes are stretched in the x_3-direction and form a tadpole-shape (figure 5*b*, *c*). The mutual induction between the heads, which contains far more circulation than the tail, is much stronger than that between the tails. As a result, the heads move ahead leaving the tails behind. The peak of vorticity in each core is shifted relatively away from the axis of each vortex ring (figure 5*b–d*). This shift of the peaks can be understood qualitatively by considering the conservation of fluid volume in a cross-section of a vortex core with curvature.

The outer cores travel upward faster than the inner cores because the two inner cores are pushed against each other forming a dipole and pulling each other downward by mutual induction. The outer cores ahead of the inner cores induce, at the position of the inner cores, a flow which is converging toward the (x_2, x_3)-plane (the dividing line in figure 5). As a result, the inner cores are further pressed against each other to make a flat dipole. The magnitude of the converging flow due to the outer cores decreases with decreasing x_1 and vanishes on the (x_2, x_3)-plane. Thus, the vorticity is accumulated and steepened in the x_1-direction near the (x_2, x_3)-plane. The dipole would propel itself downward in the absence of any external flow. In the present case, it is advected upward by a strong flow induced by the rest of the vortex tubes.

The so-called head–tail structure of a dipole, which has peaks of vorticity at the front of the dipole (downward in figure 5*f* and upward in figure 5*l–p*) and long tails at the back, is clearly seen at $t = 3.5$ and 8.5–13. This structure has been observed in other configurations such as a head-on collision of two circular vortex rings (Stanaway, Shariff & Hussain 1988), a perturbed anti-parallel vortex pair (MH) and a disturbed Batchelor's dipole (Pumir & Kerr 1987). The head–tail structure was also observed in an inviscid calculation of a head-on collision of two vortex rings (Shariff *et al.* 1988). A common observation in the formation of the head–tail structure is that heads are created at the front of a dipole which is convex in the travelling direction so that the two elements of the dipole tend to approach each other through their self-induction velocity. The formation of the head–tail structure in a dipole through the self-approaching flow will be reported elsewhere (Kida, Takaoka & Hussain 1991). A

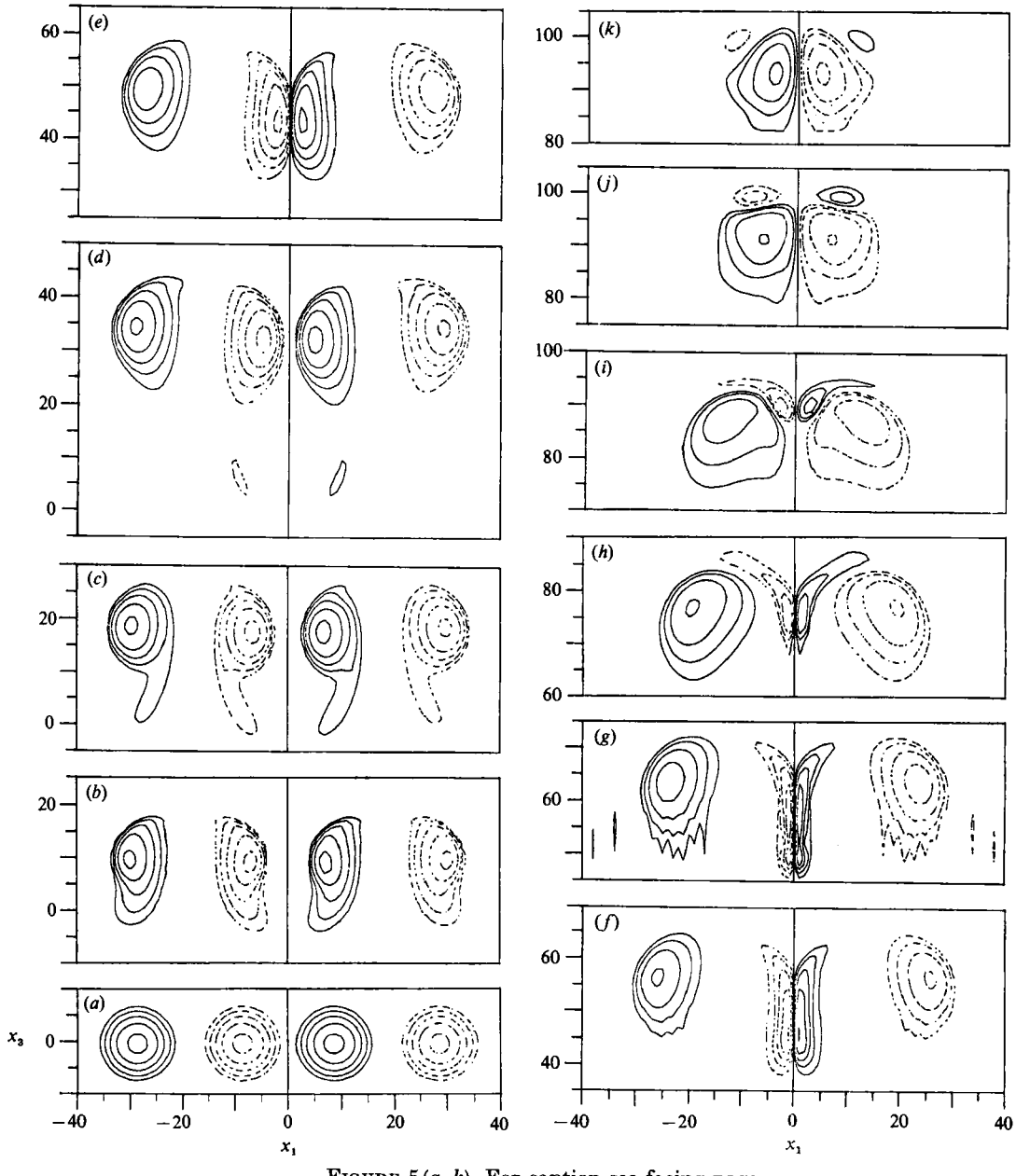

FIGURE 5(*a–k*). For caption see facing page.

close relation between the head–tail structure and the spatial distribution of strain rate will be discussed in §3.3.

Incidentally, a wavy structure in the vortex cores of the dipole, which is symmetric with respect to the (x_2, x_3)-plane (figure 5*g*, *o*), seems to be due to an instability. The characteristics of this instability, such as the symmetry and the lengthscale, are understood qualitatively in terms of the instability of a triangular jet, in which the dipole is replaced by two vortex layers of finite width with uniform vorticity of the same magnitude and opposite sign, and the stability characteristics are known

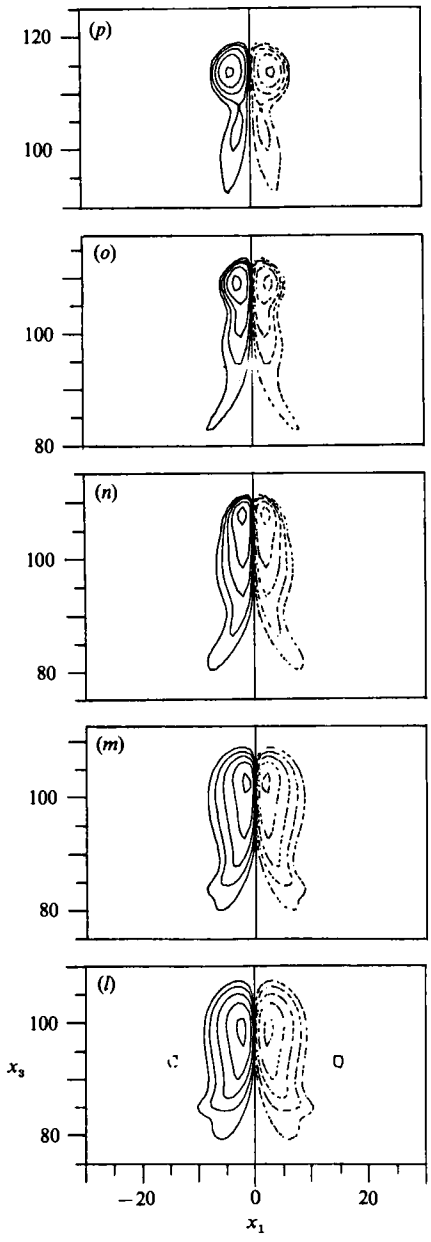

FIGURE 5. Cross-section of vorticity component $-\omega_2$ on the (x_1, x_3)-plane for Case I. (*a*) $t = 0$, (*b*) 0.5, (*c*) 1, (*d*) 2, (*e*) 3, (*f*) 3.5, (*g*) 4, (*h*) 5, (*i*) 6, (*j*) 7, (*k*) 7.5, (*l*) 8.5, (*m*) 9, (*n*) 10, (*o*) 11, (*p*) 13. Solid and broken lines represent positive and negative values, respectively. Levels plotted are 5, 10, 20, 40 and 80% of $|\omega|_{\max}$. Numbers on the axes are the coordinates measured in terms of mesh size.

analytically (see Drazin & Reid 1981, p. 246). A symmetric (with respect to the centreline of the triangular jet) disturbance is linearly unstable in the inviscid case.

The flow converging toward the centreplane keeps the two rings of the dipole together. The opposite-signed vorticity across the symmetry plane is being cancelled on the plane by viscous cross-diffusion. These vortex lines that are cancelled out by diffusion should be connected with the corresponding vortex lines in the other vortex

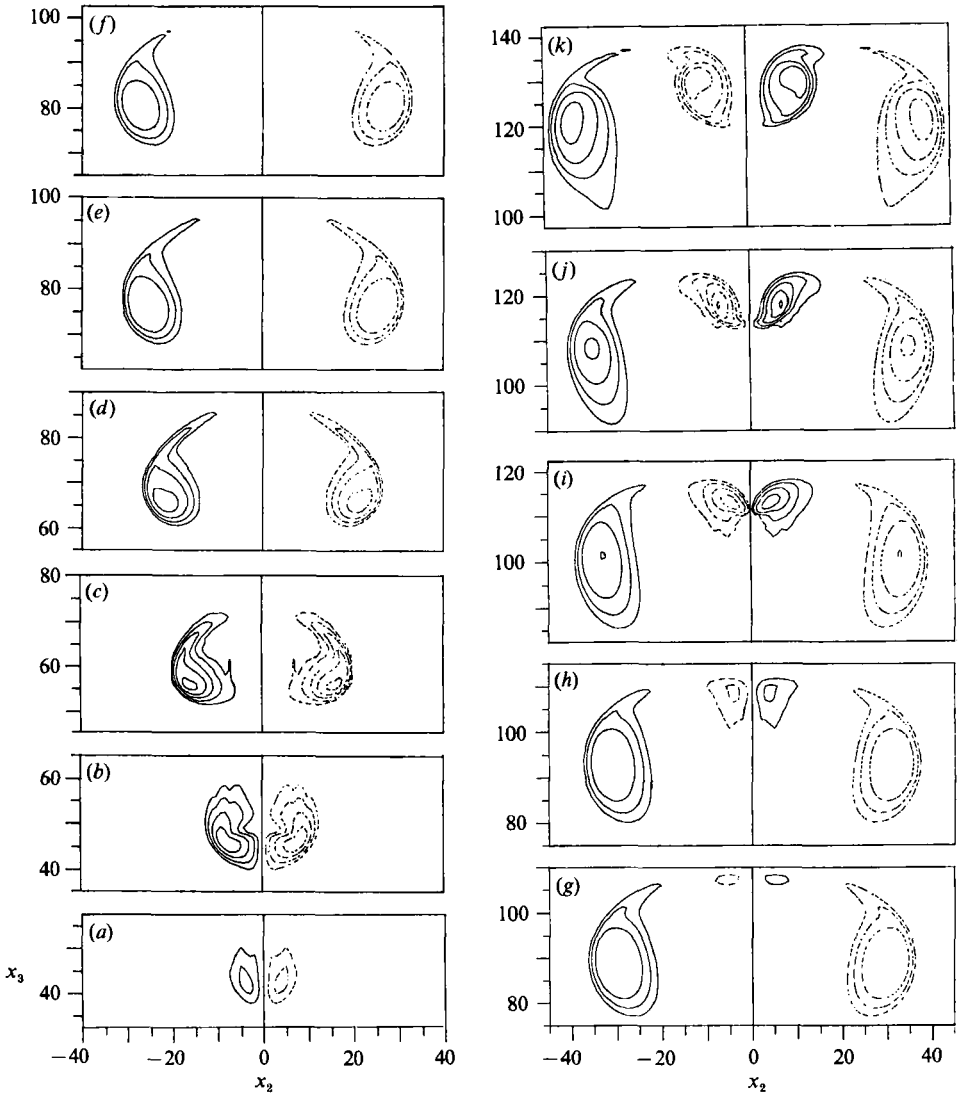

FIGURE 6. Cross-section of vorticity component ω_1 on the (x_2, x_3)-plane for Case I. (*a*) $t = 3.5$, (*b*) 4, (*c*) 5, (*d*) 6, (*e*) 7, (*f*) 7.5, (*g*) 8.5, (*h*) 9, (*i*) 10, (*j*) 11, (*k*) 13. Solid and broken lines represent positive and negative values, respectively. Levels plotted are 5, 10, 20, 40 and 80% of $|\omega|_{\max}$.

tubes, for vortex lines cannot be terminated inside the flow since the vorticity field is solenoidal. Therefore, an x_1-component of circulation appears on the (x_2, x_3)-plane, which exactly equals the amount of the x_2-component which is lost in the (x_1, x_3)-plane by viscous cross-diffusion. The cancellation of vorticity is incomplete, and the uncancelled parts of vorticity, or threads, swirl around the outer cores as a result of the induction by the latter (see figures 4*a–d*(v–vii) and 5*h–l*). The intensity of the threads is being weakened by viscous cross-diffusion between the threads and the main cores. Meanwhile, the outer cores approach each other, which initiates the second reconnection (§3.4).

The time sequence of the contours of ω_1 on the (x_2, x_3)-plane, resulting from bridging (§3.3), is drawn in figure 6. The solid and broken lines represent positive and

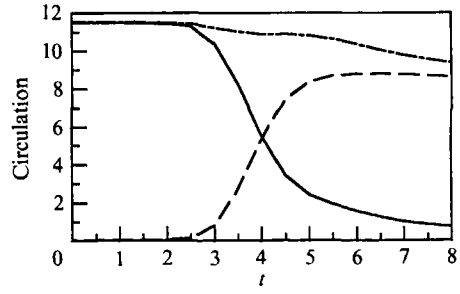

FIGURE 7. Time-development of circulation around interacting vortex tubes during the first reconnection for Case I. ——, Circulation around the cross-section of an inner core on the (x_1, x_3)-plane; — — —, circulation around the cross-section of a bridge on the (x_2, x_3)-plane; – – – –, the sum of the two circulations.

negative values of ω_1, respectively. Again contours are shown for ω_1-values of 5, 10, 20, 40 and 80% of $|\omega|_{\max}$ and $|\omega_1|$ is less than 5% until $t = 3$. The two small islands in figure 6(*a*) are the cross-sections of the newly born bridges. The location and the direction of the initial appearance of the bridges will be discussed in §3.3 in regard to the maximum stretching rate and the stagnation point. The rapid increase of the distance between the two islands results from the approach of the round parts of the main tube which have larger radii. Note that during the formation of bridges their cross-section is not smooth nor well-defined because of continual accumulation of new reconnected vortex lines and their advection around the bridge core (MH). Bridging is nearly complete at $t = 5$, whence the vortex cross-section takes a tadpole shape with the head downward. This form of core cross-section persists during the rest of the simulation. At $t = 8.5$, the second reconnection starts.

The time development of circulation around the cross-section of one of the inner vortex cores in the (x_1, x_3)-plane is plotted by a solid line in figure 7. A broken line represents the circulation around the cross-section of a newly born vortex core, or a bridge, on the (x_2, x_3)-plane (see figure 6*a*), and a dash-dot line the sum of the two circulations. These circulations were calculated by summing the vorticity component, ω_1 or ω_2, on the grid points belonging to the vortex core concerned. The x_2-component of circulation decreases slowly at early times ($t \lesssim 2$), because of the interaction of the edges of the cores which are fattened by viscous diffusion. Around $t = 2.5$, just when the first reconnection occurs, the circulation begins to decay appreciably and loses 80% of its initial value by $t = 4.5$. At the same time, the x_1-component of circulation appears and increases rapidly. During the reconnection, say $2.5 \lesssim t \lesssim 4.5$, 70% of the initial circulation is lost, but the sum of the x_1- and x_2-components remains almost constant in time. The decrease in the sum results from viscous cross-diffusion between the threads and the main vortex tubes as well as between the vortex tubes on the (x_1, x_3)- and (x_2, x_3)-planes. For $t \gtrsim 4.5$, the x_2-component decays rather gradually.

There may be three phases of evolution of two interacting vortex rings, just as observed earlier by MH in two interacting anti-parallel sinusoidal vortex tubes. They are (i) the *inviscid advection* phase in which anti-parallel parts of vortex tubes approach each other by self- and mutual inductions, and the vortex lines are stretched and the cores are flattened to form a dipole with a head–tail structure, (ii) the *bridging* phase in which nearly antiparallel vortex lines are annihilated and linked by viscous cross-diffusion at the interaction zone to create bridges orthogonal to the original vortex tubes, and (iii) the *threading* phase in which the developed bridges

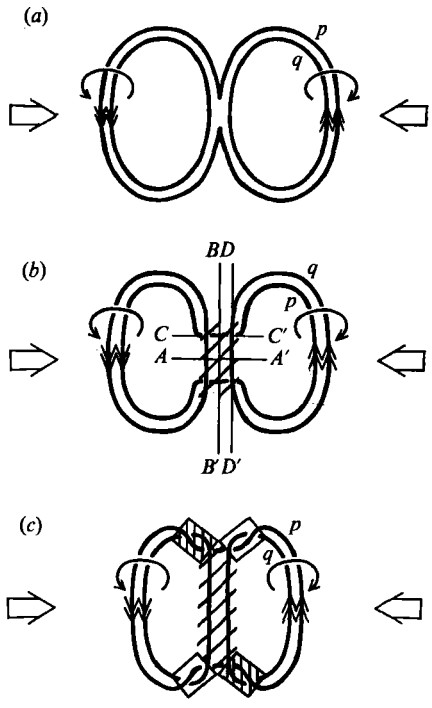

FIGURE 8. Illustration of bridging. Two vortex rings are interacting at the centre. they are pushed from left and right by a converging flow designated by big arrows. Double and round arrows indicate the directions of vorticity and the rotation of vortex lines, respectively. Letters p and q represent the reconnected and unreconnected vortex lines, respectively. The number of reconnected lines increases as time goes on from (*a*) to (*c*). Annihilation of vorticity is taking place in hatched areas. The vortex lines are twisted like right-handed and left-handed screws in the shaded and blank rectangles, respectively.

reverse the curvature of yet-unreconnected parts of the interacting vortex tubes so that the original anti-parallel vortex lines begin to move apart; the reconnection process remains incomplete, leaving threads as remnants of the original tubes. These threads are killed by cross-diffusion with the main core, which is quite different from the case studied by MH. These three phases roughly correspond to periods (i) $0 \leqslant t \lesssim 2.5$, (ii) $2.5 \lesssim t \lesssim 4.5$ and (iii) $t \gtrsim 4.5$.

The interaction time or duration of the bridging phase (ii) depends on how fast the two vortex tubes are pressed against each other. The velocity field around the interaction zone is induced by the vorticity in the interaction zone as well as by the remains of the vortex tubes. In fact, the contribution from the remains of the vortex tubes is dominant in the first reconnection process. Thus, in spite of many attempts at exploration (Schatzle 1987; Takaki & Hussain 1985; Ashurst & Meiron 1987), it is not clear whether the reconnection interaction time can be expressed only in terms of local quantities which characterize the interacting portion of the vortex tubes.

3.3. *Bridging*

The cross-linking of vortex lines in the present reconnection process can be explained by the bridging mechanism observed in the interaction of a pair of anti-parallel sinusoidal vortex tubes (MH). The mechanism of bridging is illustrated in figure 8. (As emphasized by Melander & Hussain (1990), note that vortex lines in a viscous

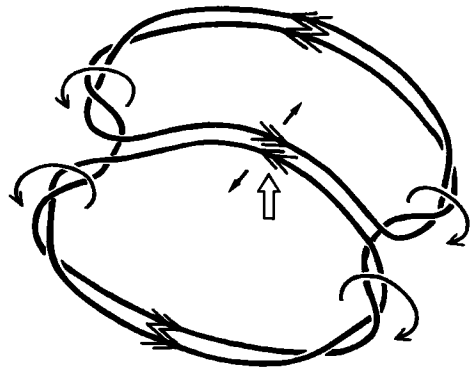

FIGURE 9. Incompleteness of cancellation. A pair of anti-parallel vortex lines at the centre is bent upward by the velocity (a big arrow) induced mainly by vorticity around the bridges, the directions of rotation of which are designated by round arrows. This upward bending of the anti-parallel vortex lines induces self-repelling velocity (small arrows) and causes them to move apart. Double arrows represent the direction of vorticity.

flow are not material lines, although they are treated so throughout this paper. This idealization is helpful in the discussion.) The direction of vorticity is shown by double arrows. The vortex rings rotate in the directions indicated by curved arrows so that they move out of the paper as a whole. The two vortex rings are pushed against each other by self-induction or by an external flow. In the present simulation, the converging flow is generated by the vortex rings themselves, since we have no external flow. (There are image flows because of the periodic boundary condition, but their contribution to the converging flow is small compared with the self-induction velocity of the vortex rings.)

When two vortex rings come into contact, the outermost vortex lines, which are in opposite directions, are cancelled by viscous cross-diffusion in the interaction zone (the hatched areas in figure 8). At the same time, they are connected with their counterparts in the other vortex rings at the ends of the interaction zone (figure 8*a*). We denote by p in figure 8 typical vortex lines which have been reconnected during this process, and by q those lines which have not yet been reconnected. Since the two vortex rings are pushed against each other constantly, the number of reconnected vortex lines increases over time. The vortex lines are rotating around each other in the vortex cores so that lines p and q must be tangled at the ends of the interaction zone (figure 8*b*, *c*). The vortex lines are strongly twisted especially in the regions denoted by rectangles in figure 8(*c*), like right-handed and left-handed screws in shaded and blank rectangles, respectively. This means that super-helicity density is large there if the magnitudes of ω and χ do not vary very much (discussed in §7). The portions of vortex line p that link the two rings are called bridges. With the help of the self-induced velocity the reconnected vortex lines accumulate ahead of the advecting anti-parallel tube pair (i.e. at the back of the rings).

Meanwhile, the cancelling part (the two vertical lines at the centre in figure 8*b*, *c*) of the vortex rings is bent by the velocity field induced by the upper and lower parts of the vortex rings in such a way that its centre moves out of the paper. This in turn causes the two vertical lines, which are curved in planes perpendicular to that of the paper, to move apart due to the reversed self-induction velocity, and prevents further cancellation. This situation is illustrated from another angle in figure 9. The direction of rotation of vortex rings, which induces an upward velocity (a big arrow)

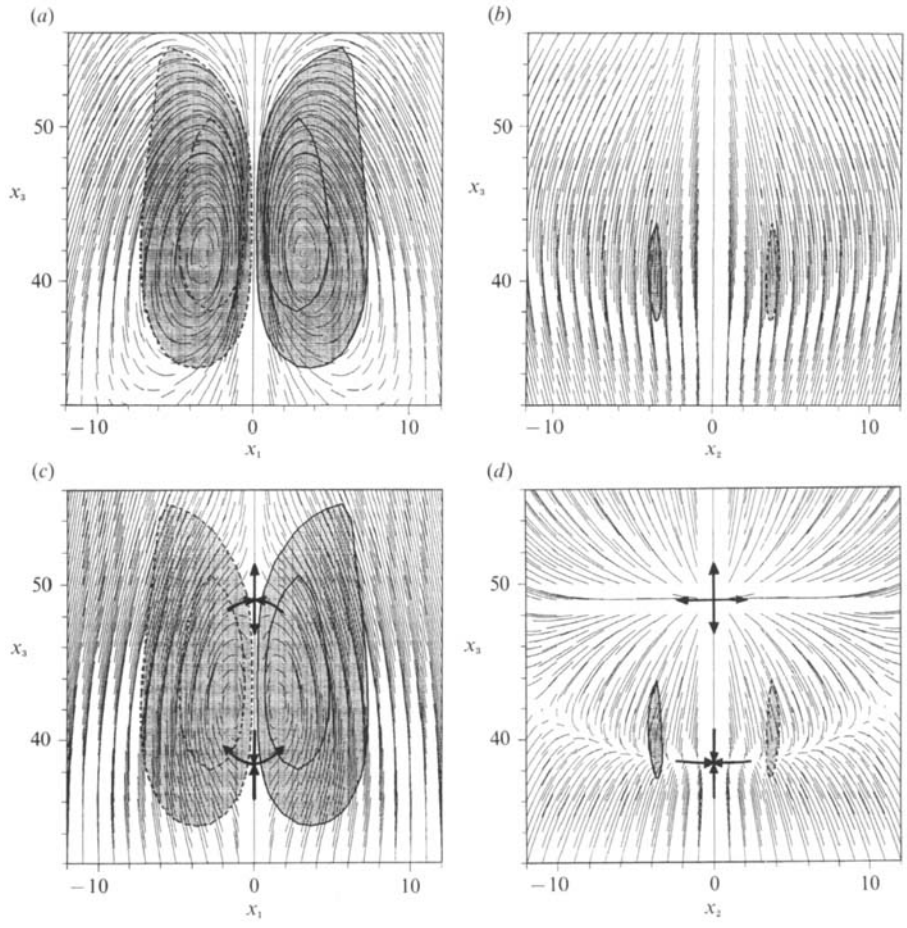

FIGURE 10. Streamlines and contours of vorticity components ($-\omega_2$ in the (x_1, x_3)-plane in (a, c), and ω_1 in the (x_2, x_3)-plane in (b, d)) in moving frames at $t = 3$ for Case I. Frames (a, b) are moving with the vortex dipole $(+1.0)$, and (c, d) with the bridges (-1.3). Thin curves are parallel to the velocity vectors on the planes. The contour levels drawn are $\pm 10\,\%$ and $\pm 40\,\%$ of $|\omega|_{max}$ for (a, c), and $\pm 2\,\%$ for (b, d). Thick solid and broken lines denote positive and negative values. Arrows on the centrelines indicate the direction of the flow around the stagnation points.

at the centre is indicated by curved arrows. This upward velocity bends the anti-parallel vortex lines upward. These curved vortex lines have self-induced velocity away from the mid-plane and move apart in the directions indicated by small arrows. Thus, the cancellation is always incomplete and some uncancelled vorticity is left behind as threads. The degree of incompleteness of cancellation or the amount of remnant circulation depends upon the shape of the vortex rings during the reconnection as well as upon viscosity. This will be discussed further in §4.

The mechanism of formation of bridges, the vortex reconnection, has been discussed in relation to streamlines or stagnation points by MH. Before discussing our new explanation of bridging in terms of vortex stretching rate, it may be appropriate to give here some comments on their argument concerning streamlines.

The streamlines on planes parallel and perpendicular to the vortex dipole at $t = 3$ for Case I are drawn in frames moving with two different velocities in figure 10. Figure 10(a, c) represents the streamlines in the (x_1, x_3)-plane which corresponds to

line AA' in figure 8(*b*). These are in frames with the dipole and the bridges, respectively. The translational velocity of the dipole (or bridges) is estimated from the weighted mean velocity, $\int \boldsymbol{u}|\omega_2|\,\mathrm{d}\boldsymbol{x}/\int|\omega_2|\,\mathrm{d}\boldsymbol{x}$ (or $\int \boldsymbol{u}|\omega_1|\,\mathrm{d}\boldsymbol{x}/\int|\omega_1|\,\mathrm{d}\boldsymbol{x}$), where the integration is performed over the whole domain of figure 10(*a*) (or *b*). In these figures the trajectories of fluid particles which start at the regular grid points are drawn by integrating them along the velocity vectors at this time. The length of each curve is proportional to the magnitude of velocity there. The curves are parallel to the velocity vectors. Since each curve starts from one of the regular grid points, it is easy to identify the direction of velocity. The velocity component normal to this plane is identically zero because of symmetry. The contour of vorticity $-\omega_2$ is superimposed to show the position of the dipole. The contour levels are ± 10 and $\pm 40\%$ of $|\boldsymbol{\omega}|_{\max}$. A fluid particle in the right-hand half of the dipole rotates counterclockwise and in the left-hand half clockwise. It takes about 0.84 time units for a typical fluid particle in the dipole, the mean radius of trajectory of which is about 2 mesh lengths, to go around the core once. Thus, the interacting core undergoes one or more turns during the first reconnection, $3.5 \lesssim t \lesssim 4.5$, say.

There are two stagnation points on the centreline, one above and the other below the dipole. Their locations, however, are very different in figures 10(*a*) and 10(*c*). In fact, they are located outside figure 10(*a*). The direction of the flow around the stagnation points is indicated by arrows in figure 10(*c*). The direction of the flow around the lower stagnation point is the reverse of around the upper stagnation point. According to MH, those vortex lines that are advected by the velocity field (in a frame moving with the dipole) and come close to the centreline between the two stagnation points are transported along the centreline to the lower stagnation point. These vortex lines, which are almost perpendicular to this plane, are advected and accumulate at the lower stagnation point to make a bridge. This argument may, however, suffer from several difficulties. First, the streamlines in a moving frame do not generally represent the motion of vortex lines unless the flow is steady. Second, the stagnation point is not a sink in this plane, so that vorticity does not necessarily accumulate there. Third, the velocity field is not Galilean invariant so that the shape of the streamlines and the position of stagnation points are frame-dependent (cf. figures 10*a* and 10*c*). Fourth, there is ambiguity in determining the velocity of the reference moving frame for an unsteady vortex dipole (or anti-parallel vortex tubes) since the vorticity distribution over the dipole varies in time. There may be several ways to determine the 'velocity' of the dipole. Actually, as will be described below, a bridge is created closer to the point of largest vortex stretching rate (equation (3.3)).

Figures 10(*b*) and 10(*d*) show the streamlines and the contours of the normal component of vorticity ω_1 on the (x_2, x_3)-plane (BB' in figure 8*b*) on the same moving frames as figures 10(*a*) and 10(*c*), respectively. The contour level of vorticity is $\pm 2\%$ of $|\boldsymbol{\omega}|_{\max}$. The two islands represent embryos of bridges. The bridges are rather close to the lower stagnation point in figure 10(*d*) but not in figure 10(*b*). This is trivial because figure 10(*d*) is a frame moving with the bridges themselves. In figure 10(*d*), the upper stagnation point in the (x_1, x_3)-plane is regarded as a source in the (x_2, x_3)-plane, and the lower stagnation point as a sink. The flow is converging in two orthogonal directions (x_2 and x_3) and diverging in one direction (x_1) at the lower stagnation point. The flow is directed downward everywhere between these two stagnation points in the symmetry (x_2, x_3)-plane.

We have also examined the behaviour of the streamlines both on the (x_1, x_3)-plane and on a plane passing through a bridge with other estimations of the velocity of the

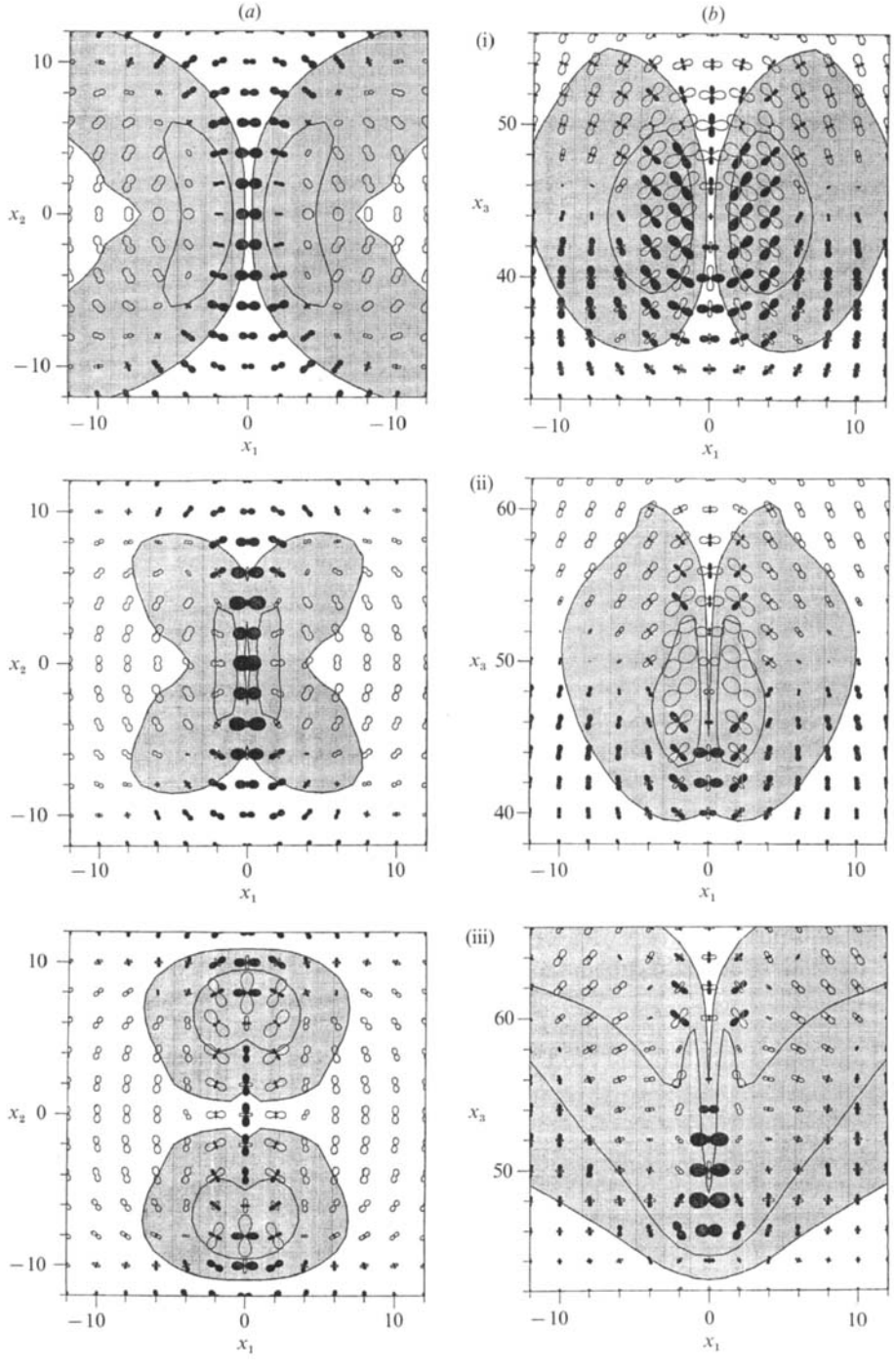

FIGURE 11 (a, b). For caption see facing page.

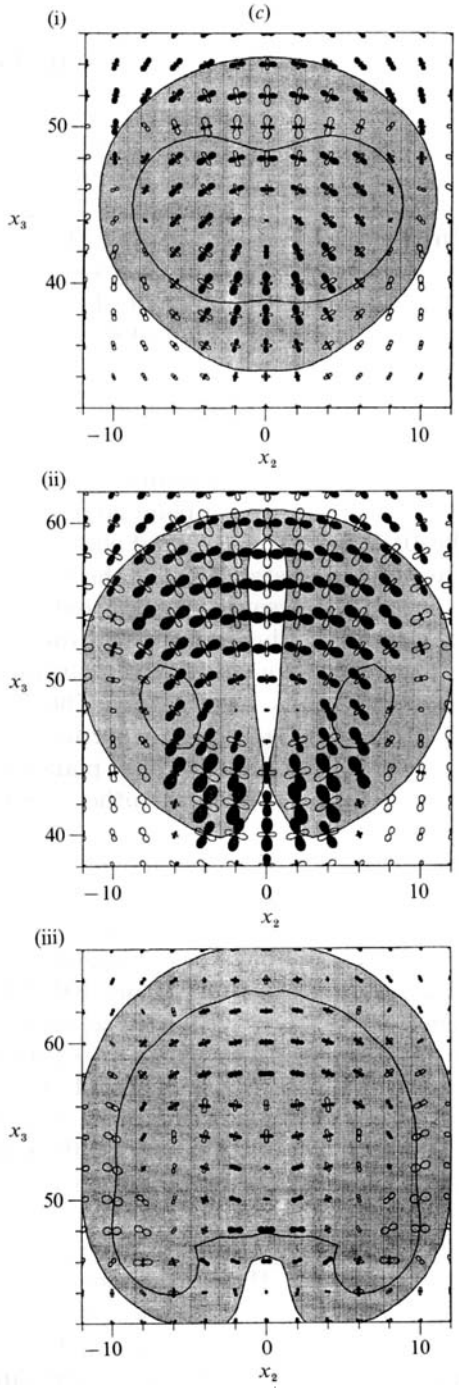

FIGURE 11. Angular dependence of stretching rate on planes parallel to (*a*) the (x_1, x_2)-plane, (*b*) the (x_1, x_3)-plane and (*c*) the (x_2, x_3)-plane for Case I. (i) $t = 3$, (ii) 3.5, (iii) 4. The planes are (*a*) (i) $x_3 = 40\Delta x$, (*a*) (ii) $x_3 = 43\Delta x$, (*a*) (iii) $x_3 = 46\Delta x$, (*b*) (i) $x_2 = 4\Delta x$, (*b*) (ii) $x_2 = 4\Delta x$, (*b*) (iii) $x_2 = 8\Delta x$, (*c*) (i) $x_1 = 4\Delta x$, (*c*) (ii) $x_1 = 4\Delta x$, and (*c*) (iii) $x_1 = \Delta x$. The planes in (*a*) and (*b*) pass through bridges, while those in (*c*) a thread. The distance from the centre of a butterfly or a dumbbell shape to a point of its periphery is proportional to the stretching rate in the direction of the point seen from the centre. The black and blank areas denote respectively positive and negative values of stretching rate. The 10% and 40% levels of contours of the vorticity norm are superimposed for reference.

dipole, that is, by integrating the weighted velocity over regions in which vorticity magnitude exceeds several thresholds. For larger values of the thresholds, the velocity of the dipole is closer to that of the bridges, and therefore the lower stagnation point comes near the position of the bridges.

The rate-of-strain tensor

$$s_{ij} = \frac{1}{2}\left(\frac{\partial u_i}{\partial x_j} + \frac{\partial u_j}{\partial x_i}\right), \quad i,j = 1,2,3, \tag{3.1}$$

is a measure of deformation of a fluid element in a flow. This is a useful indicator of the vortex stretching. The stretching rate of a fluid element is a function of the direction as well as of the position of the element. Let $\hat{\boldsymbol{e}}$ be a unit vector. The stretching rate of a fluid element in the direction of $\hat{\boldsymbol{e}}$ is expressed as

$$s(\hat{\boldsymbol{e}}) = \hat{\boldsymbol{e}} \cdot \boldsymbol{s} \cdot \hat{\boldsymbol{e}} = \sum_{i,j=1}^{3} e_i s_{ij} e_j. \tag{3.2}$$

Figure 11 shows the angular and spatial distributions of the stretching rate on planes parallel to (*a*) the (x_1, x_2)-plane, (*b*) the (x_1, x_3)-plane and (*c*) the (x_2, x_3)-plane at (i) $t = 3$, (ii) 3.5 and (iii) 4. The 10% and 40% levels of contours of the vorticity norm are superimposed for reference. The distance from the centre of a butterfly or a dumbbell shape to a point on its periphery is proportional to the stretching rate in the direction of the point seen from the centre. The directions of positive and negative stretching rates, or the expanding and contracting directions, are differentiated by black and blank regions, respectively. The x_3-coordinates of planes parallel to the (x_1, x_2)-plane (figure 11*a*) and the x_2-coordinates of planes parallel to the (x_1, x_3)-plane (figure 11*b*) are chosen so that these planes pass through bridges (*CC'* in figure 8*b*). The planes of figure 11(*c*), on the other hand, are chosen to focus on a thread (*DD'* in figure 8*b*).

Along the x_2-axis in figure 11*a*(i) we see that fluid elements are being stretched in the direction of the x_1-axis and the stretching rate is maximum at $x_2 \approx \pm 4\Delta x$, Δx being the mesh-size ($= 2\pi/64$). This is more clearly shown in the vortex stretching rate (see (3.3) and figure 12 below). These positions of largest stretching rate coincide with the x_2-coordinates of the initial bridges (see figure 10*b*). As time goes on, (i)→(iii), the high-stretching region moves away from the x_2-axis. By comparing these positions with the cross-section of the bridges (figures 6*a–c*), we find that the bridges are moving apart while being stretched during this period. At $t = 4$ (figure 11*a*(iii)), we see that fluid elements are being stretched along the x_2-axis for $|x_2| \lesssim 4\Delta x$, where no substantial vorticity is left after the viscous cross-diffusion. This stretching of fluid particles along the x_2-axis is caused by the induction velocity of the main part of the approaching vortex rings.

Figure 11*b*(i) also has some interesting features. The fluid elements at the lower half of the x_3-axis are being stretched in the x_1-direction. The x_3-coordinate of the largest stretching rate is about $40\Delta x$, which agrees with the x_3-coordinate of the centre of a bridge (see also figure 10*b*). It is clear in figure 11(*b*)(ii, iii) that the bridge evolves where the stretching is strongest. Another interesting feature of figure 11(*b*)(i) is the spatial distribution of the stretching direction. Notice that it points horizontally in the lower half of the x_3-axis, but vertically in the upper half. This distribution of the stretching rate may have a close relation to the head–tail structure of an interacting vortex dipole mentioned at the beginning of this section. The head is widened by the horizontal stretching, while the tail is extended by the vertical stretching (Kida *et al.* 1991).

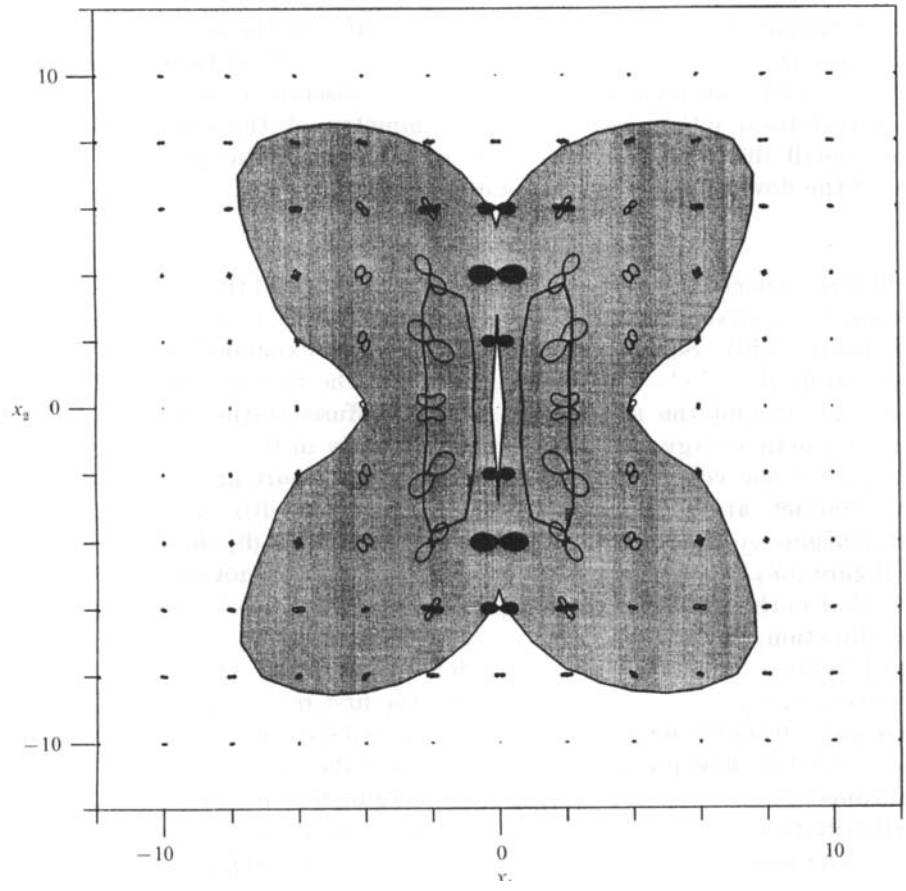

FIGURE 12. Angular dependence of the vortex stretching rate on the same plane ($x_3 = 43\Delta x$) as in figure 11(*a*)(ii). $t = 3.5$.

Figure 11(*c*) represents the structure of a thread. Look at the top centres of figure 11(*c*) where a thread is located. The fluid elements there are being stretched in the x_2-direction. Although we can only see a thread in figure 11(*c*)(ii) at these contour levels, it is clear that the thread is actually being stretched.

The spatial distribution of the stretching rate of fluid elements is expressed by $s(\hat{\boldsymbol{e}})$, but a more appropriate quantity for vortex stretching rate may be

$$s_\omega(\hat{\boldsymbol{e}}) = (\boldsymbol{\omega}\cdot\hat{\boldsymbol{e}})\, s(\hat{\boldsymbol{e}}). \tag{3.3}$$

In figure 12 we plot the angular dependence of $s_\omega(\hat{\boldsymbol{e}})$ on the same plane as in figure 11(*a*)(ii) at $t = 3.5$. It is now clear that vorticity is intensified most strongly at $x_2 \approx \pm 4\Delta x$ where the initial bridges are created.

It is interesting to compare the present numerical results with Schatzle's (1987) laboratory experiment, which is one of the most extensive experiments of the interaction of two vortex rings. First, we note that the vorticity distribution across vortex tubes is nearly Gaussian in his experiment (figures A.5 and A.6 in Schatzle 1987), which is used as the initial condition of our numerical simulation. Unfortunately, a precise comparison is impossible because the initial conditions (the ratio of R and D for example), the Reynolds number and the Schmidt number are

different in his experiment and our numerical simulation. Nevertheless, we find that the spatial distribution of the rate of strain is qualitatively the same at least on the symmetry plane ($x_1 = 0$) (cf. our figure 11*b*(i) and frames 16 of figures 6.6, 6.9 and 6.11 in Schatzle 1987). An asymmetric flow structure observed in his experiment may have developed from either unavoidable asymmetry of the equipment or uncontrollable small disturbances. This is in contrast with the persistence of the symmetry of the flow in our numerical simulation.

3.4. *Second reconnection*

After the first reconnection is over, a distorted vortex ring and the two threads move further along the x_3-axis, changing their shape in a rather complicated manner (figure 4*a*, *b*(vi), (vii)). Some parts of the ring are expanded and others are compressed, while the whole tube is being twisted. The threads left after the first reconnection go around the main tube and are diffused rather rapidly. Viscous dissipation of kinetic energy also occurs more intensely in the threads (§5).

The portions of the vortex tubes that were farthest apart at the initial instant come into contact at around $t = 9$ (see figure 4*a–d*(viii)). Then the second reconnection begins. Around this time we again have a vortex dipole with a head–tail structure (figure 5*m*). Notice, however, that the direction of motion of the dipole is opposite to that in the first reconnection (figure 5*f*, *m*). The dipole now moves in the positive x_3-direction.

As stated before, the details of the vortex reconnection are also affected by vorticity outside the interaction region. During the first reconnection, the vorticity distribution away from the interaction region induces a strong converging flow at the interaction zone. This flow presses the two vortices of the dipole closer and increases the rate of cancellation. Remember that the converging flow is caused mainly by the vorticity distribution of the outer part of the vortex tubes parallel to the interaction zone. During the second reconnection, however, there is no such parallel part of the vortex tube and therefore no strong converging velocity is induced in the interaction zone. Only the self-induced velocity squashes the dipole. As a result, the approach of the interacting vortex tubes is slow, and so is the reconnection. The turnover time of a typical fluid particle in a core is 1.07, so that it rotates in the core four times during $9 \lesssim t \lesssim 13$ (from (viii) to (x) in figure 4*a–d*). Remember that a fluid particle rotates in the core only once during the first reconnection (§3,3). The mechanism of the second reconnection is essentially the same as that of the first. However, because it is slower, we can probe its details.

As seen in figure 4(*a–d*(viii)), two closest portions of the vortex tube come into contact at $t \approx 9$. Vortex lines reconnect to create bridges orthogonal to the interacting anti-parallel parts of the vortex ring (see two humps on both sides of the interaction region in figure 4*a–d*(ix)). A large amount of vorticity is left uncancelled and takes the form of 'connecting rods of an eye glass'. This uncancelled part is called a leg (Kida *et al.* 1989), which corresponds to the thread at the first

---

FIGURE 13. Streamlines and contours of vorticity components normal to planes in a frame moving with the bridges at $t = 9$ for Case I, where the velocity of the moving frame is 1.5 upward: (*a*) the (x_1, x_3)-plane and (*b*) the (x_2, x_3)-plane. Thin curves are streamlines. The contour levels drawn are $\pm 20\,\%$ and $\pm 40\,\%$ of $|\omega|_{\max}$ for (*a*), and $\pm 10\,\%$ for (*b*). Thick solid and broken lines denote positive and negative values. Arrows on the centrelines indicate the direction of the flow around the stagnation points.

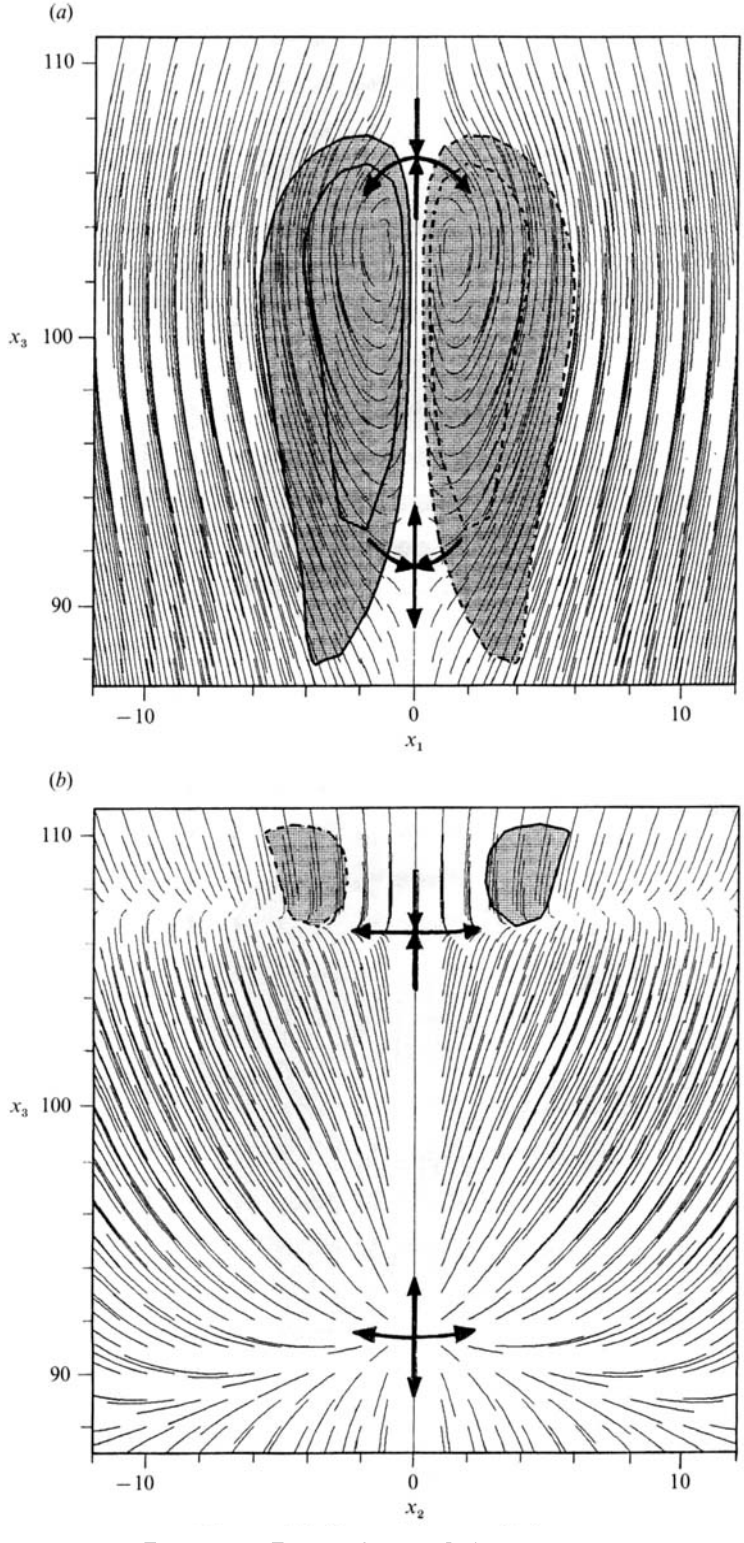

FIGURE 13. For caption see facing page.

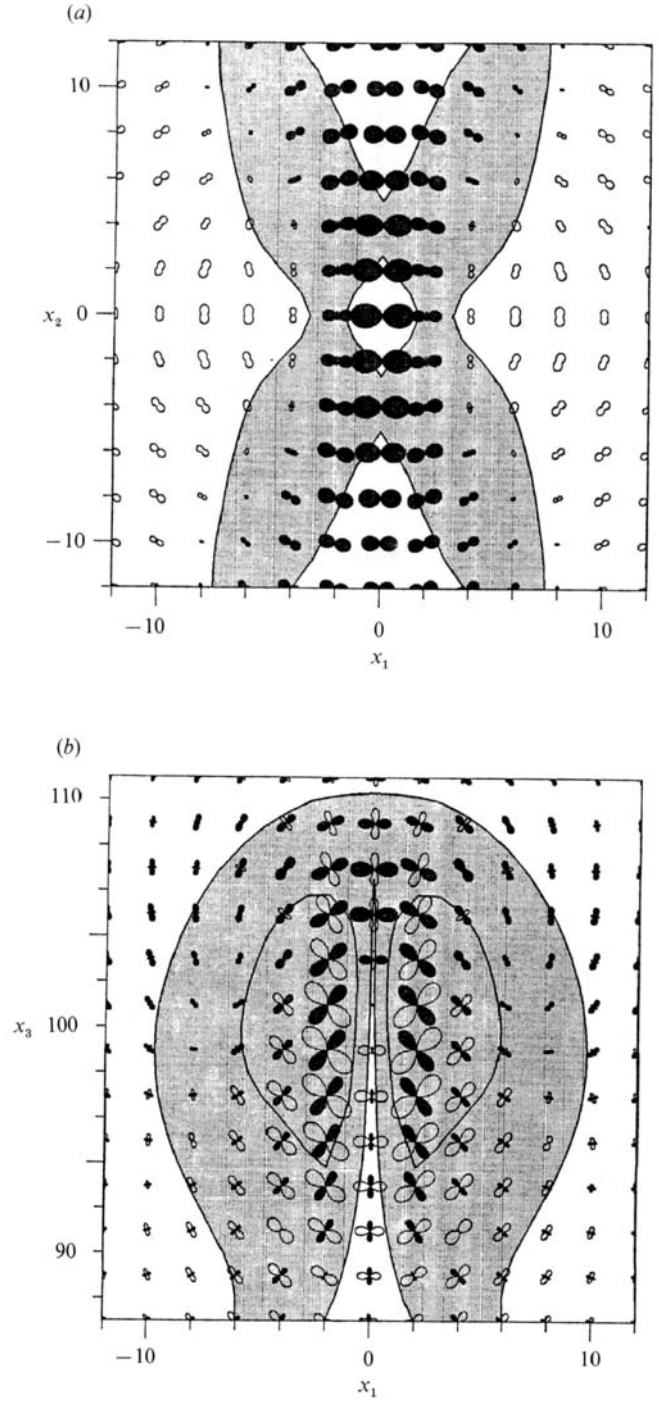

FIGURE 14. Angular dependence of the stretching rate on planes parallel to (*a*) the (x_1, x_2)-plane and (*b*) the (x_1, x_3)-plane at $t = 9$ for Case I. (*a*) $x_3 = 108\Delta x$, (*b*) $x_2 = 4\Delta x$. These planes are chosen so that they pass through bridges. The 10% and 40% levels of contours of the vorticity norm are superimposed for reference.

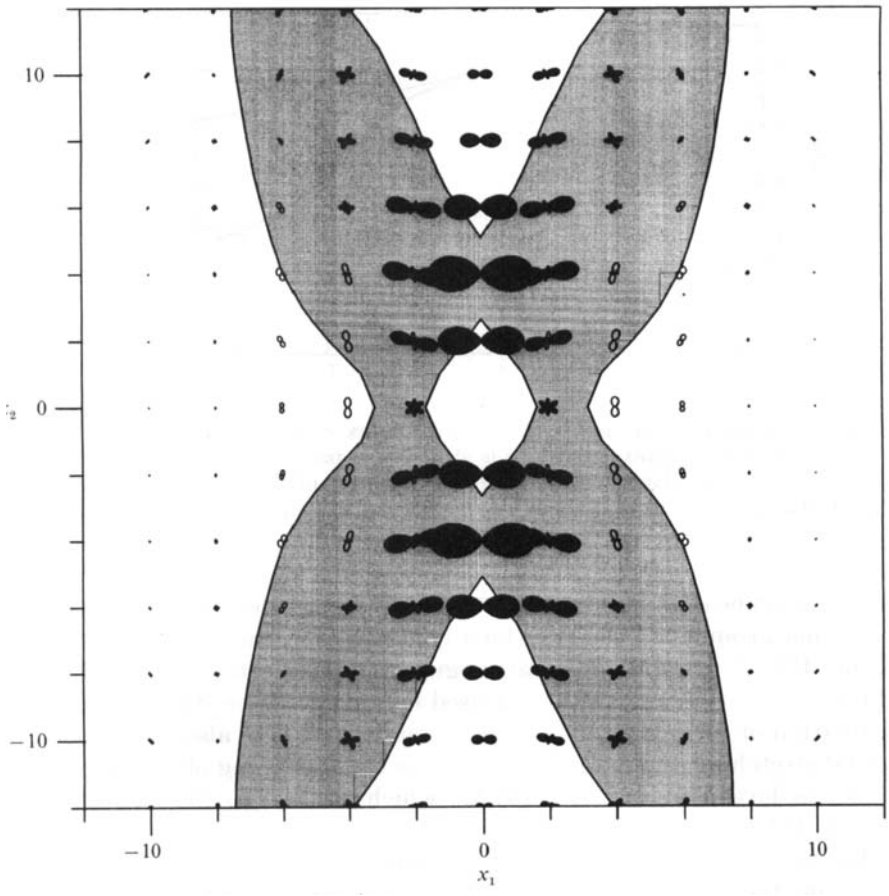

FIGURE 15. Angular dependence of the vortex stretching rate on the same plane ($x_3 = 108\Delta x$) as in figure 14(*a*). $t = 9$.

reconnection. The mechanism of bridging is the same as that illustrated in figure 8 (but the direction of vorticity there should be reversed).

The streamlines and vortex contours on the (x_1, x_3)- and the (x_2, x_3)-planes at the beginning of the second reconnection ($t = 9$) are shown in figures 13(*a*), 13(*b*), respectively. These graphs are similar to the corresponding ones for the first reconnection in the frame moving with the bridges (see figures 10*c*, *d*), except for several differences. The direction of the head–tail structure, or the sign of vorticity in the cores, is opposite. The stagnation points are a saddle and a source on the (x_1, x_3)-plane (figure 13*b*), the former corresponding to the sink at the bottom centre in figure 10(*d*). The appearance of either a stagnation point or a sink may be explained by considering the intensity of bridges and the curvature of the main vortex tube (Pumir & Siggia 1987). The locations of stagnation points in the frame moving with the dipole are far from those of the bridges, as we saw in figure 10(*a*, *b*).

In figure 14(*a*, *b*) is plotted the angular dependence of stretching rate $s(\hat{\boldsymbol{e}})$ at $t = 9$ on planes parallel to the (x_1, x_2)- and the (x_1, x_3)-planes, respectively. These planes are chosen to cross the centre of a bridge. As seen in figure 14(*a*), fluid elements in the vicinity of the x_2-axis are being stretched in the x_1-direction. To see the spatial distribution of vorticity intensification, we plot in figure 15 the vortex stretching rate

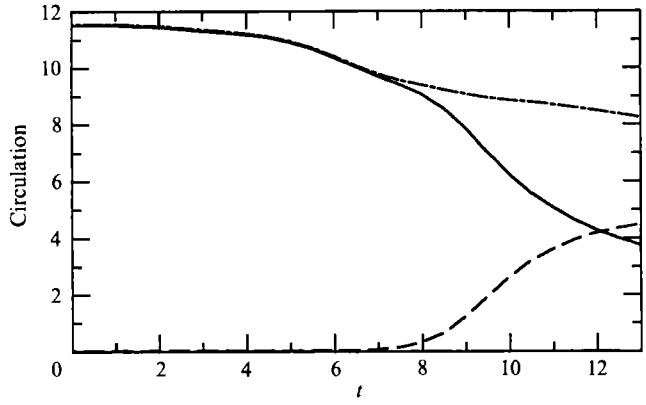

FIGURE 16. Time-development of circulation around vortex cores for Case I: ——, circulation around the cross-section of a vortex core which is identified as one of the outer cores on the (x_1, x_3)-plane at $t = 0$; — — —, circulation around the cross-section of a bridge on the (x_2, x_3)-plane which is identified as an inner core in figure 6(*g–k*); – – – –, the sum of the two circulations.

$s_\omega(\hat{\boldsymbol{e}})$ on the same plane as in figure 14(*a*) at $t = 9$. It is seen that the vortex stretching rate has maxima around $|x_2| = 4\Delta x$, which coincide with the x_2-coordinates of the bridges (figure 13*b*). The stretching rate in figure 14(*b*) has a structure similar to that in figure 11(*b*)(i), and the same argument used before about the stretching of bridges and the formation of the head–tail structure can be used here also. Notice here that the horizontal stretching at top centre represents the stretching of a bridge and that its magnitude is larger around $x_3 = 107\Delta x$, which is close to the positions of the bridges (figure 13*b*).

The bridges grow at the expense of the vorticity of the anti-parallel part of the tube. Meanwhile, the vorticity in the growing bridges becomes strong enough to push back the legs to the minus x_3-direction to reverse the curvature of the legs so that they move apart. Because there is no external converging flow to maintain the reconnection, it stops at an early stage, leaving more uncancelled vorticity than in the first reconnection.

The time-development of the circulation around a vortex core in the (x_1, x_3)-plane which is identified as one of the outer cores in figure 5(*a*) is plotted by a solid line in figure 16. A broken line represents the circulation around a cross-section of a bridge in the (x_2, x_3)-plane (one of the inner cores in figure 6*g–k*), and a dash-dot line denotes the sum of the two circulations. The circulation in the (x_1, x_3)-plane decreases rather gradually until $t \approx 8.5$ when the second reconnection takes place. Then it beings to decrease more rapidly, and at the same time circulation in the (x_2, x_3)-plane appears. This shows that the x_2-component of vorticity is transferred to the x_1-component during the second reconnection. The sum of these two circulations should be constant if cross-diffusion occurred only at the interaction zone where the bridges are created. However, the cross-diffusion between vortex rings of adjacent periodic boxes is non-negligible, which leads to the decrease of the total circulation.

Let us discuss the time-development of the maximum of vorticity norm $|\boldsymbol{\omega}|$, which has been used for reference levels in our vorticity contour plots. The instantaneous maxima of vorticity norms on the two symmetry planes are shown in figure 17(*a*). Here circles and triangles represent the maxima in the (x_1, x_3)- and (x_2, x_3)-planes, respectively. The x_1-coordinate of the point of the maximum on the (x_1, x_3)-plane is

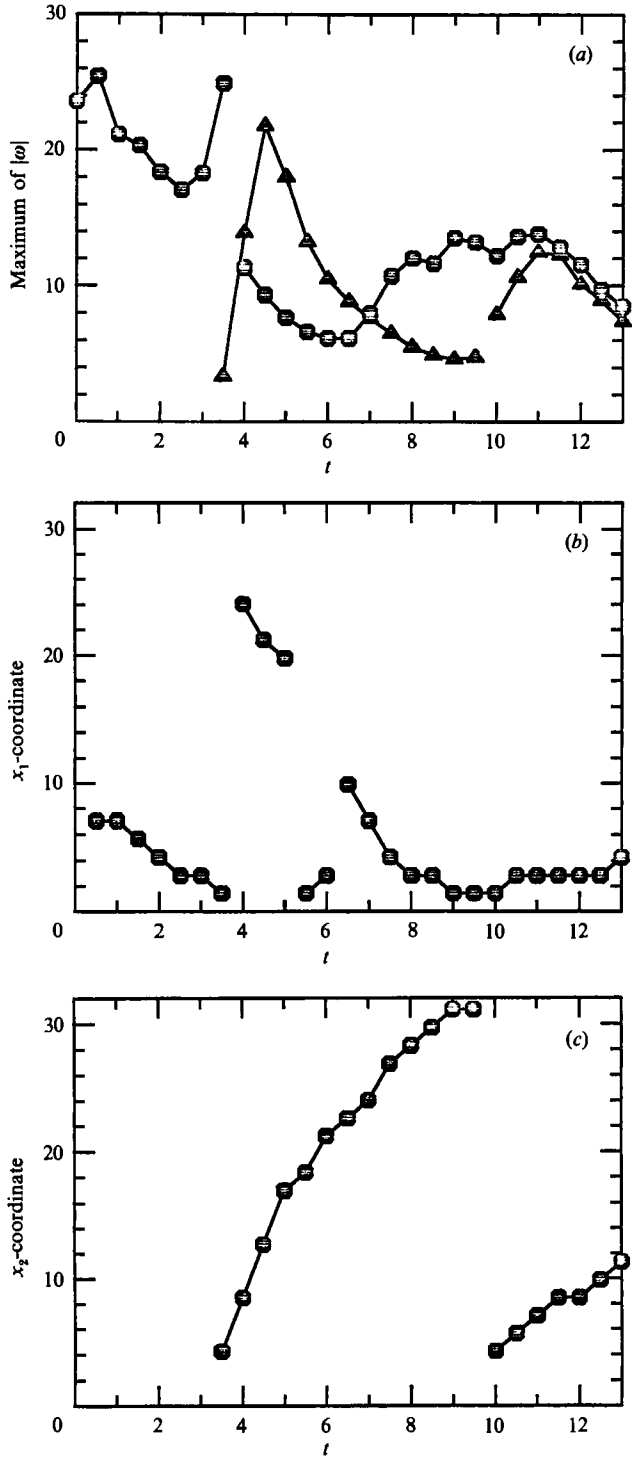

FIGURE 17. (*a*) Time-development of the maxima of $|\omega|$ on the (x_1, x_3)-plane (circles) and on the (x_2, x_3)-plane (triangles) for Case I. (*b*) The x_1-coordinate of the position of the maximum on the (x_1, x_3)-plane. (*c*) The x_2-coordinate of the position of the maximum on the (x_2, x_3)-plane.

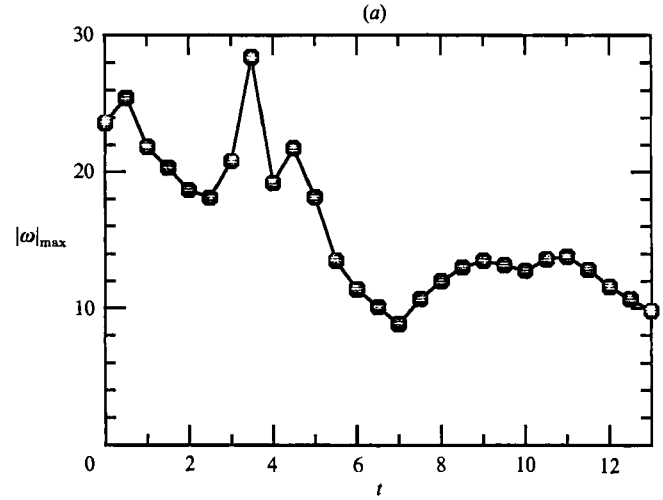

FIGURE 18(a). For caption see facing page.

plotted in figure 17(b), and the x_2-coordinate of the point of the maximum on the (x_2, x_3)-plane in figure 17(c). The behaviour of these maxima can be understood easily with reference to figures 5 and 6. Note that there are several local maxima in each symmetry plane; we must discriminate which gives the absolute maximum. In figure 17(a) the maxima at different points are not connected.

The initial increase of the maximum on the (x_1, x_3)-plane, which is located in the inner cores in figure 5, results from the vortex stretching due to the mutual induction velocity. The increase, however, is stopped at an early stage of evolution ($t \approx 0.5$) owing to viscous diffusion. It decreases until $t \approx 3$ when the two vortex rings begin contact. The rapid increase from $t = 3$ to 3.5 is a result of a strong stretching of vortex cores at the beginning of the first reconnection (§3.2). As seen in figure 17(b), the maximum is still in the inner cores. The strong cancellation of vorticity in the inner core during the first reconnection, however, leads to a rapid decrease of vorticity there. As a result, the peaks in the outer core dominate for a while ($4 \lesssim t \lesssim 5$). After this time, as seen in figure 17(b), the cores in which the maximum occurs alternate a few times, but the maximum value itself does not exhibit any sharp jump. Another increase around $t = 8$ is due to the vortex stretching in the approaching vortex cores just before the second reconnection, and a rapid decrease after $t \approx 11$ is due to viscous diffusion in legs.

The maximum on the (x_2, x_3)-plane begins to increase very rapidly from $t \approx 3.5$ as newly born bridges grow in the first reconnection. As seen in figure 17(c), the x_2-coordinate of the maximum increases very rapidly. This, of course, corresponds to the rapid expansion of the vortex ring in the x_2-direction (see figure 4b(v–vii)). The growth of the maximum in the (x_2, x_3)-plane ceases at around $t = 4.5$, meaning that the stretching of the bridges is no longer effective. Thereafter, the vorticity decreases by viscous diffusion until the second reconnection occurs. Another cross-over happens when the intensity of the new bridges born in the second reconnection (inner cores in figure 6g–k) dominates that of the outer cores, indicated by a jump in figure 17(c) at $t \approx 10$. After $t \approx 11$, this maximum decreases again, i.e. the bridges are no longer being stretched and neither are the legs.

The absolute maximum $|\omega|_{max}$ of the vorticity norm in the whole field is plotted in

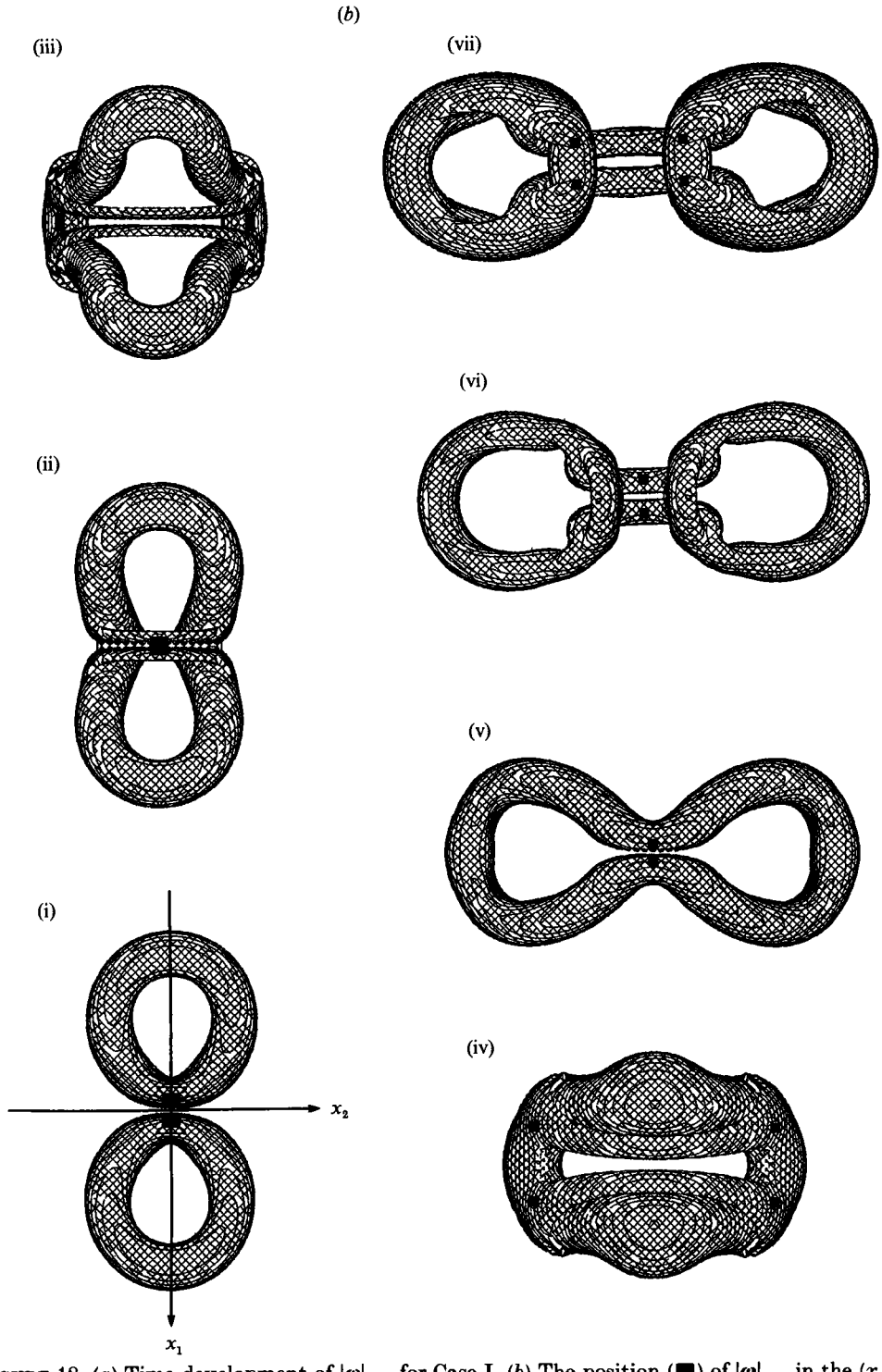

FIGURE 18. (*a*) Time-development of $|\omega|_{\max}$ for Case I. (*b*) The position (■) of $|\omega|_{\max}$ in the (x_1, x_2)-plane. The iso-surfaces of vorticity norm at the level of 25% of $|\omega|_{\max}$ are drawn for reference. (i) $t = 3$, (ii) 4, (iii) 5, (iv) 6, (v) 9, (vi) 11, (vii) 13.

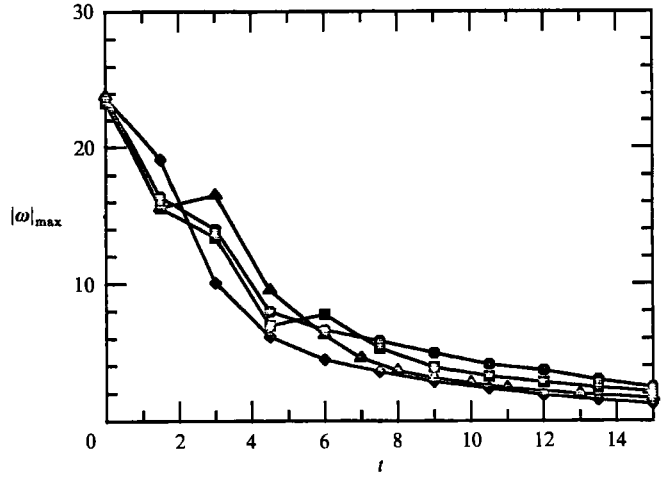

FIGURE 19. Time-development of $|\omega|_{max}$: ■, Case II; ●, Case III; ▲, Case IV; and ◆, Case V.

figure 18(*a*). This, being by definition larger than the two maxima in figure 17(*a*), is very close to the envelope of the two maxima. The x_1- and the x_2-coordinates of the position of the maximum are plotted by solid squares in figure 18(*b*). The positions of the maxima move as follows. In the inviscid advection phase of the first reconnection they are located in the inner cores at the closest point to the (x_2, x_3)-plane, where vortex lines are strongly stretched (figure 18*b*(i)). Then, in the bridging phase, they are lying in the threads (figure 18*b*(ii)). Up to this time they are on the symmetry (x_2, x_3)-plane. But, in the threading phase ($4.5 \lesssim t \lesssim 7$) they are shifted to the roots of the bridges, where the interaction between the bridges and the main tube is very active. The points of maxima move away from the (x_2, x_3)-plane together with the roots of the bridges. Meanwhile, the distorted main tube comes into contact with itself in the (x_1, x_3)-plane. In the advection phase ($7 \lesssim t \lesssim 9$) of the second reconnection the maximum points are on the nearest portion of the interaction zone. They shift to the legs in the bridging phase ($9 \lesssim t \lesssim 11.5$) and then to the roots of legs in the threading phase.

The calculation was finished at $t = 13$ because the vortex ring is stretched too much in the x_2-direction by this time, and the interaction among the rings in the adjacent boxes may not be negligible any more. What will happen after $t = 13$? According to more extensive simulations starting from smaller vortex tubes (Cases II–V, see §4), the change over time of the vortex shape is very slow and no interesting topological change has been observed.

4. Effects of initial conditions

We have seen so far that two circular vortex rings which start side by side on a common plane (the inclination angle $\theta = 0°$) undergo two successive vortex reconnections. These reconnection processes are governed by the characteristics of the flow at the interaction zone and are influenced by the entire shape of the vortex rings. In this section, we consider the dependence on the initial conditions of the characteristics of the reconnection processes.

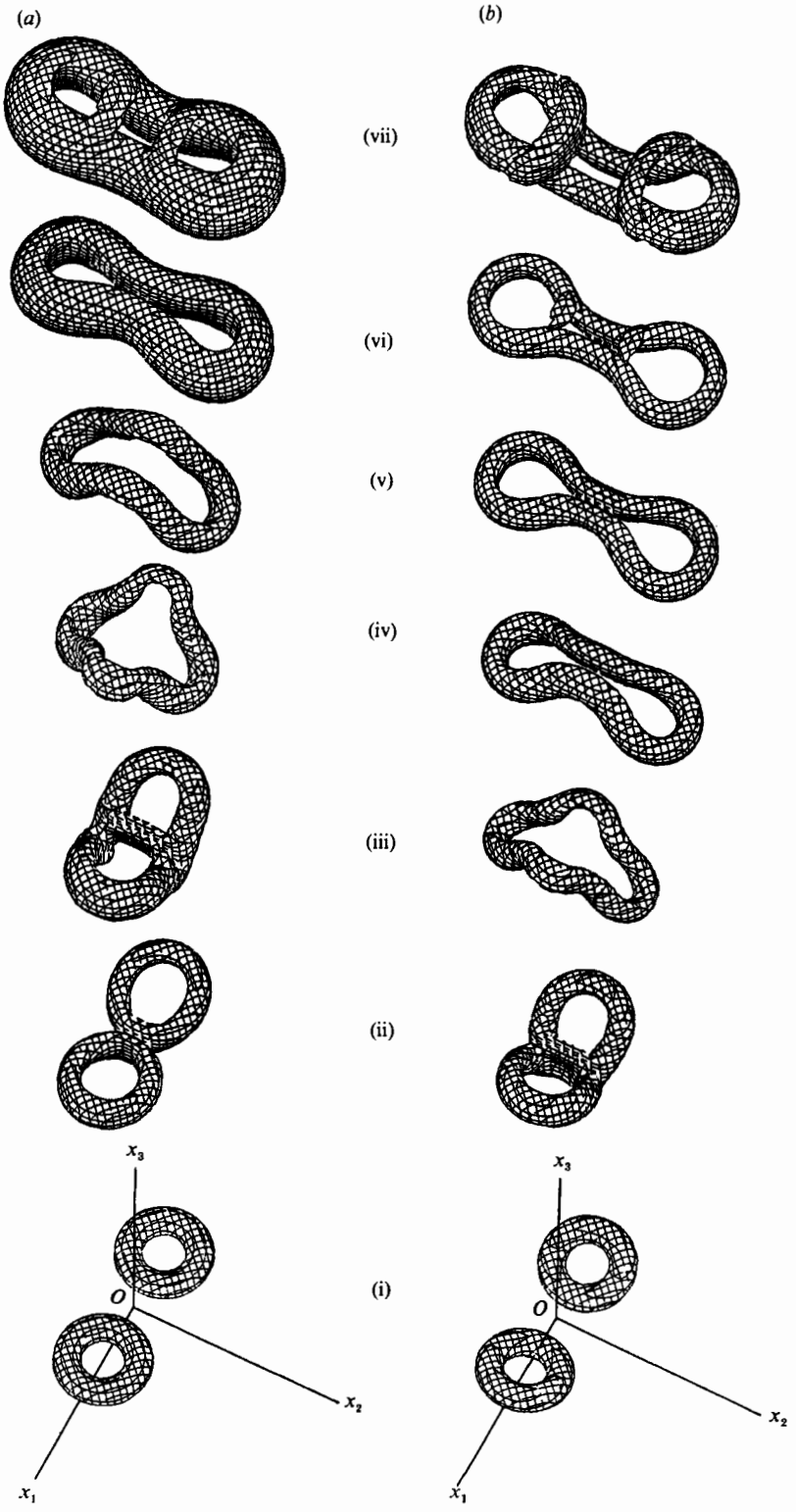

FIGURE 20 (*a*, *b*). For caption see page 619.

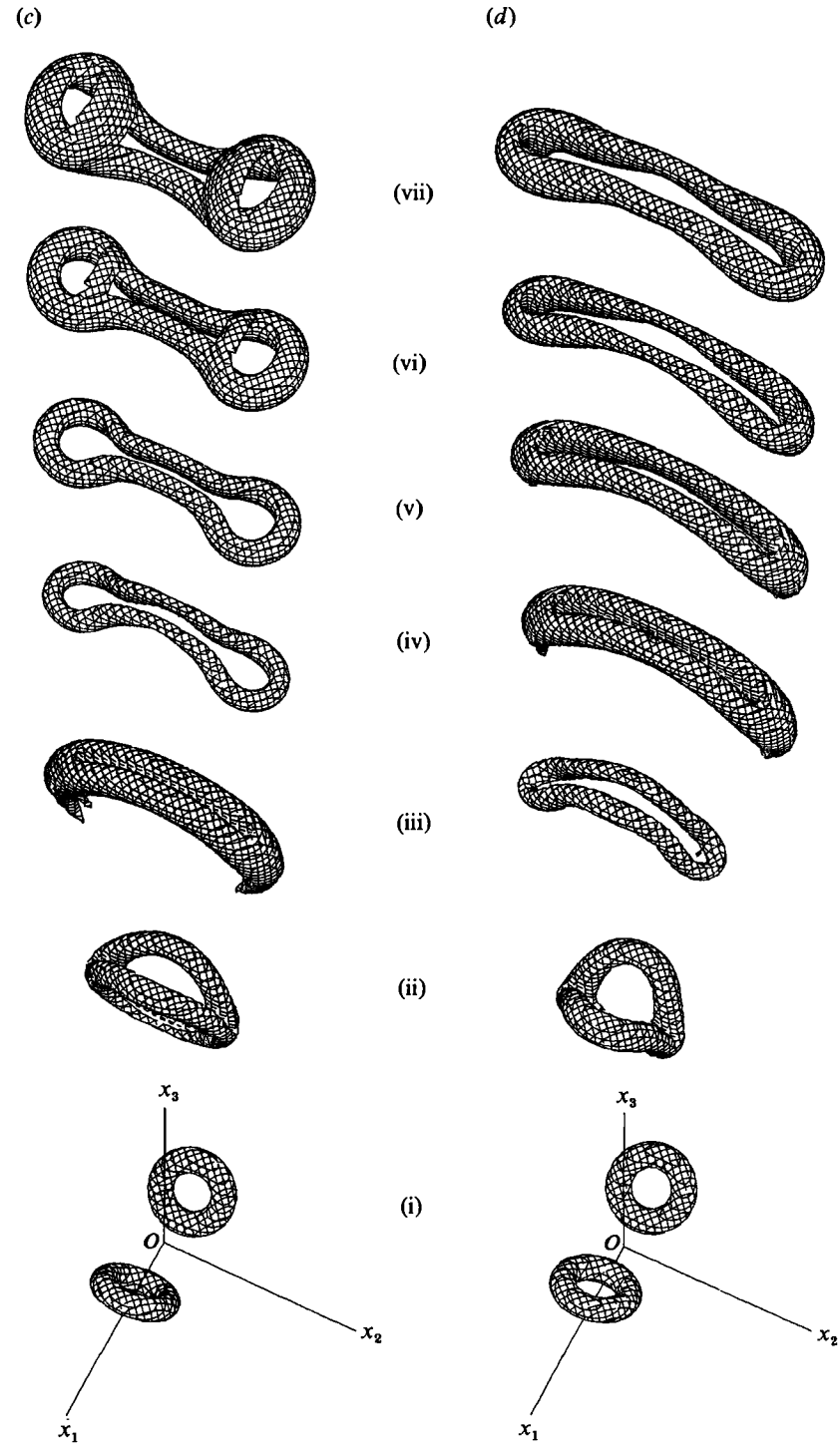

FIGURE 20 (*c*, *d*). For caption see facing page.

4.1. *Initial inclination angle*

In order to examine the dependence of the phenomenon on the initial conditions we have simulated flows with four different inclination angles: $\theta = 0°$, 15°, 30° and 45° (see figure 3). To reduce undesirable interactions with vortex rings in the adjacent periodic boxes we halved the sizes of the vortex rings and the distance between the centres of the rings (§2). This reduction requires larger viscosity (smaller Reynolds number) to maintain the accuracy of the calculation. The cut-off error due to truncation of the Fourier modes can be conveniently monitored by looking at the behaviour of the energy spectrum around the cut-off wavenumber (§5). The parameters used in each run are listed in table 1.

The time-development of $|\omega|_{\max}$ is shown for Cases II–V in figure 19. Although the details of the time variation are different, it decays rather similarly for different cases. These values of maximum vorticity norm will be used for the reference levels in the plots of vorticity given below.

Figure 20 shows the iso-surfaces of the vorticity norm $|\omega|$ at several representative times for Cases II–V. They are seen from the (2, 1, 5)-direction.

4.2. *Effect on first reconnection*

All four cases undergo the first reconnection. Not surprisingly, the time at which their interaction begins is earlier for larger initial inclination angle θ. The occurrence of a vortex reconnection and the degree of completeness of cancellation depend not only on the characteristics of the interacting parts of the vortex rings but also on the velocity field around the interaction zone. Since the velocity field is determined by the entire distribution of vorticity, the global shape of vortex rings affects the reconnection process. Among other factors, the curvature of an interacting nearly anti-parallel vortex pair and the strength of the converging velocity field at the interaction zone are crucial in determining the completeness of reconnection. As seen in figure 20, the global shape of the vortex ring is different for different initial inclination angles. It is interesting in particular to note that the degree of completeness of cancellation of vorticity does not change monotonically with angle θ but cancellation is most effective at some angle between 0° and 45°.

To see the structure of the vortex core just after the first reconnection, we plot in figure 21 the cross-section of vorticity component $-\omega_2$ on the (x_1, x_3)-plane for Cases II–V. The solid and broken lines represent the positive and negative values, respectively. The remnants of the interacting vortex dipole, or threads, are advected around two main vortex cores. For small initial inclination angles ($\theta = 0°$ and 15°) we see two small cores, which originate from the tail of the interacting dipole, being advected upwards between two main cores (figure 21*a*, *b*). For a large angle ($\theta = 45°$, figure 21*d*), on the other hand, an interacting dipole with a head–tail structure appears below the main cores. Interestingly, for an intermediate angle ($\theta = 30°$, figure 21*c*), we can see that the head and tail are separate.

FIGURE 20. Perspective view of the iso-surfaces of the vorticity norm seen from the (2, 1, 5)-direction. (*a*) Case II: (i) $t = 0$, (ii) 3, (iii) 4.5, (iv) 6, (v) 7.5, (vi) 12, (vii) 18. The levels plotted are 40% of $|\omega|_{\max}$ at $t = 0$, 3, 6, 12 and 18, and 50% at $t = 4.5$ and 7.5. (*b*) Case III: (i) $t = 0$, (ii) 1.5, (iii) 3, (iv) 4.,5, (v) 6, (vi) 7.5, (vii) 10.5. 40% level at $t = 0$, 1.5, 3 and 10.5, and 50% at $t = 4.5$, 6 and 7.5. (*c*) Case IV: (i) $t = 0$, (ii) 1.5, (iii) 3, (iv) 4.5, (v) 6, (vi) 7.5, (vii) 10.5. 40% level at $t = 0$, 1.5 and 3, and 50% at $t = 4.5$, 6, 7.5 and 10.5. (*d*) Case V: (i) $t = 0$, (ii) 1.5, (iii) 3, (iv) 4.5, (v) 6, (vi) 7.5, (vii) 10.5. 40% level at $t = 0$, 1.5, 3 and 10.5, and 50% at $t = 4.5$, 6 and 7.5.

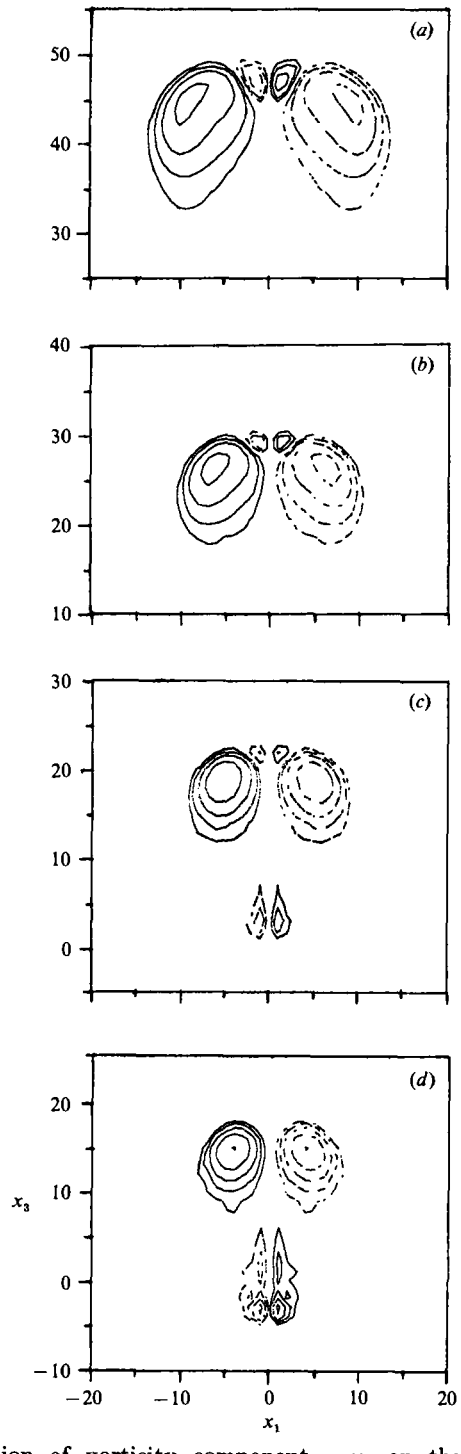

FIGURE 21. Cross-section of vorticity component $-\omega_2$ on the (x_1, x_3)-plane after the first reconnection. (*a*) $t = 6$ for Case II, (*b*) $t = 3$ for Case III, (*c*) $t = 2$ for Case IV, and (*d*) $t = 1.5$ for Case V. Solid and broken lines represent positive and negative values, respectively. The levels plotted are 5, 10, 20, 40 and 80% of $|\omega|_{max}$.

Case	θ (deg.)	Head	Tail	Sum	t
I	0	—	0.27†	0.27†	6
II	0	—	0.13	0.13	6
III	15	—	0.07	0.07	3
IV	30	0.16	0.04	0.20	2
V	45	0.52	—	0.52	1.5

TABLE 2. Remnant circulation. († Divided by 4 to compare with the other cases (see §2).)

The remnant circulation in a thread after the first reconnection is listed in table 2. By comparing Cases II–V, we see that the remnant circulation in the tail part decreases with θ, whereas that in the head increases. The sum of the two circulations is a minimum at $\theta = 15°$, indicating that vorticity cancellation is most efficient at this angle though it is never complete.

This dependence of remnant circulation on the initial inclination angle can be explained qualitatively by considering the relative positions of the inner and outer cores in the (x_1, x_3)-plane. Remember that the inner cores are pressed together by a converging flow induced by the outer cores, and vorticity is cancelled at the interaction zone around the (x_2, x_3)-plane by viscous cross-diffusion (§3.2). From the geometry we expect that for smaller θ the threads would slip through the interaction zone before the outer cores come close enough to interact, whereas for larger θ the outer cores touch before the threads meet. Since the threads do not stay in the interaction zone for long, the cancellation of vorticity is not effective for both of these extreme angles. Thus we expect that there is a certain angle at which the inner cores stay in the interaction zone for a relatively long time so that the cancellation is maximum.

4.3. *Effect of viscosity*

The initial condition for Case II (figure 20*a*) is similar to that for Case I which was discussed in detail in §3. As stated in §2, the effective viscosity, or the inverse of the Reynolds number, for Case I is half that for Case II. Thus, we can examine the viscosity dependence of the motion of vortex rings by comparing these two cases.

By comparing figures 4(*a*) and 20(*a*), we recognize that their shapes are very similar at corresponding times. The global motion of the vortex rings, i.e. the translation along the x_3-axis and the rotation toward the (x_2, x_3)-plane seem to be independent of viscosity. The behaviour of the vortex motion in the interaction zone, however, is affected by viscosity. The mechanism of bridging may be the same, but the cancellation of vorticity is less complete for smaller viscosity; that is, the remnant vortices have higher circulation. In table 2 we list the remnant circulation after the first reconnection for Case I, which is reduced by a factor of 4 for comparison with the other cases (§2). We see that the remnant circulation is higher at larger Reynolds numbers. These results on viscosity dependence suggest that the inviscid calculation of vortex motion, e.g. by the vortex filament and vortex-in-cell methods, can simulate the global motion of vortex rings but not vortex reconnections.

4.4. *Second reconnection*

The motion of vortex rings after the first reconnection is also different for different initial inclination angle θ. The second reconnection is more complete (i.e. ratio of circulations in bridges and threads is higher) for $\theta = 15°$ and 30°. Bridges in the

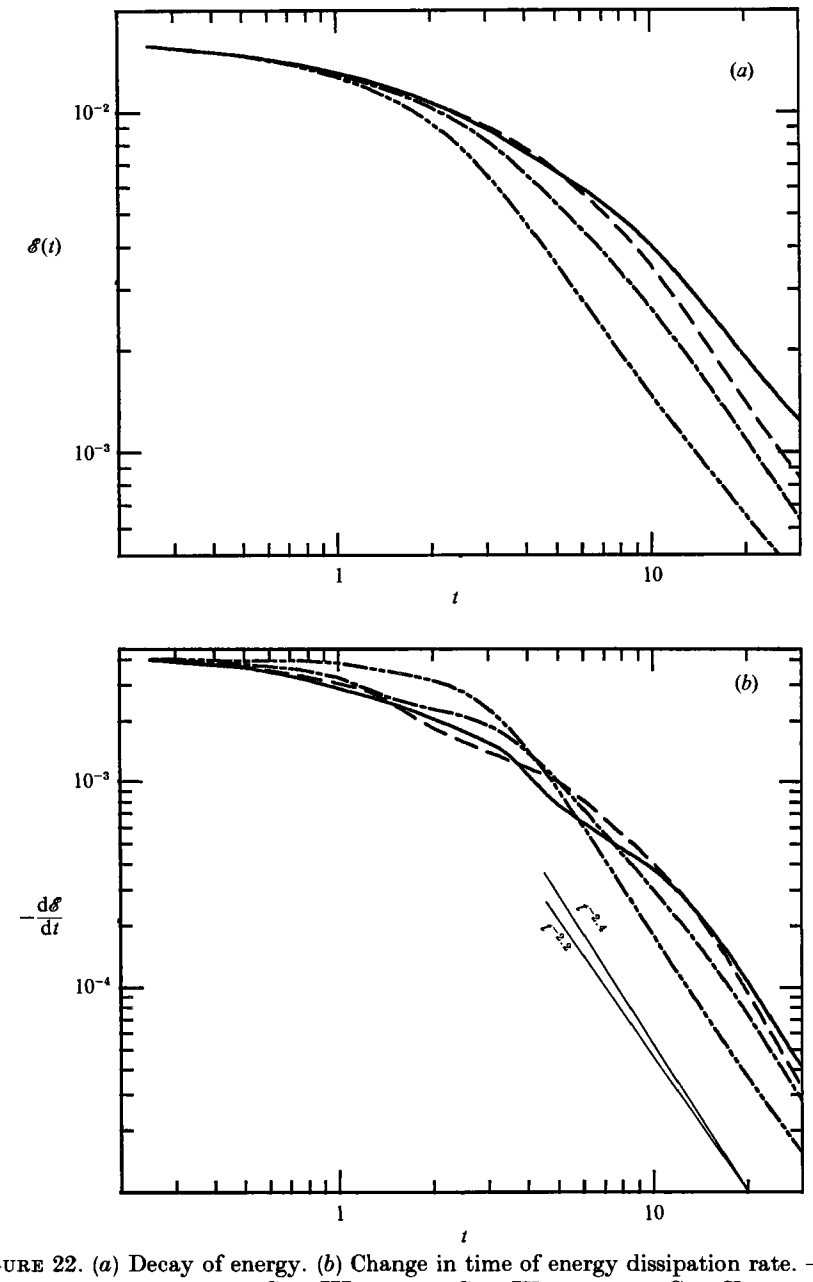

FIGURE 22. (*a*) Decay of energy. (*b*) Change in time of energy dissipation rate. ——, Case II; — — —, Case III; – – – –, Case IV; – – – – – –, Case V.

second reconnection are also created for the other two cases, but for $\theta = 0°$ the process is very slow (compare the final times in figures 20*a–d*), and for $\theta = 45°$ bridges are too weak to appear at the level of iso-surfaces plotted here.

The viscosity dependence of the vortex motion is more prominent at later times. By comparing figure 20(*a*) with figure 4(*a*), we see that viscosity reduces the curvature of vortex rings and also the approaching velocity of the two rings. Remember that Case I can be compared with Case II ($\nu = 0.005$) by the change of

variables given in (2.9) with reduced viscosity $\nu = 0.0025$. We therefore expect that the second reconnection would take place more completely for smaller viscosity.

5. Energy and enstrophy

The kinetic energy of fluid motion decays through dissipation controlled by strain rate and viscosity. Since a reconnection produces complicated fine-scale motions and the viscosity plays the key role in the mechanism, a substantial decay of kinetic energy is associated with a vortex reconnection. Figure 22(*a*) shows the evolution of kinetic energy $\mathscr{E}(t)$, (2.7), for Cases II–V. The energy decays little at first, but it begins to decay appreciably around $t = 2$–3, during the first reconnection. A reconnection produces finer scales – bridges and threads; these contribute to higher dissipation. We can also see that the starting time of the dissipation of energy is earlier for larger angle θ (§4.2).

Figure 22(*b*) shows that the energy dissipation rate $-\mathrm{d}\mathscr{E}/\mathrm{d}t$ (enstrophy $\frac{1}{2}|\boldsymbol{\omega}|^2$ multiplied by 2ν) decreases monotonically in time. The enstrophy production by vortex stretching is not large enough to compensate for the decrease in enstrophy caused by viscous dissipation. We see strange oscillations in the enstrophy decay which are invisible in the decay curves of energy. These oscillations are actually related to those rapid changes of vortex lines during the first reconnection process and the associated vorticity intensification by stretching. Humps are observed at $t \approx 3.5$, 1.2 and 0.9 for Cases II, III and IV, respectively. A hump for Case V is hardly visible. As seen in figure 20(*a*)–(*c*), the first reconnection occurs at these times. Such oscillations are not apparent in the decay curve of enstrophy during the second reconnection because the change is weaker. After these oscillations, the energy-dissipation rate decays algebraically in time as

$$\frac{\mathrm{d}\mathscr{E}}{\mathrm{d}t} \propto -t^{-(p+1)}, \quad p = 1.2\text{–}1.4. \tag{5.1}$$

In particular, the curve for Case V has a wide range of power-law decay, beginning at $t \approx 5$.

The expression for the change over time of energy is obtained by integrating (5.1) as

$$\mathscr{E}(t) = \mathscr{E}_0 + \mathscr{E}_1 t^{-p}, \tag{5.2}$$

where $\mathscr{E}_0$ and $\mathscr{E}_1$ are constants. The power of the decay law is more evident in the energy-dissipation rate than in the energy. This is understood by noting either the existence of a constant term in the energy decay law (5.2) or the localness of the energy-dissipation rate. The regions in which the energy dissipation rate

$$\begin{aligned} \epsilon(\boldsymbol{x}) &= \frac{\nu}{2} \sum_{j,k=1}^{3} \left(\frac{\partial u_j}{\partial x_k} + \frac{\partial u_k}{\partial x_j} \right)^2 \\ &= \nu|\boldsymbol{\omega}|^2 + 2\nu \sum_{j,k=1}^{3} \frac{\partial^2}{\partial x_j \partial x_k} u_j u_k \end{aligned} \tag{5.3}$$

takes large values are more localized in space than the kinetic energy field $|\boldsymbol{u}(\boldsymbol{x})|^2$ so that the total energy-dissipation rate is less affected by periodic boundary conditions. The second term on the right-hand side of (5.3) cancels out after integration with respect to the space coordinates. Therefore the mean values of $\epsilon(\boldsymbol{x})$ and $\nu|\boldsymbol{\omega}|^2$ are

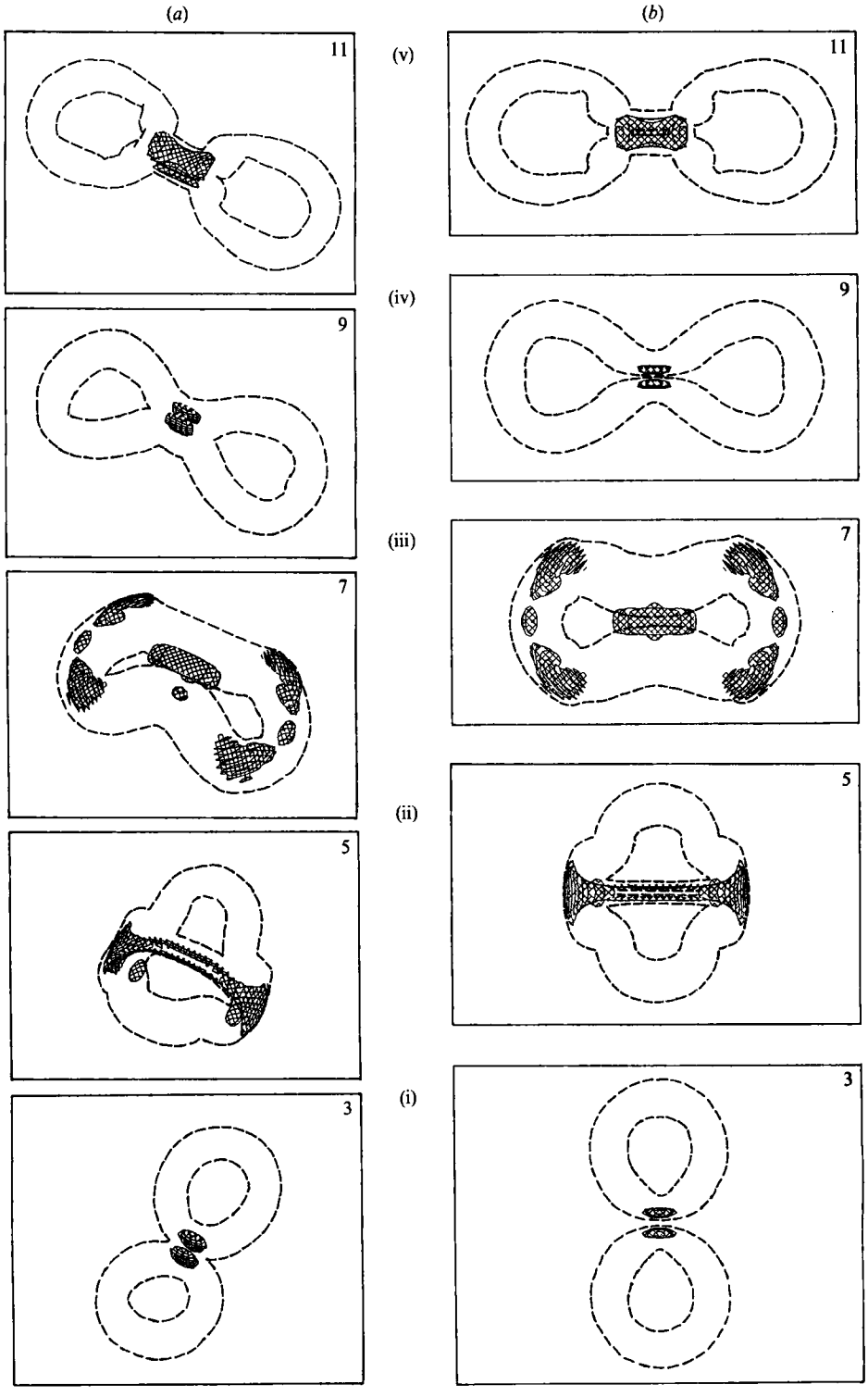

FIGURE 23 (*a*, *b*). For caption see facing page.

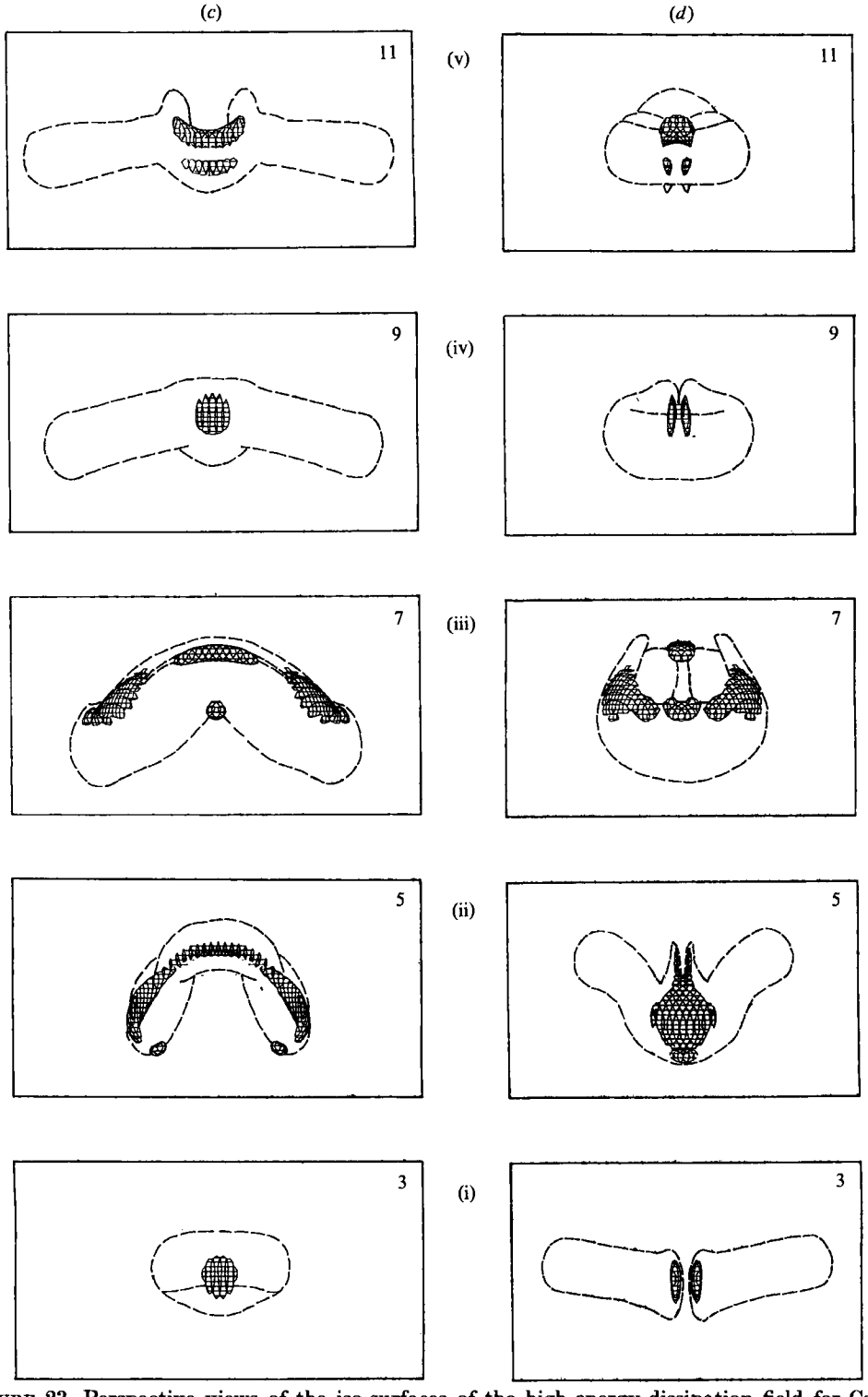

FIGURE 23. Perspective views of the iso-surfaces of the high-energy-dissipation field for Case I which are seen from directions (*a*) (2, 1, 5), (*b*) (0, 0, 1), (*c*) (1, 0, 0) and (*d*) (0, 1, 0). The times and the levels of the iso-surfaces are (i) $t = 3$, 50% of the instantaneous maximum of dissipation rate, (ii) $t = 5$, 30% (iii) $t = 7$, 70%, (iv) $t = 9$, 50% and (v) $t = 11$, 50%. Outlines of the vortex ring (25% levels of $|\omega|_{\max}$) are drawn as broken lines for reference.

exactly equal. Their local values, however, differ appreciably owing to the second term which is typically of the same order of magnitude as the first.

Figure 23 shows four different views of the high-energy-dissipation regions for Case I. The regions where $\epsilon(\boldsymbol{x})$ takes values larger than a specific fraction of the maximum are drawn. Broken lines denote the vortex core at the 25% level of $|\boldsymbol{\omega}|_{\max}$ (see figure 4). We see that $\epsilon(\boldsymbol{x})$ is much more localized than $|\boldsymbol{\omega}(\boldsymbol{x})|$ in the interacting dipole before the reconnections, and in bridges and threads (or legs) after the reconnections. This indicates that the second term in (5.3) is of comparable order of magnitude as the first. While the enstrophy has a large organized structure, i.e. it extends more in space and its shape is preserved for relatively long times, the energy dissipation field is localized in space and changes rapidly. The spatial distribution of high-energy-dissipation regions will be discussed further in §7 in relation to the domains of large-helicity density.

The power law (5.1) or (5.2) is similar to the energy decay law of fully developed turbulence. The power law of energy decay (5.2) in turbulence has been observed in many laboratory experiments (Uberoi 1963; Comte-Bellot & Corrsin 1966; Ling & Wan 1972; Ginevskii, Kolesnikov & Ukhanova 1979). The power p varies in the range $1.0 \lesssim p \lesssim 1.4$ from experiment to experiment. The power law of energy decay in turbulence has also been derived theoretically and shown to be different for different kinds of turbulence. It depends especially on the characteristics of large-scale motions (Kolmogorov 1941; Saffman 1967; Tatsumi, Kida & Mizushima 1978; Kida 1981; Lesieur & Schertzer 1978). A recent numerical simulation by Kida & Murakami (1988) also demonstrated the power law of energy decay and its dependence on the large-scale motions. Our velocity field is not in a state of a fully developed turbulence as far as the large-scale motions are concerned. However, it is likely that the small-scale motions may be in a turbulent state especially in the bridges and threads. Since energy dissipation is confined to these small scales and the dissipation from these regions gives the dominant contribution to the total dissipation, it is reasonable to expect that the energy-dissipation rate obeys the same decay law as turbulence.

The band-averaged three-dimensional energy spectrum function $E(k)$, which is the kinetic energy of the Fourier components of wavenumbers between $k-\frac{1}{2}$ and $k+\frac{1}{2}$, is plotted at several times for Case IV in figure 24; (a) and (b) are linear-log and log-log plots, respectively. The peak wavenumber 4 at $t = 0$ corresponds to the core-diameter $2a$ (≈ 4 mesh lengths), while the hump at wavenumber 10 corresponds to the ring diameter $2D$ (≈ 10 mesh lengths). The energy is transferred rapidly to larger wavenumbers at early times ($t \lesssim 3$). This is a manifestation of the small-scale components being excited by stretching, flattening and reconnection of vortex rings. At later stages of evolution, the viscosity has an effect so that the energy spectrum decays over the entire wavenumber range. We note in passsing that the rapid decrease of the energy spectrum at large wavenumbrers is a good measure of the accuracy of the numerical simulation.

The enstrophy-production rate by vortex stretching is expressed by

$$P = \boldsymbol{\omega} \cdot \boldsymbol{S} \cdot \boldsymbol{\omega}. \tag{5.4}$$

Figure 25 shows four perspective views of iso-surfaces of the enstrophy-production rate for Case I at the same times as in figure 23 for the energy-dissipation rate. The positive enstrophy-production regions are shaded darker. We can see that the enstrophy-production rate is high in the interacting dipole before the reconnections, and in the bridges and threads after the reconnections. In other words, the vorticity

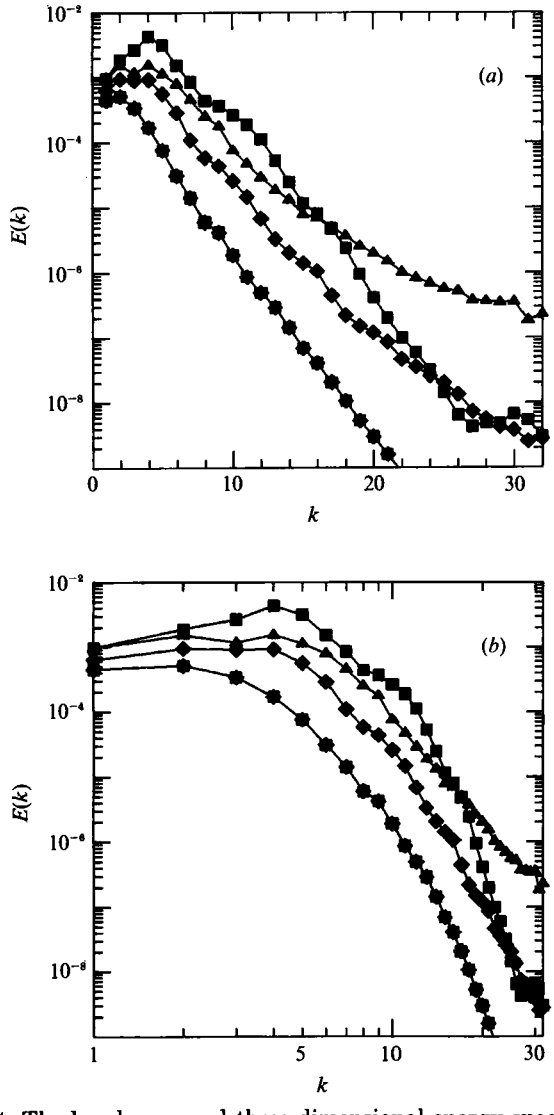

FIGURE 24. The band-averaged three-dimensional energy spectrum for Case IV: (*a*) linear log-scale, (*b*) log–log scale: ■, $t = 0$; ▲, 3; ◆, 6; ✱, 15.

lines are stretched in these regions. There are similarities and differences in shape between the high-enstrophy-production and high-energy-dissipation regions (cf. figures 23 and 25). These regions are similar before the reconnections (e.g. $t = 3$ and 9) but not after (e.g. $t = 5$, 7 and 11). In the latter stages the peaks of the energy dissipation rate are between those of enstrophy-production rate (cf. figure 18 in MH). This indicates that these two quantities behave quite independently of each other. Incidentally, it has been suggested that high energy dissipation is expected in regions of high enstrophy production, where the small-scale motions are excited by vortex stretching. The present results, however, suggest that this correspondence does not always hold.

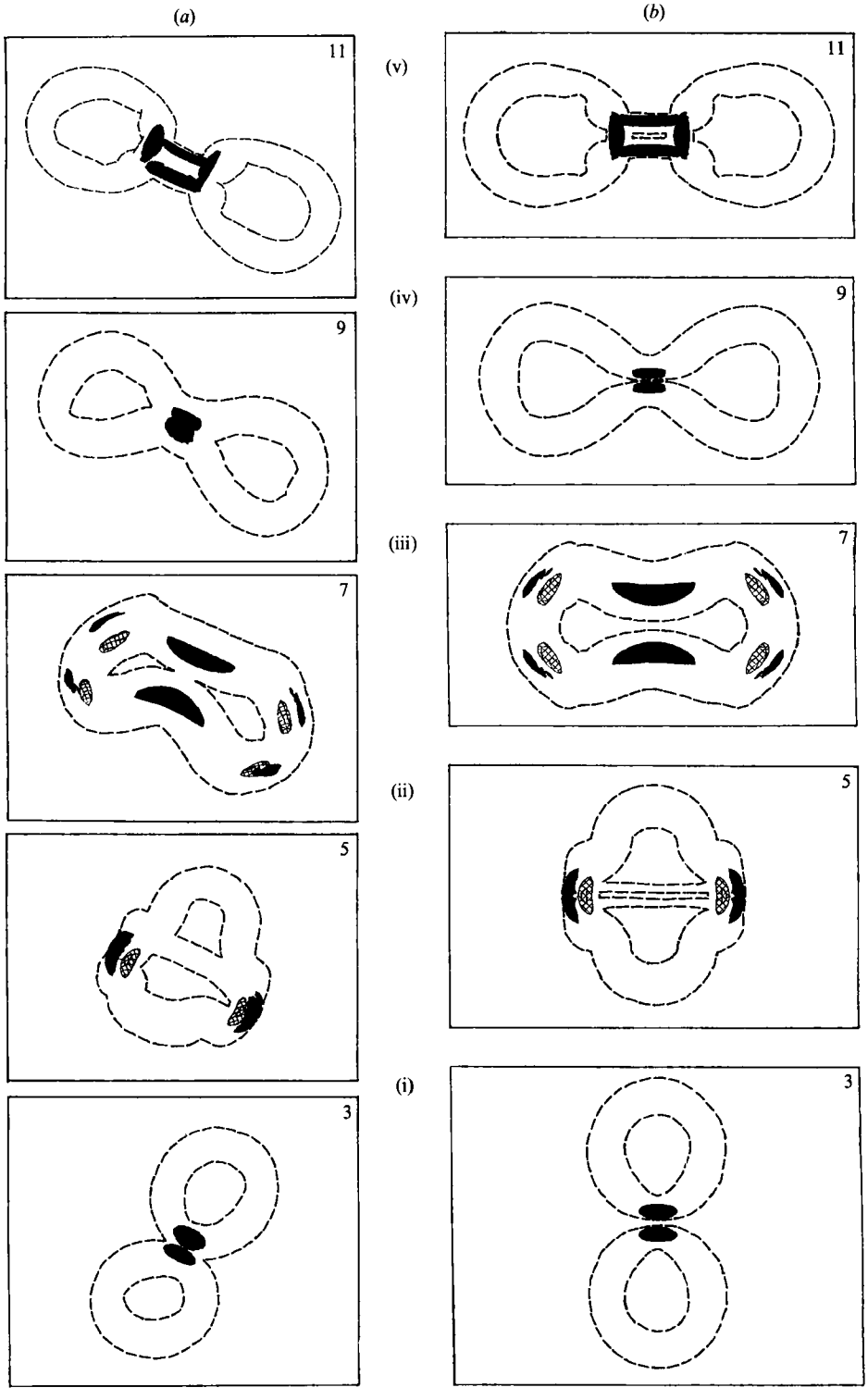

FIGURE 25(*a*, *b*). For caption see facing page.

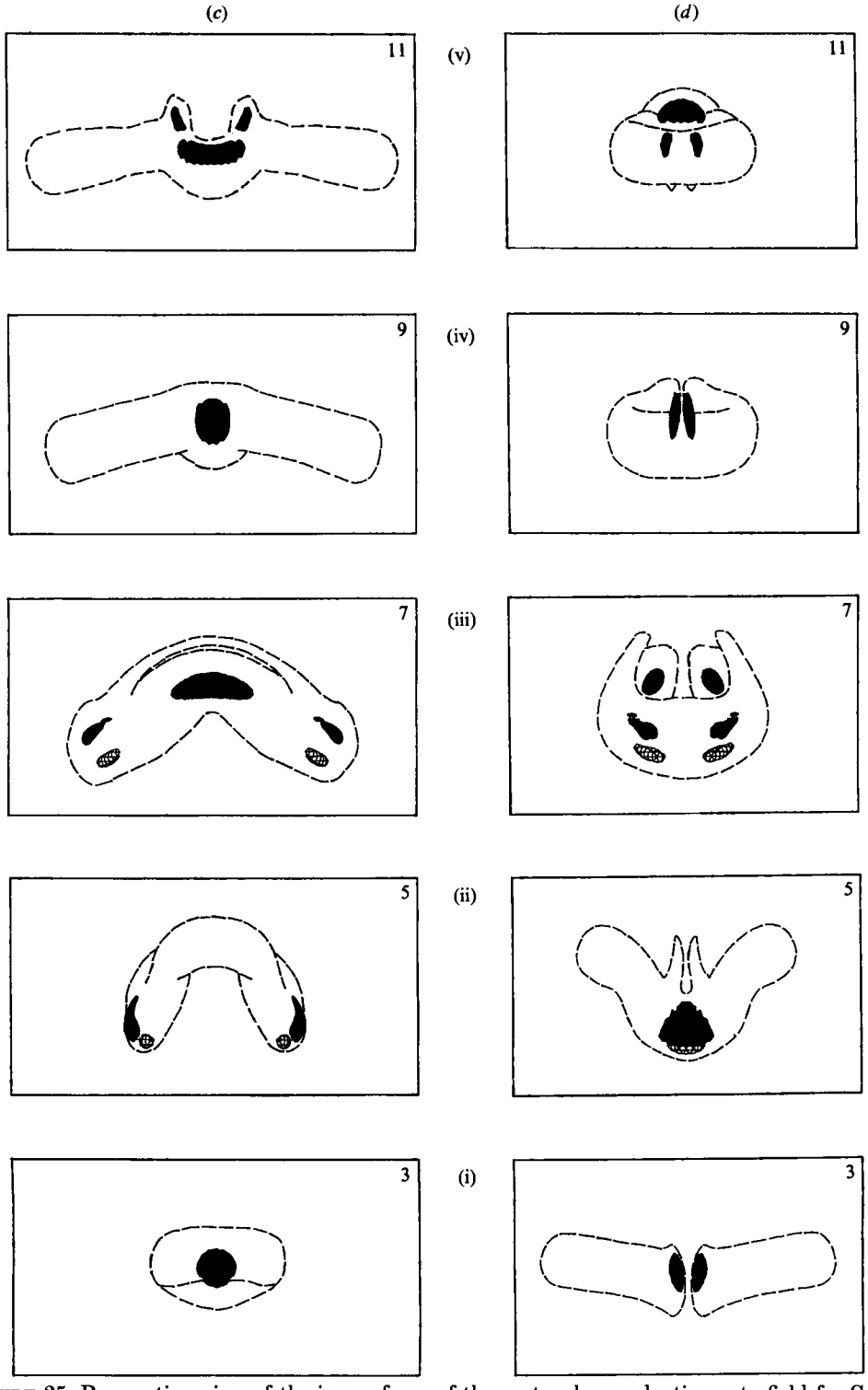

FIGURE 25. Perspective view of the iso-surfaces of the enstrophy-production-rate field for Case I which are seen from directions (*a*) (2, 1, 5), (*b*) (0, 0, 1), (*c*) (1, 0, 0) and (*d*) (0, 1, 0). The times and the levels of the iso-surfaces are (i) $t = 3$, 30% of the instantaneous maximum of the production rate, (ii) $t = 5$, 30%, (iii) $t = 7$, 50%, (iv) $t = 9$, 30% and (v) $t = 11$, 30%. Positive regions are shaded darker. Outlines of the vortex ring (25% of $|\omega|_{\max}$) are drawn as broken lines for reference.

6. Passive scalar transport

Smoke or dye have been used frequently in laboratory experiments for flow visualization. They are advected by fluid motion while spreading in space by molecular diffusion, but they hardly alter the fluid motion. If we neglect their influence on fluid motion, the motion of a floating material is governed by

$$\frac{\partial}{\partial t}S+(\boldsymbol{u}\cdot\boldsymbol{\nabla})S=\kappa\nabla^2 S, \tag{6.1}$$

where κ is the diffusivity of the material S.

The advection and diffusion terms are the same as in (2.2), but here there is no counterpart of the first term in the right-hand side of (2.2) which represents vortex stretching. That is, a passive material is advected by fluid motion and diffused by molecular diffusivity, whereas vorticity not only undergoes advection and diffusion but is also influenced by stretching of a fluid element. The lack of the stretching term in the scalar equation results in a difference in the time evolution of the vorticity and passive scalar fields in three-dimensional flows, even at unity Schmidt number ($\nu = \kappa$). Vorticity is intensified by stretching of a fluid element, whereas the density of a passive scalar is decreased. This reminds us of the repeated warnings against trusting flow visualization in turbulent flows for studying vortex dynamics and coherent structures (Hussain 1983, 1986).

If the advection term is large enough that the stretching term may be neglected, the motion of a scalar is the same as that of vorticity. In regions where the stretching effect is dominant, on the other hand, their behaviour should be different. In the following, we will describe the similarities and differences in the time evolution of a scalar and vorticity.

The time development of a passive scalar is simulated numerically for Case IV. Initially the scalar quantity has the same distribution as the vorticity magnitude (2.5). Both the viscosity ν and the diffusivity κ are set to be 0.005, i.e. the Schmidt number is one.

Four perspective views of the iso-surfaces of the vorticity norm and the concentration of the passive scalar are drawn in figure 26 at $t = 0$, 1, 1.5, 2, 3, 5, 10, 15. They are seen from the (2, 1, 5)-, (0, 0, 1)-, (1, 0, 0)- and (0, −1, 0)-directions, respectively. At first sight, we recognize that the two quantities change similarly but not identically. During the first reconnection, the distributions of the vorticity norm and the scalar are similar except that the scalar quantity diffuses much more than the vorticity field (see figure 26*a–d* (ii–v) and their iso-surface levels). The similarity, however, seems to be rather accidental. Where a cancellation of vorticity occurs, a fluid element is stretched very much so that the scalar is also depleted. After the first reconnection, the difference between the two distributions is significant (see figure 26*a–d* (iv–vi)). The two round portions at both ends of the ring are stretched by their own induction velocity so that vorticity is intensified there but the scalar quantity is diluted. This is the reason why we observe a relatively higher density of the scalar at the central region at $t = 5$ and 10. Then, at a later stage of the second reconnection, the two legs are stretched much faster than the ring portions. As a result, the scalar density in the legs is reduced and the density in the rings becomes relatively high. Meanwhile (at $t = 15$), we observe two holes at the positions of the vortex rings. Furthermore, at very large times ($t = 21$), we see two separate blobs of high density of scalar as visualized in experiments (figure 6*c* in Oshima & Asaka 1977).

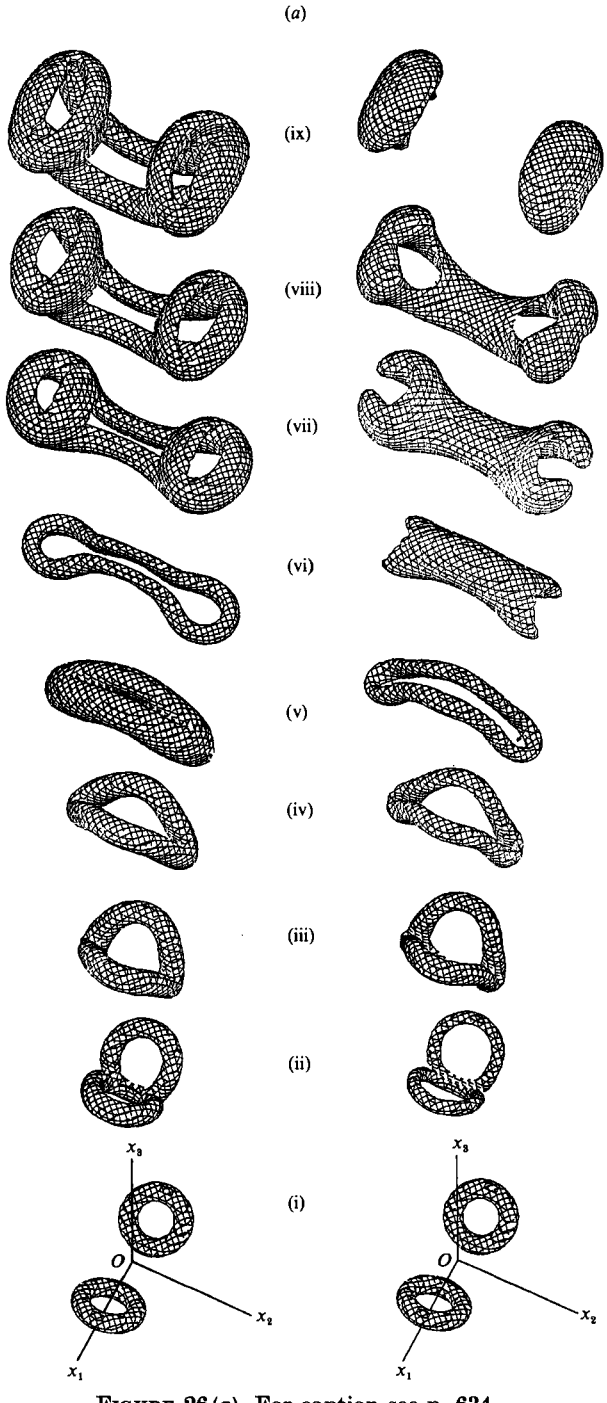

FIGURE 26(*a*). For caption see p. 634.

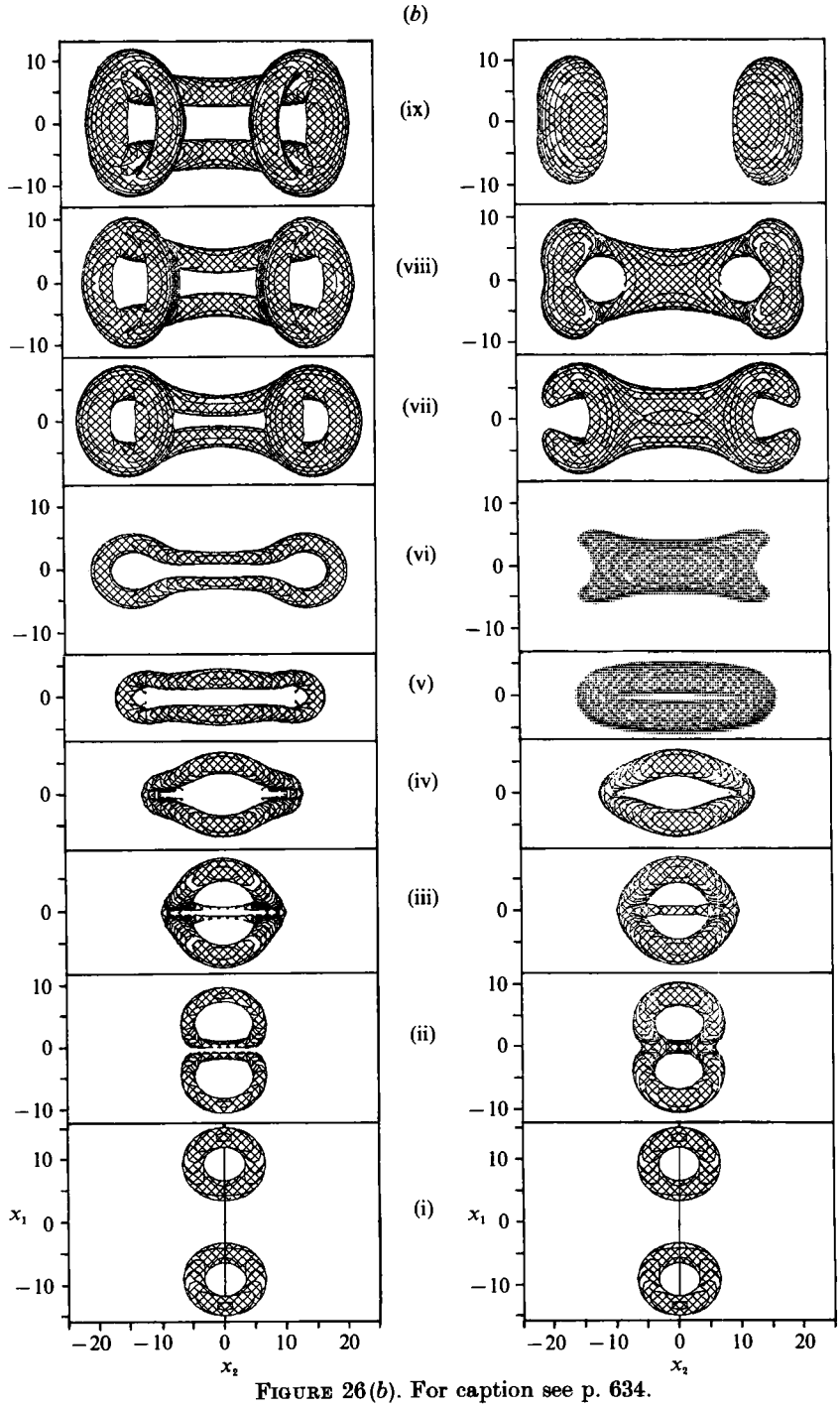

FIGURE 26(*b*). For caption see p. 634.

Cross-sections of vorticity components (left) and the scalar density (right) on the (x_1, x_3)- and the (x_2, x_3)-planes are drawn at three representative times in figures 27(*a*) and 27(*b*), respectively. At $t = 2$, just after the first reconnection, the scalar has already been diffused much more than vorticity (compare their contour levels). At

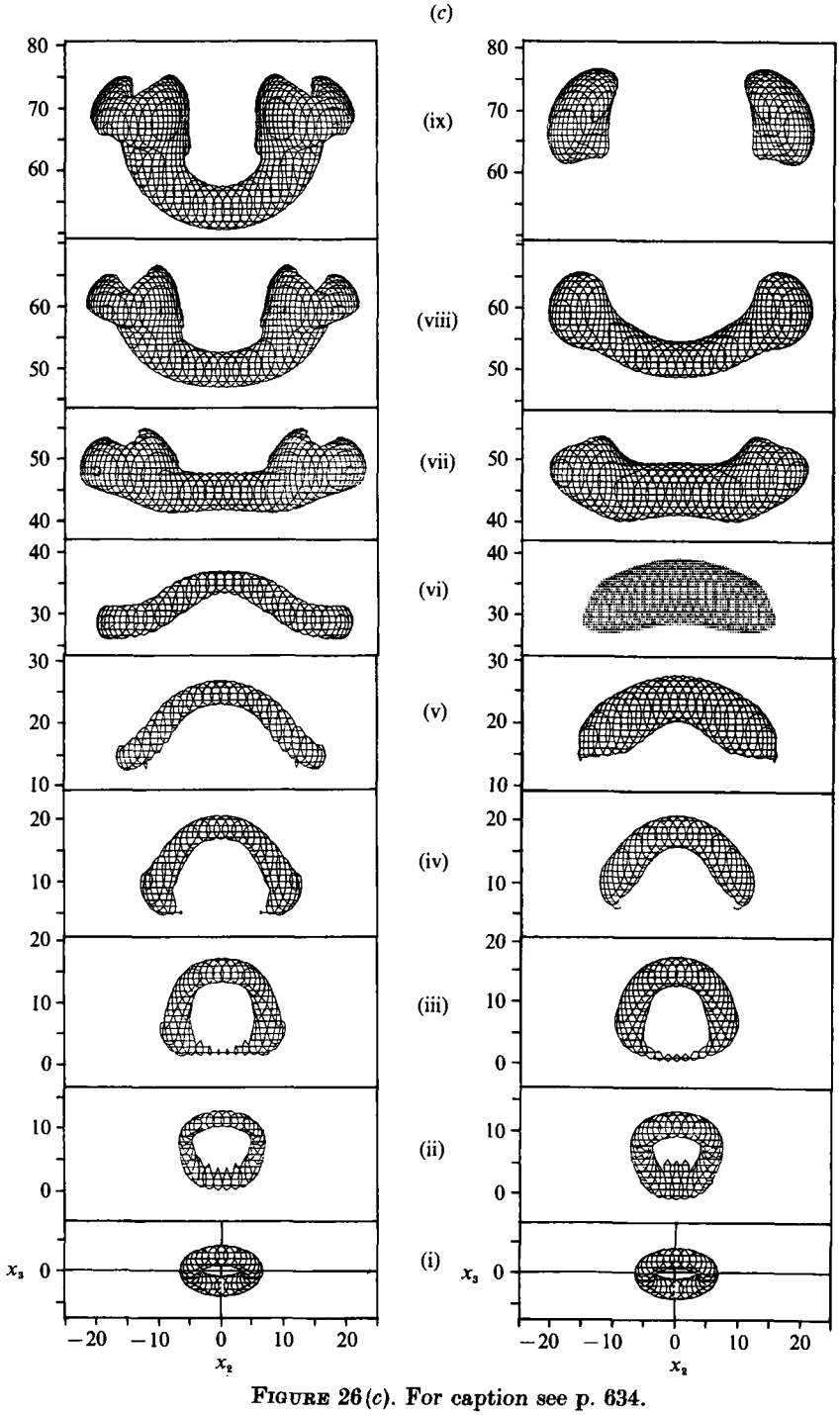

FIGURE 26(*c*). For caption see p. 634.

higher levels (shaded regions), the two quantities still look similar. However, at $t = 5$, after the merged vortex has undergone stretching and shrinking motions, the shapes of the two quantities are completely different (see figure 26(vi)). We cannot seen any resemblance between the two in the cross-section in the (x_2, x_3)-plane. The

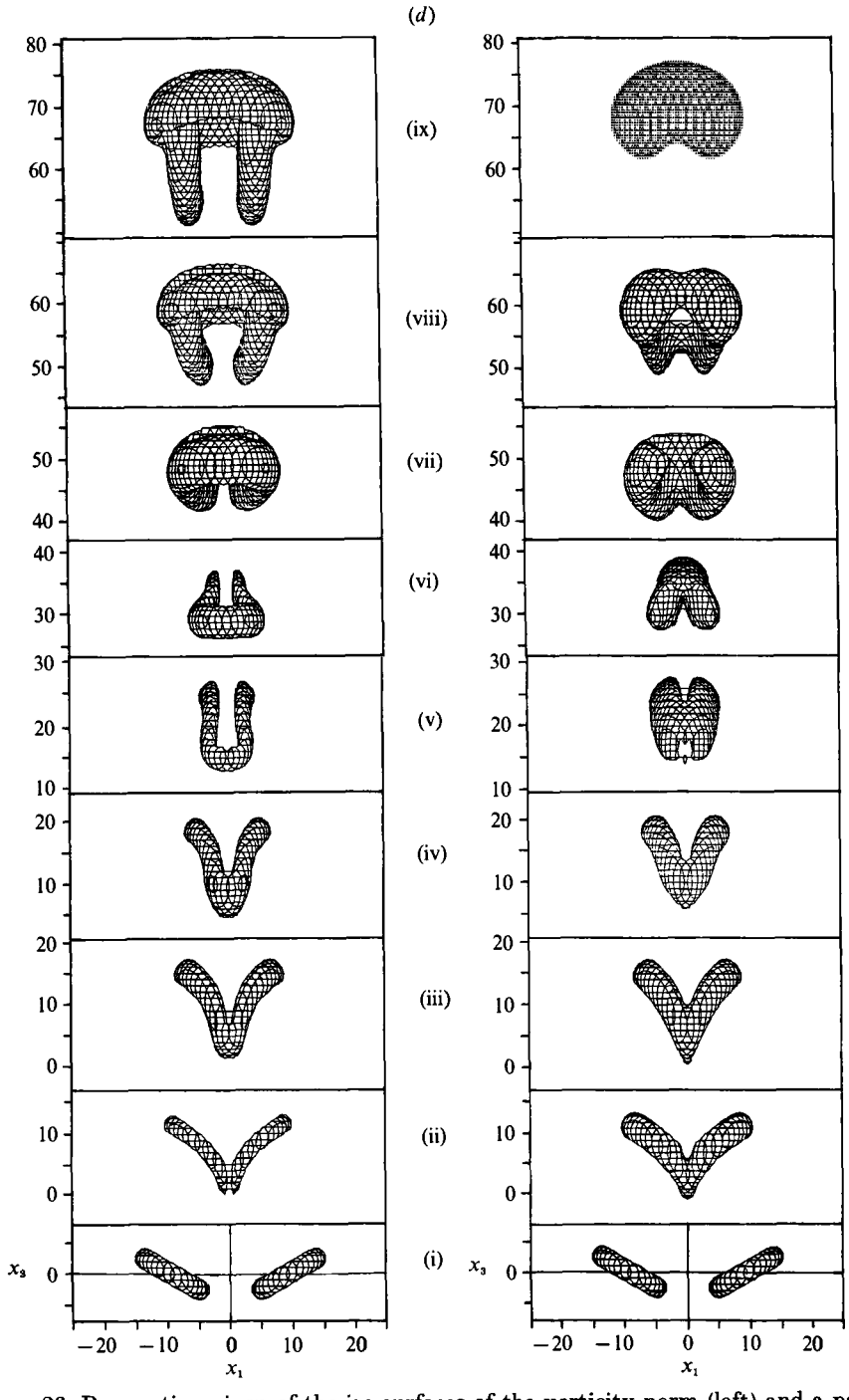

FIGURE 26. Perspective views of the iso-surfaces of the vorticity norm (left) and a passive scalar (right) for Case IV. They are seen from directions (*a*) (2, 1, 5), (*b*) (0, 0, 1), (c) (1, 0, 0) and (*d*) (0, −1, 0) (i) $t = 0$, (ii) 1, (iii) 1.5, (iv) 2, (v) 3, (vi) 5, (vii) 10, (viii) 15 and (ix) 21. The isosurface levels of the vorticity norm are 40% at $t = 3$, 45% at $t = 21$ and 50% at other times, and those of the scalar are 40% at $t = 3$, 60% at $t = 15$ and 21, and 50% at other times.

contours of the scalar quantity in the (x_1, x_3)-plane have two peaks similar to the vorticity norm only at the highest level (80%) at $t = 5$. Later, at $t = 15$, well after the second reconnection, the similarity in shape of the two quantities improves. The cross-sections in the (x_2, x_3)-plane resemble each other slightly at higher levels, but not enough to merit discussion of the detailed structure. Note in passing, the especially impressive long tail in the scalar contour (figure 27*a*, *b*(iii)).

Thus, we conclude that although the final appearance of the scalar and vorticity norm is similar, this is accidental because of two opposite effects in the two successive reconnection processes. It is not guaranteed that the change over time of a scalar quantity will represent the vorticity dynamics faithfully (see also MH). This conclusion was drawn from a simulation of a flow with unity Schmidt number and is expected to hold for other Schmidt numbers.

7. Helicity dynamics

7.1. *Helicity and helicity density*

The inner product of velocity and vorticity,

$$h_u = \boldsymbol{u}\cdot\boldsymbol{\omega} \tag{7.1}$$

is called the helicity density. It is a pseudo-scalar and represents the twisted structure of the velocity field. The equation for the time development of helicity density can be derived from (2.1)–(2.4) as

$$\frac{\partial}{\partial t}h_u + \nabla\cdot(\boldsymbol{u}h_u) = -\nabla\cdot\left(\boldsymbol{\omega}\frac{p}{\rho}\right) + \tfrac{1}{2}\nabla\cdot(\boldsymbol{\omega}\boldsymbol{u}\cdot\boldsymbol{u}) + \nu(\nabla^2 h_u - 2\nabla\nabla : \boldsymbol{u}\boldsymbol{\omega} - 2h_\omega), \tag{7.2}$$

where

$$h_\omega = \boldsymbol{\omega}\cdot\boldsymbol{\chi} \tag{7.3}$$

is the super-helicity density and

$$\boldsymbol{\chi} = \nabla\times\boldsymbol{\omega} \tag{7.4}$$

is the di-vorticity. (In a two-dimensional flow the di-vorticity plays an important role in the formation of vorticity gradient (Kida 1985).)

By integrating (7.2) over a periodic domain, we obtain

$$\frac{\mathrm{d}}{\mathrm{d}t}H_u = -2\nu H_\omega, \tag{7.5}$$

where

$$H_u = \int h_u \,\mathrm{d}\boldsymbol{x} \tag{7.6}$$

is the helicity and

$$H_\omega = \int h_\omega \,\mathrm{d}\boldsymbol{x} \tag{7.7}$$

is the super-helicity.

The helicity density changes locally in space and time through advection, diffusion and potential-force-like terms (see (7.2)). These nonlinear effects for the time variation of helicity H_u cancel out after spatial integration. Equation (7.5) implies that the helicity is a constant of motion in inviscid flow. In the inviscid case, an integration of helicity density over any domain surrounded by a vorticity surface is conserved. It is, however, not known whether H_u is conserved in the inviscid limit. There is no guarantee that H_ω would remain finite in this limit.

The helicity density represents the torsional structure of the velocity field. As illustrated in figure 28, if the streamlines are twisted like a right (left)-handed screw,

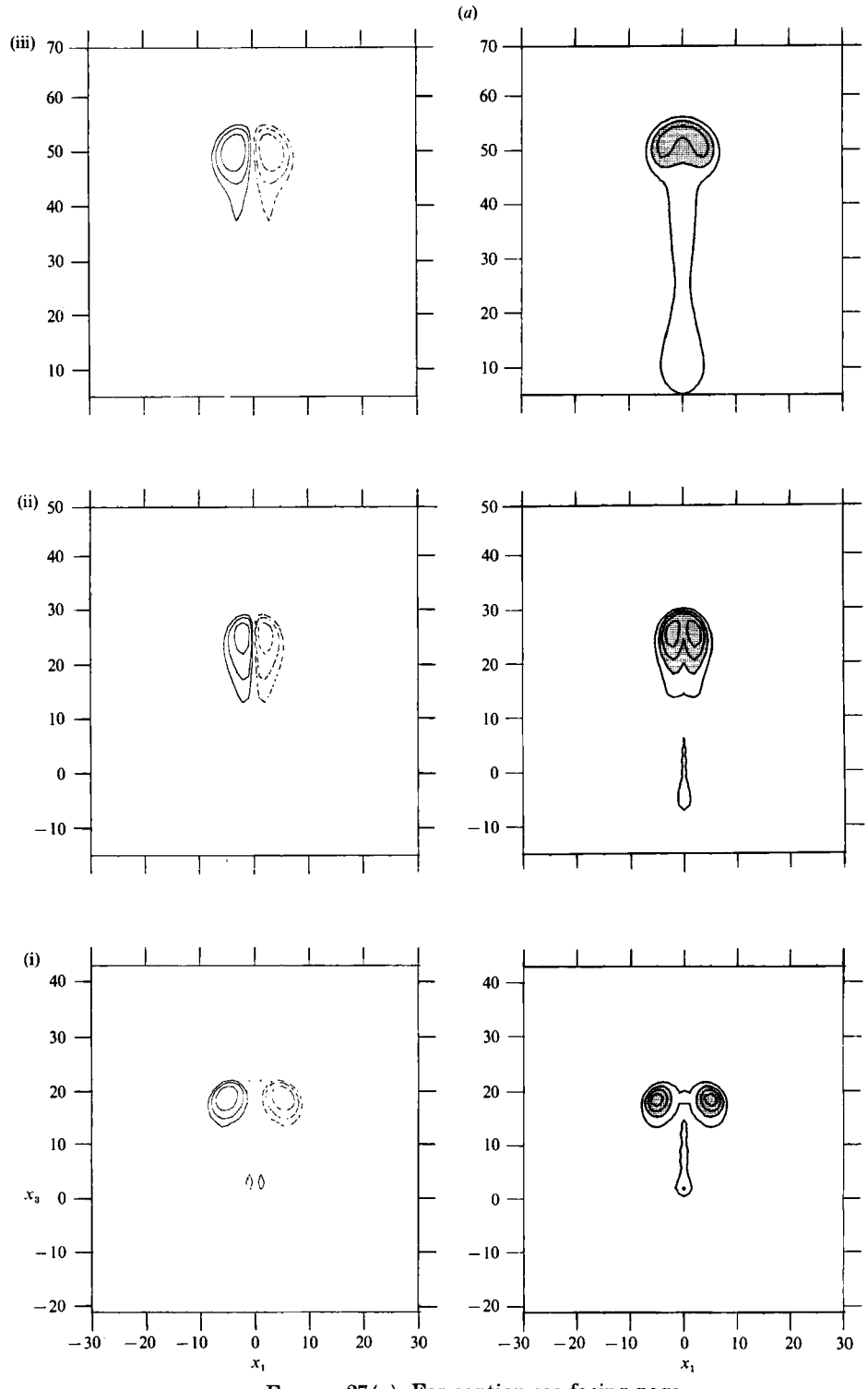

FIGURE 27 (*a*). For caption see facing page.

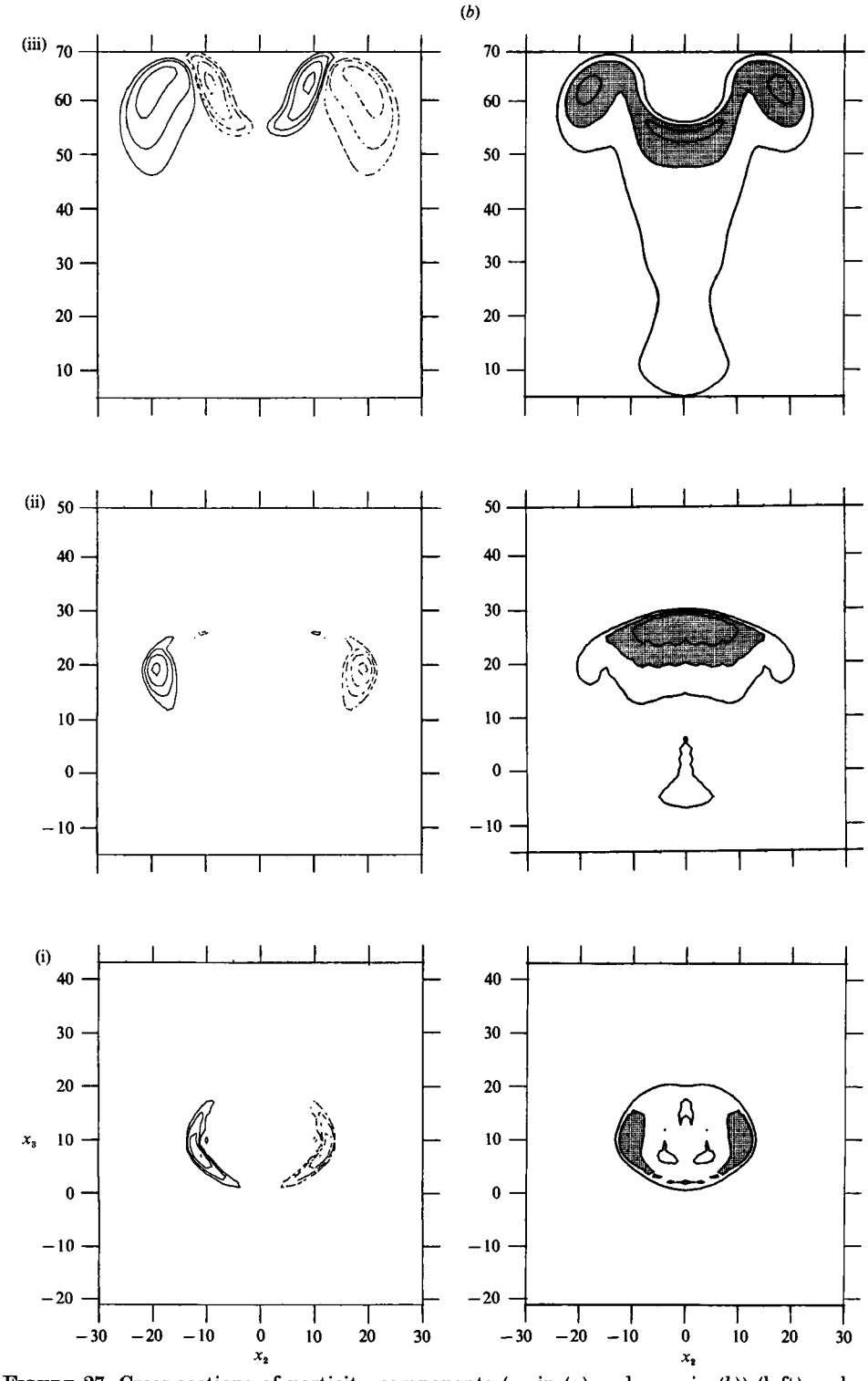

FIGURE 27. Cross-sections of vorticity components (ω_1 in (a) and $-\omega_2$ in (b)) (left) and a passive scalar (right) on (a) the (x_1, x_3)-plane and (b) the (x_2, x_3)-plane at (i) $t = 2$, (ii) 5 and (iii) 15 for Case IV. The levels of vorticity contours are ± 10, ± 20, ± 40 and $\pm 80\,\%$ of $|\omega|_{\max}$. Solid and broken lines represent positive and negative values, respectively. The contour levels of the scalar are 20, 40, 60 and 80% of the maximum. The regions of scalar density higher than 40% are shaded.

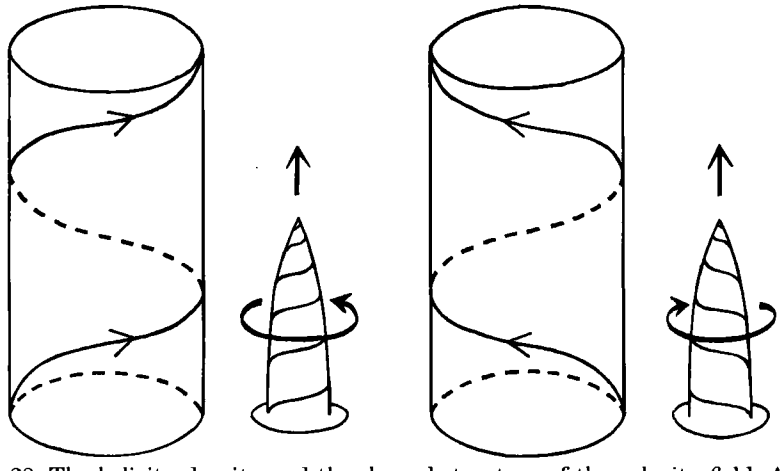

FIGURE 28. The helicity density and the skewed structure of the velocity field. A positive (negative) helicity density represents streamlines twisted like a right (left)-handed screw.

it gives a positive (negative) helicity density. This is true for a pure helicoidal motion, i.e. a solid rotation plus a constant axial flow and for a small deviation from it, but not always for a general velocity field. Likewise, the super-helicity density represents the torsional structure of the vorticity field.

The helicities, H_u and H_ω, have also topological meanings. They are related to the total amount of entanglement of the vorticity and di-vorticity lines, respectively (Moffatt 1969). The constancy of helicity in an inviscid flow is a manifestation of any reconnection of vorticity lines being prohibited in the inviscid case. Note, however, that the inverse is not always true. As in the case of a collision of two vortex rings, the helicity does not always change even if a vortex reconnection causes a change of topology of the vortex lines.

In a viscous case, the helicity changes in time according to (7.5). It may increase or decrease according as the super-helicity is negative or positive. Notice here the minus sign on the right-hand side of (7.5). It means that the skewed structure of the vorticity field may work to generate a skewed structure of opposite sense to the velocity field.

7.2. *Helicity density in a moving frame*

The helicities and helicity densities introduced in the preceding section are closely related to the topological structure of the flow field. The appearance of the velocity field is different in a frame moving with a different velocity $\boldsymbol{U}$, i.e. it is not Galilean invariant (e.g. Levich 1987). Therefore, there must be an appropriate frame in which the relation between the helicity density and the skewed structure of the velocity field can be recognized most clearly.

One of the most reasonable coordinate systems may be the one in which the change over time of the spatial pattern of the velocity field is minimized. There seems to be no definite way to specify it because an actual flow field does more or less change in time. Here we propose a practical method to find such a moving system that minimizes the integral of the square of helicity density.

Consider an integral of the square of helicity density in a coordinate system moving with velocity $\boldsymbol{U}$,

$$I = \int [\boldsymbol{\omega}(\boldsymbol{x}) \cdot (\boldsymbol{u}(\boldsymbol{x}) - \boldsymbol{U})]^2 \, \mathrm{d}\boldsymbol{x}, \tag{7.8}$$

where the integration is taken over a whole periodic box. The velocity $\boldsymbol{U}$ which

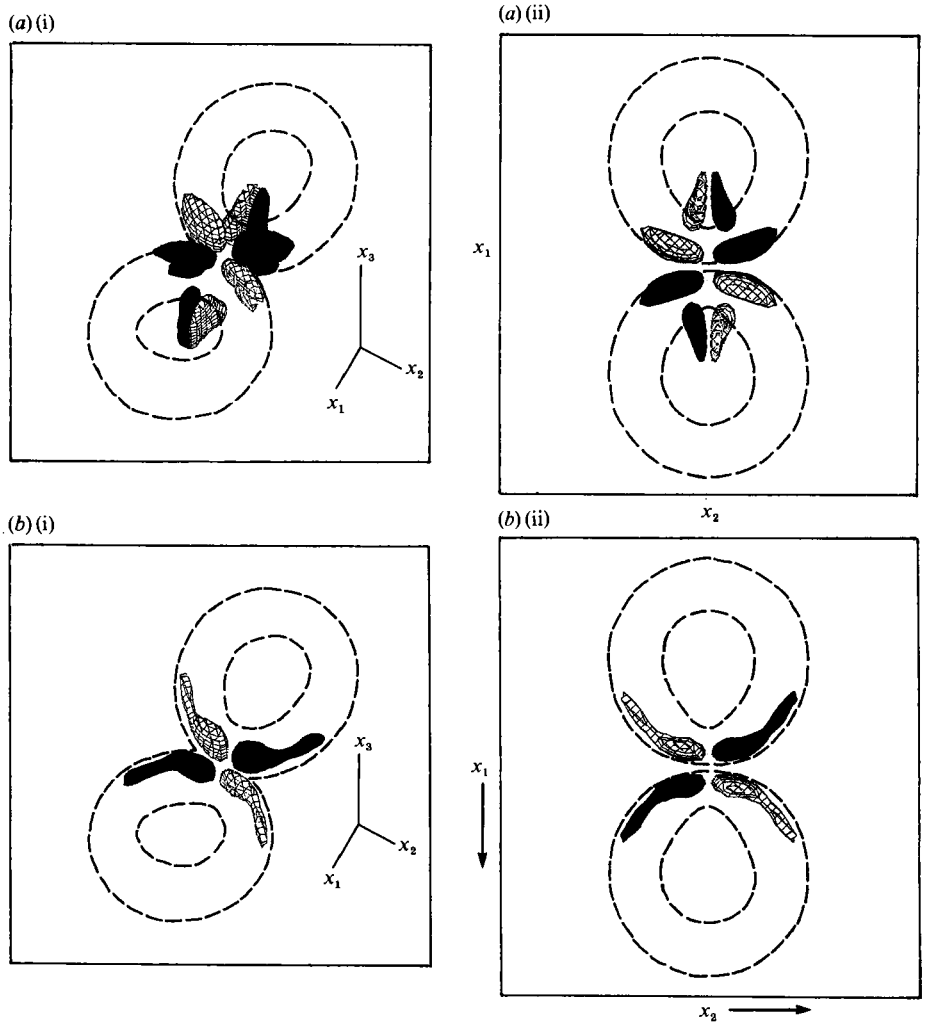

FIGURE 29. Perspective views of the iso-surfaces of (*a*) the helicity and (*b*) super-helicity densities which are seen from directions (i) (2, 1, 5) and (ii) (0, 0, 1) at $t = 3$ for Case I. Surface levels are $\pm 50\%$ of the maximum of the helicity magnitude for both helicities. Blacked and hatched regions represent positive and negative values, respectively. The helicity density is calculated in a moving frame ($U_3 = 0.673$) in which an integral of the square of the helicity density is minimized.

minimizes the integral I is found by putting the derivative of I with respect to each component of $\boldsymbol{U}$ equal to zero,

$$\frac{\partial I}{\partial U_i} = \sum_{j=1}^{3} \int \omega_j(\boldsymbol{x})\,(u_j(\boldsymbol{x}) - U_j)\,\omega_i(\boldsymbol{x})\,\mathrm{d}\boldsymbol{x} = 0, \quad i = 1, 2, 3. \tag{7.9}$$

Thus, the velocity $\boldsymbol{U}$ satisfies the following simultaneous linear algebraic equations:

$$\sum_{j=1}^{3} A_{ij}\,U_j = B_i, \tag{7.10}$$

where

$$A_{ij} = \int \omega_i(\boldsymbol{x})\,\omega_j(\boldsymbol{x})\,\mathrm{d}\boldsymbol{x} \tag{7.11}$$

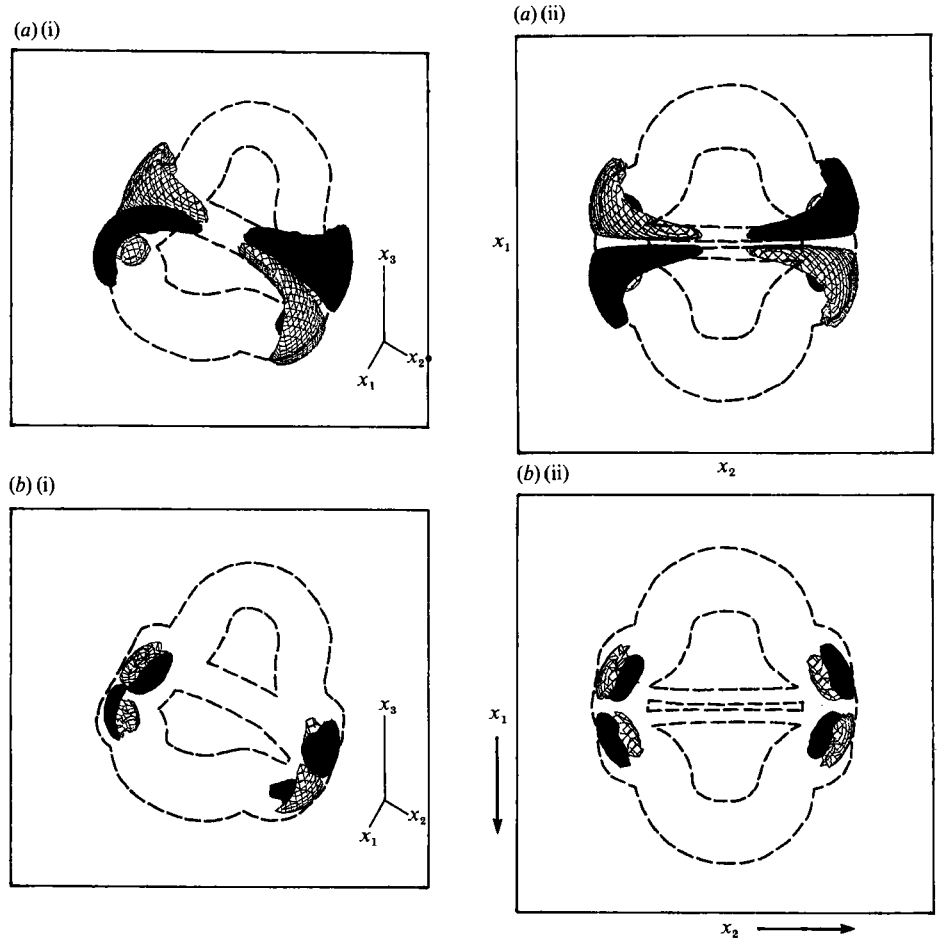

FIGURE 30. The same as figure 29 at $t = 5$, $U_3 = 0.623$.

and
$$B_i = \int h_u(\boldsymbol{x})\,\omega_i(\boldsymbol{x})\,\mathrm{d}\boldsymbol{x}. \tag{7.12}$$

In the present case the flow is symmetric with respect to the (x_1, x_3)- and the (x_2, x_3)- planes so that A_{ij} is a diagonal tensor and B_i contains the x_3-components only; that is,

$$A_{ij} = \delta_{ij} \int \omega_i(\boldsymbol{x})^2\,\mathrm{d}\boldsymbol{x} \tag{7.13}$$

and
$$B_i = \delta_{i3} \int h_u(\boldsymbol{x})\,\omega_3(\boldsymbol{x})\,\mathrm{d}\boldsymbol{x}. \tag{7.14}$$

Thus, the velocity $\boldsymbol{U}$ is given by

$$\boldsymbol{U} = \left(0, 0, \frac{\int h_u(\boldsymbol{x})\,\omega_3(\boldsymbol{x})\,\mathrm{d}\boldsymbol{x}}{\int \omega_3(\boldsymbol{x})^2\,\mathrm{d}\boldsymbol{x}}\right). \tag{7.15}$$

Figures 29 and 30 respectively show the iso-surfaces of the helicity and super-helicity densities at $t = 3$ and 5 — two typical time instants during the first

reconnection for Case I. The helicity density is calculated in a frame moving with velocity $\boldsymbol{U}$ given by (7.15). The levels of the iso-surfaces are $\pm 50\%$ of the instantaneous maximum of helicity density magnitude. The positive parts are shaded darker. The helicity density takes negative values in a quadrant $x_1, x_2 > 0$ (see figures 29 and 30*a*). This suggests that the streamlines are twisted as a left-handed screw in this quadrant. The helicity density is antisymmetric with respect to both the (x_1, x_3)- and the (x_2, x_3)-planes, so the senses of twist of the streamlines are opposite in adjacent quadrants. In this symmetric configuration of the flow, therefore, the helicity is always zero though the helicity density takes non-zero values locally. The four islands along the (x_1, x_3)-plane at $t = 3$ extended out of the main vortex tube. This reflects the non-local nature of the velocity field. As seen in figure 30(*a*), the helicity density is large in threads as well as around bridges at $t = 5$. The sign of helicity density in the threads is easily understood by considering the direction of rotation of the threads and the expanding flow along the threads.

The super-helicity density has a similar structure to the helicity density but more localized in space. At $t = 3$, it takes negative values in the first and the third quadrants $x_1 x_2 > 0$, and positive in the second and the fourth quadrants $x_1 x_2 < 0$. This suggests that the vorticity lines are twisted as left-handed and right-handed screws in the respective quadrants. These senses of twist are consistent with those represented schematically in figure 8. At a later time ($t = 5$), the super-helicity density exhibits a more complicated structure. It is seen in figure 30(b) that there are regions of large positive and negative super-helicity density in each quadrant in the bridges so that the flow field may have a more complicated structure there.

Now let us make a comment on the helicity density and a lifetime of structures. The helicity density has attracted much attention with respect to a nonlinear term $(\boldsymbol{\omega} \times \boldsymbol{u})$ of the Navier–Stokes equation (2.1), which causes energy to small-scale motions. It is argued that this term may be small in regions where helicity density is large, for $\boldsymbol{\omega}$ and $\boldsymbol{u}$ are almost parallel in such regions and thus $\boldsymbol{\omega} \times \boldsymbol{u}$ is small. Furthermore, if the nonlinear interaction term is small, the generation of small scales is inhibited and therefore viscous dissipation is also less. Then, we can expect a long-lived structure of the flow which may describe the so-called coherent structure.

This argument, however, seems superficial. First, the magnitudes of $\boldsymbol{\omega}$ and $\boldsymbol{u}$ are not taken into account. We cannot expect that $\boldsymbol{u} \times \boldsymbol{\omega}$ is necessarily large where $\boldsymbol{u} \cdot \boldsymbol{\omega}$ is small simply by considering the relation $|\boldsymbol{u} \cdot \boldsymbol{\omega}|^2 + |\boldsymbol{u} \times \boldsymbol{\omega}|^2 = u^2 \omega^2$. It is not applicable for a general unsteady flow in which $\boldsymbol{u}$ and $\boldsymbol{\omega}$ vary in magnitude as well as in their relative orientations. Second, it is not $\boldsymbol{u} \times \boldsymbol{\omega}$ but $\boldsymbol{\nabla} \times (\boldsymbol{u} \times \boldsymbol{\omega})$ that may deform the vorticity field as described by the vorticity equation

$$\frac{\partial \boldsymbol{\omega}}{\partial t} + \boldsymbol{\nabla} \times (\boldsymbol{\omega} \times \boldsymbol{u}) = \nu \nabla^2 \boldsymbol{\omega}. \tag{7.16}$$

In fact, the vorticity and velocity are almost orthogonal inside the main vortex tube. While helicity density is small in the main tube, it is large in the interaction zone. Contrary to the above argument, the deformation of the structure is rapid in the interaction zone and the structure of the vortex tube is preserved for a long time. Third, the nonlinear term on the right-hand side of (2.1), which describes the interaction between neighbouring positions, is generally of the same order of magnitude as $\boldsymbol{u} \times \boldsymbol{\omega}$. It certainly contribute to the local change of the velocity field though it disappears after integration with respect to space.

The exclusiveness of domains of high helicity density and high energy dissipation

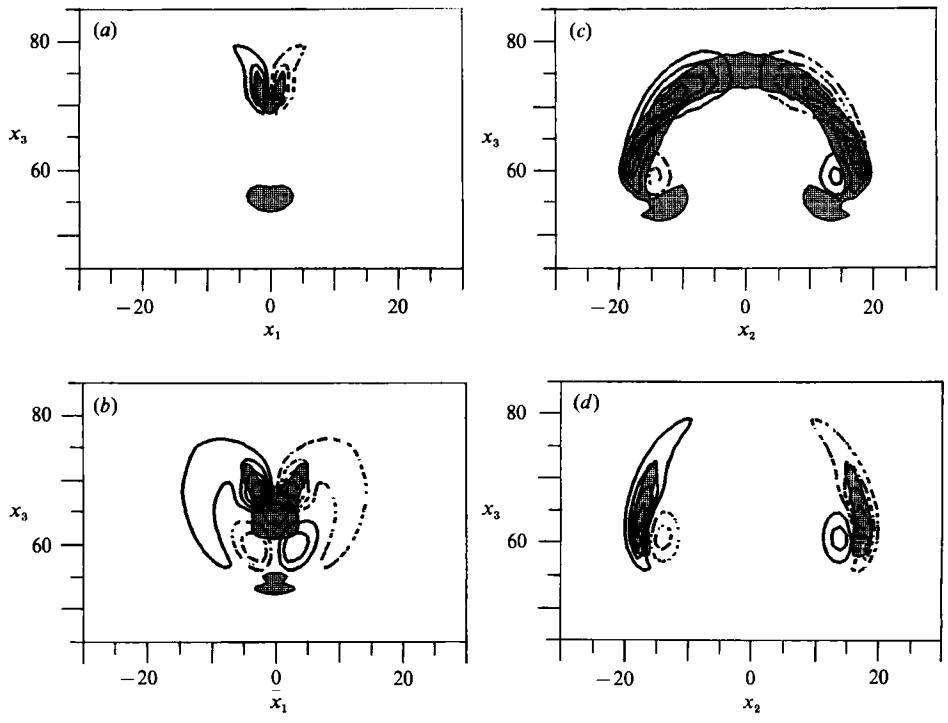

FIGURE 31. Cross-sections of helicity density (in a moving frame of minimum I) and energy dissipation rate at $t = 5$ for Case I. The positive and negative parts of the helicity density are drawn by solid and broken lines, respectively. The contour levels are 20, 40 and 60% of the maxima for both quantities. Shaded areas are high-dissipation regions in which the energy dissipation rate is larger than 20% of the maximum. The planes of the cross-sections are (*a*) $x_2 = 10\Delta x$, (*b*) $x_2 = 15\Delta x$, (*c*) $x_1 = 1.5\Delta x$ and (*d*) $x_1 = 5\Delta x$, the positions of which are shown in figure 32.

has been discussed by Moffatt (1985) under the assumption that a turbulent flow is dominated by steady solutions of the Euler equation bounded by sheets of high dissipation. It was conjectured that each steady solution might describe the long-lived structure of the coherent motion in turbulence. Several numerical simulations of turbulent shear layers (Hussain 1986) demonstrate that there is significant overlap of the two domains but their peaks are exclusive. Figure 31 shows four cross-sections of helicity density (in a moving frame of minimum I) and energy-dissipation rate at $t = 5$ for Case I. The positive and negative parts of the helicity density are drawn by solid and broken lines, respectively. The contour levels are 20, 40 and 60% of the maximum of helicity magnitude. Shaded areas denote high-dissipation regions, in which the dissipation rate is larger than 20% of the maximum. The positions of these four planes are shown in figure 32. These planes are chosen so that they go through regions of high vorticity and high helicity, namely, bridges or threads.

Figures 31 (*a*) ($x_2 = 10\Delta x$) and 31 (*b*) ($x_2 = 15\Delta x$) show that both the dissipation and the helicity are large in bridges, while figures 31 (*c*) ($x_1 = 1.5\Delta x$) and 31 (*d*) ($x_1 = 5\Delta x$) show that they are high in a thread. Therefore, these two fields are not exclusive in the present flow field, but, on the contrary, they overlap substantially in bridges and threads. We have confirmed this overlap in other planes also (figures are not reproduced here).

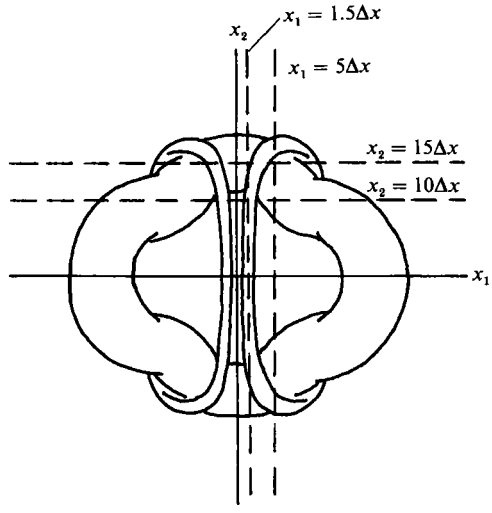

FIGURE 32. Planes chosen for figure 31. Outlines of the vortex ring (25% of $|\omega|_{max}$) are drawn for reference.

8. Concluding remarks

The vortex interaction in a collision of two vortex rings has been investigated by solving the Navier–Stokes equation numerically. Two identical circular vortex rings were set side by side at the initial time. It was observed that they undergo two reconnections successively as had been visualized experimentally with dye or smoke. The overall shapes of the vortex rings are different for different initial conditions, but the mechanism of the reconnection is explained by bridging.

Because of the symmetric configuration for the initial condition, the two vortex rings approach in an exactly anti-parallel fashion. The mechanism of the reconnection is not a simple cancellation of opposite-signed vorticity but a more complex three-dimensional phenomenon, bridging, which is composed of three fundamental processes: cancellation of opposite-signed vorticity, transfer of vorticity to orthogonal directions and vortex stretching. This mechanism was discovered and explained by MH in a simulation of a pair of anti-parallel sinusoidal vortex tubes with opposite circulation, except for the prediction of the position of bridges. They relate the position of bridges to stagnation points in a frame moving with the interacting dipole, but actually bridges are created at the point of maximum vortex stretching rate.

There are several characteristic features of bridging. It occurs when two anti-parallel vortex tubes touch each other. Most of the original vorticity is cancelled out, and the same amount of circulation appears perpendicularly to the original anti-parallel vortex tubes, as bridges. They are created in the front of the interacting vortex tubes, or ahead of the direction of the self-advection of the interacting vortex tubes near the point of maximum stretching rate. The cancellation of the original anti-parallel vortex tubes is not complete, for neighbouring portions of the vortex tubes, which are directed perpendicularly to the interacting vortex tubes, together with newly created bridges, bend the original tubes in such a way that they move away from each other by their self-induction.

The bridging mechanism manifests itself very clearly in the present simple geometry of an interacting vortex pair which are anti-parallel, of equal strength and

in a symmetric configuration. It is expected that the vortex reconnection in asymmetric configurations, such as a trefoiled vortex ring (Kida & Takaoka 1987) and two orthogonal straight vortex tubes (Melander & Zabusky 1988), may have the same characteristic feature as that of bridging mentioned above and that the bridging may be a main mechanism in the vortex reconnection process for a general configuration of the vortex field. In general cases of asymmetric configurations, however, much more complicated interactions are expected. For example, if two interacting vortices have different circulation, the weaker vortex would wind around the stronger one. Viscosity plays an essential role in bridging. It is therefore anticipated that the bridging may not occur in the inviscid limit and helicity may be invariant in this limit.

We studied various field quantities. The regions in which energy dissipation is large is highly localized in space compared with enstrophy (or vorticity) concentrated regions. The kinetic energy of fluid decays according to the same power law as that in a fully developed turbulence. This can be understood by noting that energy dissipation is dominant in the interaction zone, bridges and threads. It was also observed that the enstrophy-production rate takes high values in these regions. This is reasonable because both the energy dissipation and the enstrophy production rates are determined by the strain rate.

The helicity and super-helicity densities represent the skewed structure of the velocity and vorticity fields, respectively. We note that vorticity is large in the main vortex tubes, the form of which is preserved for a relatively long time. On the other hand, it is the helicity density that is large in bridges and threads. These shapes change rapidly in time. The high-helicity-density and high-energy-dissipation regions overlap significantly though their peaks may be different. We therefore conclude that a long-lived structure may carry strong vorticity rather than high helicity density.

The motion of a passive scalar advected by interacting vortex tubes was also examined. Stretching of a fluid element dilutes the density of a passive scalar, whereas it intensifies the magnitude of vorticity. The concentration of a passive scalar does not always mark the magnitude of vorticity even if they sometimes have a similar appearance.

With the resolution (64^3) of the present numerical simulation the initial Reynolds number Γ/ν cannot be higher than about a thousand. We have seen that viscosity tends to reduce the curvature of vortex tubes and prolong the reconnection time, especially of the second reconnection. We also observed that the amount of remnant circulation after the first reconnection increases with the Reynolds number, suggesting that the reconnection may not occur in the inviscid limit. Numerical simulations with higher resolution are necessary to resolve the Reynolds-number dependence of reconnections.

We studied in this paper the vortex interaction of two identical vortex rings in a symmetric configuration. In general, we expect that asymmetric configurations with different circulations and different orientations would occur more often. Then we expect many interesting phenomena, such as the wrapping of a weaker vortex tube around a stronger one and vortex breaking due to the occurrence of three-dimensional instabilities. These subjects are left for future studies with simulations of higher resolution.

The calculation was done on the FACOM M780/30-VP400E system in the data processing centre of Kyoto University. This work was supported by the US

Department of Energy Grant DE-FG05-88ER-13839, Office of Naval Research Grant N00014-89-J-1361 and a Grant-in-Aid for Scientific Research from the Ministry of Education, Science and Culture of Japan.

REFERENCES

ANDERSON, C. & GREENGARD, C 1988 The vortex ring merger problem at infinite Reynolds number (Preprint).

ASHURST, W. T. & MEIRON, D. 1987 Numerical study of vortex reconnection. *Phys. Rev. Lett.* **58**, 1632–1635.

BEALE, J. T., KATO, T. & MAJDA, A. 1984 Remarks on the breakdown of smooth solutions for the 3-D Euler equations. *Commun. Math. Phys.* **94**, 61–66.

BRISSAUD, A., FRISH, U., LEORAT, J., LESIEUR, M. & MAZURE, A. 1973 Helicity cascades in fully developed isotropic turbulence. *Phys. Fluids* **16**, 1366–1367.

CHAMBERLAIN, J. P. & LIU, C. H. 1985 Navier–Stokes calculation for unsteady three-dimensional vortical flows in unbounded domains,. *AIAA J.* **23**, 868–874.

CHORIN, A. J. 1982 The evolution of a turbulent vortex. *Commun. Math. Phys.* **83**, 517–535.

COMTE-BELLOT, G. & CORRSIN, S. 1966 The use of a contraction to improve the isotropy of grid-generated turbulence. *J. Fluid Mech.* **25**, 657–682.

DRAZIN, P. G. & REID, W. H. 1981 *Hydrodynamic Stability*. Cambridge University Press.

FOHL, F. & TURNER, J. S. 1975 Colliding vortex rings. *Phys. Fluids* **18**, 433–436.

GINEVSKII, A. S., KOLESNIKOV, A. V. & UKHANOVA, L. N. 1979 Decay of turbulence behind a double grid of cylinders with opposite motion of grids. *Isv. Acad. Nauk. SSSR, Mekh. Zhidk. Gaza* **14**, 17–25.

HUSSAIN, F. 1983 Coherent structure – reality and myth. *Phys. Fluids* **26**, 2816–2850.

HUSSAIN, F. 1986 Coherent structures and turbulence. *J. Fluid Mech.* **173**, 303–356.

KERR, R. M. & HUSSAIN, F. 1989 Simulation of vortex reconnection. *Physica D* **37**, 474–484.

KIDA, S. 1981 Similar solutions in modified cumulant expansion. *Phys. Fluids* **24**, 604–614.

KIDA, S. 1983 Turbulence and singularity of the velocity field. *Publ. RIMS, Kyoto University* **19**, 1033–1048.

KIDA, S. 1985 Numerical simulation of two-dimensional turbulence with high-symmetry. *J. Phys. Soc. Japan* **54**, 2840–2854.

KIDA, S. & MURAKAMI, Y. 1988 Numerical study of energy decay of turbulence. *J. Phys. Soc. Japan* **57**, 3657–3660.

KIDA, S. & MURAKAMI, Y. 1989 Statistics of velocity gradients in turbulence at moderate Reynolds numbers. *Fluid Dyn. Res.* **4**, 347–370.

KIDA, S. & TAKAOKA, M. 1987 Bridging in vortex reconnection. *Phys. Fluids* **30**, 2911–1924.

KIDA, S. & TAKAOKA, M. 1988 Reconnection of vortex tubes. *Fluid Dyn. Res.* **3**, 257–261.

KIDA, S. & TAKAOKA, M. 1991 Breakdown of frozen motion of vorticity field and vorticity reconnection. *J. Phys. Soc. Japan* **60** (in press).

KIDA, S., TAKAOKA, M. & HUSSAIN, F. 1989 Reconnection of two vortex rings. *Phys. Fluids* A **1**, 630–632.

KIDA, S., TAKAOKA, M. & HUSSAIN, F. 1991 Formation of head–tail structure in a two-dimensional uniform straining flow. *Phys. Fluids* (submitted).

KOLMOGOROV, A. N. 1941 On degeneration of isotropic turbulence in incompressible viscous liquid. *Dokl. Akad. Nauk. URSS* **31**, 538–540.

LEONARD, A. 1974 Numerical simulation of interacting three-dimensional vortex filaments. In *Proc. 4th Intl Conf. Numerical Method in Fluid Dynamics*, pp. 245–250. Springer.

LEONARD, A. 1980 Vortex methods for flow simulation. *J. Comput. Phys.* **37**, 289–335.

LESIEUR, M. & SCHERTZER, D. 1978 Autosimilar extinction of turbulence with large Reynolds number. *J. Méc.* **17**, 609–646.

LEVICH, E. 1987 Certain problems in the theory of developed hydrodynamical turbulence. *Phys. Rep.* **151**, 129–238.

LING, S. C. & WAN, C. A. 1972 Decay of isotropic turbulence generated by a mechanically agitated grid. *Phys. Fluids* **15**, 1363–1369.

MELANDER, M. V. & HUSSAIN, F. 1988 Cut-and-connect of two antiparallel vortex tubes. *Center for Turbulence Research Proc. Summer Program 1988* (referred to herein as MH).

MELANDER, M. V. & HUSSAIN, F. 1990 Topological aspects of vortex reconnection. In *Topological Fluid Mechanics* (ed. H. K. Moffatt & A. Tsinober), pp. 485–499. Cambridge University Press.

MELANDER, M. V. & ZABUSKY, N. J. 1988 Interaction and 'apparent' reconnection of 3D vortex tubes via direct numerical simulations. *Fluid Dyn. Res.* **3**, 247–250.

MOFFATT, K. 1969 The degree of knottedness of tangled vortex lines. *J. Fluid Mech.* **159**, 117–129.

MOFFATT, K. 1985 Magnetostatic equilibria and analogous Euler flows of arbitrary complex topology. Part 1. Fundamentals. *J. Fluid Mech.* **159**, 359–378.

ORSZAG, S. A. 1971 Numerical simulation of incompressible flows within simple boundaries. I. Galerkin (spectral) representations. *Stud. Appl. Maths* **50**, 293–327.

OSHIMA, Y. & ASAKA, S. 1977 Interaction of two vortex rings along parallel axes in air. *J. Phys. Soc. Japan* **42**, 708–713.

OSHIMA, Y. & IZUTSU, N. 1988 Cross-linking of two vortex rings. *Phys. Fluids* **31**, 2401–2403.

PUMIR, A. & KERR, R. M. 1987 Numerical simulation of interacting vortex tubes. *Phys. Rev. Lett.* **58**, 1636–1639.

PUMIR, A. & SIGGIA, E. D. 1987 Vortex dynamics and the existence of solutions to the Navier–Stokes equations. *Phys. Fluids* **30**, 1606–1626.

SAFFMAN, P. G. 1967 The large-scale structure of homogeneous turbulence. *J. Fluid Mech.* **27**, 581–593.

SCHATZLE, P. 1987 An experimental study of fusion of vortex rings. Ph.D. thesis, California Institute of Technology.

SCHWARZ, K. W. 1985 Three-dimensional vortex dynamics in superfluid ^{4}He: line–line and line–boundary interactions. *Phys. Rev.* B **31**, 5782–5804.

SHARIFF, K., LEONARD, A., ZABUSKY, N. J. & FERZIGER, J. H. 1988 Acoustics and dynamics of coaxial interacting vortex rings. *Fluid Dyn. Res.* **3**, 337–343.

SHIRAYAMA, S. & KUWAHARA, H. 1984 Vortex method in three-dimensional flow. In *Proc. 9th Intl. Conf. Numerical Methods in Fluid Dynamics*, (ed. Soubbaramayer and J. P. Boujot), pp. 503–507. Springer.

SIGGIA, E. D. 1985 Collapse and amplification of a vortex filament. *Phys. Fluids* **28**, 794–805.

SIGGIA, E. D. & PUMIR, A. 1985 Incipient singularities in the Navier–Stokes equation. *Phys. Rev. Lett.* **55**, 1749–1752.

STANAWAY, S., SHARIFF, K. & HUSSAIN, F. 1988 Head-on collision of viscous vortex rings. *Center for Turbulence Research: Proc. Summer Program 1988.*

TAKAKI, R. & HUSSAIN, F. 1985 Recombination of vortex filaments and its role in aerodynamic noise. In. *Proc. 5th Symp. on Turbulent Shear Flows, Cornell University*, pp. 3.19–3.25.

TATSUMI, T., KIDA, S. & MIZUSHIMA, J. 1978 The multiple-scale cumulant expansion for isotropic turbulence. *J. Fluid Mech.* **85**, 97–142.

UBEROI, M. S. 1963 Energy transfer in isotropic turbulence. *Phys. Fluids* **6**, 1048–1056.